

Doctoral Dissertation

Investigating QCD phase transitions with effective theory approach

Author:
Michał Szymański

Supervisors:
Dr hab. Chihiro Sasaki
Dr Pok Man Lo



Uniwersytet
Wrocławski

Wrocław, 2022

Abstract

Understanding the phase diagram of quantum chromodynamics (QCD) is one of the key objectives of high-energy physics. A lot of effort, on both theoretical and experimental sides, have been put to achieve this goal, but the task is far from being complete. The phase structure of QCD is expected to be very rich. Phase transitions which are particularly interesting from the perspective of phenomenology of heavy-ion collisions are deconfinement and chiral phase transition.

Theoretical investigation of QCD phase transitions is very difficult as it requires non-perturbative methods. The most accurate predictions are obtained from numerical lattice simulations (LQCD). In particular, it was found that chiral transition and deconfinement are smooth crossovers. These methods, however, are currently not capable of describing QCD thermodynamics at large chemical potential because of the numerical sign problem and thus other approaches are necessary. Very useful for this purpose are effective theories of QCD.

In the effective approach, one considers simplified models of QCD which share its particular features, for example symmetries, while having considerably simpler structure. Effective models are useful for several reasons. First, they may be used to explore the QCD phase diagram in the range of parameters for which LQCD methods are not applicable, and thus serve as the extrapolation tool. Particularly, many models predict the existence of the critical point (CP) in the QCD phase diagram. Moreover, with effective models one can investigate the role of different parameters or interactions and, thus, they may serve as explanatory tools, complementary to more advanced methods.

The goal of this thesis is to extend our knowledge on deconfinement and chiral phase transition. To this end, we use the effective approach. In particular, we investigate the effects of magnetic field and baryon chemical potential on these phenomena. To study deconfinement, we use an effective Polyakov loop model. We explore the consequences of both spontaneous and explicit $Z(3)$ symmetry breaking on Polyakov loop and its fluctuations. We compute ratios of Polyakov loop susceptibilities and show that the essential features of these observables, seen in LQCD, can be successfully captured by the effective approach. We also argue that ratio observables are sensitive to the strength of explicit center symmetry breaking.

Next, we generalize the model to finite magnetic field and study the impact of this parameter on deconfinement of heavy quarks by calculating Polyakov loop and its fluctuations. We demonstrate that the strength of the explicit center symmetry breaking increases with the magnetic field. In consequence, increasing magnetic field tends to decrease the (pseudo) critical temperature and leads to shrinking of the first-order region in the phase diagram. We also study how Polyakov loop and its susceptibilities are affected when the magnetic field and quark chemical potential are considered simultaneously.

When light quarks are considered, chiral physics cannot be neglected. It is known that many chiral models tend to predict the opposite trend on the magnetic field dependence on the deconfinement and chiral transition temperatures, than observed in lattice QCD. We demonstrate how the correct trend on the former can be achieved in our model by considering an improved constituent quark mass function. To show the importance of in-medium effects, we study the screening of four-quark interaction by the ring diagram in an effective chiral quark model, inspired by Coulomb gauge QCD. In consequence, the medium-dependent coupling is obtained, which naturally reduces the chiral transition temperature in a class of models and generates an inverse magnetic catalysis.

The QCD phase diagram can also be explored experimentally with the means of relativistic heavy-ion collisions. One of the goals of these experiments is to search for the conjectured QCD critical point. Large fluctuations associated with the critical point are expected to affect various experimentally measurable quantities. An important class of observables sensitive to the critical point are fluctuations of conserved charges. We study the effect of the critical point on net-proton number fluctuations using the phenomenological model in which fluctuations of the critical mode are coupled to protons and anti-protons. We calculate net proton-number cumulants along the phenomenological freeze-out line and discuss how our results depend on the model parameters and the proximity of the chemical freeze-out line to the CP.

Streszczenie

Zrozumienie diagramu fazowego chromodynamiki kwantowej (QCD) to jedno z kluczowych zadań fizyki wysokich energii. Włożono w nie bardzo dużo wysiłku, zarówno ze strony teoretycznej jak i eksperymentalnej, ale cel ten nie został jeszcze w pełni osiągnięty. Spodziewamy się, że struktura fazowa QCD jest bardzo złożona. Z punktu widzenia fenomenologii zderzeń ciężkich jonów szczególnie istotne są uwolnienie kwarków i chiralne przejście fazowe.

Pod względem teoretycznym badanie przejść fazowych w QCD jest niezwykle trudne, ponieważ wymaga metod nieperturbacyjnych. Najdokładniejszych przewidywań dostarczają numeryczne metody QCD na sieci (LQCD). W szczególności odkryto, że dla fizycznych mas kwarków zarówno przejście chiralne jak i uwolnienie kwarków są gładkimi przejściami typu crossover. Jednak metody sieciowe obecnie nie są w stanie opisać termodynamiki QCD dla dużych potencjałów chemicznych z powodu numerycznego problemu znaku, dlatego też potrzebne są inne metody. Szczególnie użyteczne w tym kontekście są teorie efektywne QCD.

W podejściu rozważa się uproszczone modele QCD, które dzielą z nią pewne własności, na przykład symetrie, mając jednocześnie znacznie prostszą strukturę. Modele efektywne są użyteczne z kilku różnych powodów. Po pierwsze, mogą być one użyte, żeby badać diagram fazowy QCD dla paramentów, gdzie metody LQCD nie dają się zastosować, a przez to stanowią narzędzie ekstrapolacji. W szczególności wiele modeli przewiduje istnienie punktu krytycznego (CP) na diagramie fazowym QCD. Ponadto przy pomocy modeli efektywnych można badać rolę różnych parametrów a także oddziaływań, przez co stanowią one użyteczne narzędzia objaśniające, będące uzupełnieniem dla bardziej skomplikowanych metod.

Celem niniejszej rozprawy jest poszerzenie naszej wiedzy na temat uwolnienia kwarków i chiralnego przejścia fazowego. Naszym podstawowym narzędziem badawczym są teorie efektywne. W szczególności zbadaliśmy wpływ pola magnetycznego i barionowego potencjału chemicznego na te zjawiska. Do badania uwolnienia kwarków, użyty został model efektywny oparty na pętli Polyakova. Zbadaliśmy konsekwencje spontanicznego i jawnego łamania symetrii $Z(3)$ na pętli Polyakova i jej fluktuacje. Obliczyliśmy stosunki podatności pętli Polyakova i pokazaliśmy, że kluczowe własności tych wielkości, zaobserwowane przez LQCD, mogą być z sukcesem uchwycone przy użyciu podejścia efektywnego. Uzasadniamy też, że stosunki podatności są wrażliwe na siłę jawnego łamania symetrii centralnej.

Następnie model ten został uogólniony do niezerowego pola magnetycznego. Zbadaliśmy wpływ tego parametru na uwolnienie ciężkich kwarków, obliczając pętli Polyakova i jej fluktuacje. Pokazaliśmy, że pole magnetyczne zwiększa siłę jawnego łamania symetrii. Na skutek tego wraz ze wzrostem pola magnetycznego temperatura (pseudo) krytyczna maleje, a obszar przejścia pierwszego rzędu zmniejsza się. Zbadaliśmy również jak pętla Polyakova i jej podatności reagują kiedy pole magnetyczne i kwarkowy potencjał

chemiczny oddziałują na system jednocześnie.

Kiedy rozważa się lekkie kwarki, należy uwzględnić rolę fizyki chiralnej. Wiadomo, że wiele modeli chiralnych przewiduje odwrotny niż zaobserwowany na sieci trend w zależności temperatur pseudokrytycznych uwolnienia kwarków i przejścia chiralnego od pola magnetycznego. Pokazaliśmy, jak używając ulepszonej funkcji masowej dla ubranych kwarków można w naszym modelu uzyskać poprawny trend dla temperatury uwolnienia kwarków. Żeby pokazać rolę efektów pochodzących od ośrodka, zbadaliśmy wpływ ekranowania oddziaływania czterokwarkowego przez diagram pierścieniowy w efektywnym modelu chiralnym, inspirowanym QCD w cechowaniu Coulomba. Na skutek ekranowania stała sprzężenia staje się zależna od ośrodka, co w naturalny sposób redukuje temperaturę przejścia chiralnego w tej klasie modeli i generuje odwrotną katalizę magnetyczną.

Diagram fazowy QCD może też być badany eksperymentalnie przy pomocy zderzeń ciężkich jonów. Jednym z celów tych eksperymentów jest poszukiwanie hipotetycznego punktu krytycznego na diagramie fazowym QCD. Silne fluktuacje związane z punktem krytycznym powinny wpływać na różne wielkości obserwowane eksperymentalnie. Ważną klasą obserwabli wrażliwych na punkt krytyczny są fluktuacje ładunków zachowanych. Zbadaliśmy wpływ punktu krytycznego na fluktuacje wypadkowej liczby protonów korzystając z fenomenologicznego modelu, w którym fluktuacje modu krytycznego sprzężone są z protonami i anty-protonami. Obliczyliśmy kumulanty wypadkowej liczby protonów wzdłuż fenomenologicznej linii wymrożenia i przedyskutowaliśmy, jak nasze wyniki zależą od parametrów modelu i odległości od punktu krytycznego.

Acknowledgments

I would like to express my gratitude towards Chihiro Sasaki and Pok Man Lo for their supervision, guidance and all the support I received from them during my PhD studies. Furthermore, I also thank Krzysztof Redlich for his support and valuable comments, as well as to Marcus Bluhm for many friendly and insightful conversations. I learned a lot from all of you during these years.

I thank my friends from room 434: Mateusz Cierniak, Michał Marczenko, and Valeriya Mykhaylova for all the great time I spent with them. In particular, I thank Michał Marczenko for many friendly and often intriguing discussions, and for a constant help in dealing with bureaucracy. I would also like to thank all the members of Institute of Theoretical Physics who at some point helped me during my scientific adventure. I also thank Michał and Valeriya for suggestions on improving my thesis.

Furthermore, I am grateful to my family and friends for their support. In particular, I owe a debt of gratitude to my wonderful wife Justyna for her support and for believing in me when I did not believe in myself. And, of course, for preparing me countless cups of tea.

Finally, I would like to thank Mr Krzysztof Łapczyński for showing me in high-school that physics can be fascinating and fun.

I acknowledge the support from the Polish National Science Centre (NCN) under the Polonez grant no. 2016/21/P/ST2/04035, Opus grant no. 2018/31/B/ST2/01663 and Preludium grant no. 2020/37/N/ST2/00367.

Contents

1	Introduction and structure of the thesis	1
2	Quantum Chromodynamics	5
2.1	QCD Lagrangian	5
2.2	Symmetries of quantum chromodynamics	8
2.2.1	General overview of symmetries	8
2.2.2	Exact and approximate symmetries of the QCD Lagrangian	11
2.3	Spontaneous chiral symmetry breaking	16
2.4	Confinement	17
2.4.1	Overview	17
2.4.2	Lattice results on confinement	20
3	Aspects of QCD thermodynamics	23
3.1	Phase transitions and critical phenomena	23
3.1.1	General overview of phase transitions	23
3.1.2	Statistical mechanics	24
3.1.3	Continuous phase transitions and critical phenomena	26
3.1.4	First-order phase transitions	30
3.2	QCD phase transitions	31
3.2.1	Deconfinement	31
3.2.2	Chiral symmetry restoration	35
3.3	QCD phase diagram	36
4	Polyakov loop fluctuations in the presence of the external fields	39
4.1	Polyakov loop susceptibilities and ratio observables	39
4.1.1	Polyakov loop and its fluctuations	39
4.1.2	Properties of ratio observables	41
4.2	Modeling Polyakov loop fluctuations	45
4.2.1	Color group integration	45
4.2.2	Gaussian model with an explicit symmetry breaking field	47
4.2.3	Polyakov loop potential	48
4.2.4	Scaling of the R_A ratio	52

4.2.5	Comparison with LQCD and PNJL model results	53
5	Polyakov loop fluctuations in a strong magnetic field and finite chemical potential	59
5.1	LQCD results on magnetized QCD	59
5.2	Polyakov loop potential at finite magnetic field	62
5.2.1	Explicit breaking strength in the external magnetic field	62
5.2.2	Robustness of the linear approximation	66
5.3	Numerical results for heavy quarks at finite magnetic field	67
5.3.1	Polyakov loop and its fluctuations	67
5.3.2	Deconfinement phase diagram	71
5.4	Studying the interplay between deconfinement and chiral dynamics	74
5.5	Driving the inverse magnetic catalysis with the ring diagram	78
5.5.1	Chiral quark model with dressed interaction	78
5.5.2	Gap equations	82
5.5.3	Numerical results	85
5.6	Simultaneous effect of finite chemical potential and magnetic field on deconfinement	87
5.6.1	Sign problem and the Polyakov loop	87
5.6.2	Modeling Polyakov loop fluctuations at finite chemical potential	89
6	Net-proton number fluctuations in the presence of the QCD critical point	95
6.1	Fluctuations of conserved charges	95
6.2	Modeling critical fluctuations in heavy-ion collisions	99
6.2.1	Baseline model	99
6.2.2	Coupling to critical mode fluctuations	100
6.2.3	Magnetic equation of state	103
6.2.4	Mapping between spin model and QCD	103
6.3	Numerical results on the net-proton number fluctuations	105
6.3.1	Kinematic cuts	106
6.3.2	Net-proton number cumulant ratios	106
7	Conclusions and outlook	113
	Appendices	117
A	Effective gluon potential	119

Chapter 1

Introduction and structure of the thesis

The medium created during ultra-relativistic heavy-ion collisions, the quark-gluon plasma (QGP), is the hottest and most dense substance created in the laboratory. Moreover, if the collision is non-central, the extremely strong magnetic fields are generated. To fully understand processes occurring during heavy-ion collisions, as well as what happened shortly after the Big Bang, it is important to understand how matter behaves under such extreme conditions.

What holds together quarks and gluons inside nucleons and nucleons inside atomic nuclei are strong interactions. They are theoretically described by quantum chromodynamics (QCD) [1–4]. One of its remarkable properties is the asymptotic freedom [5–7] – the interaction strength decreases with the energy scale. This means that at high energies the dynamics of strong interactions can be well described with the perturbative approach [3, 8, 9] which is the basic tool to handle interacting quantum field theories. On the other hand, at low energies the QCD coupling is not small and the perturbation theory is no longer suitable for describing the corresponding processes reliably. The low-energy dynamics of QCD is, in fact, very complicated. The asymptotic states of QCD are not quarks and gluons, the fundamental degrees of freedom present in the QCD Lagrangian, but their, colorless, bound states – hadrons. This property is called confinement. Another peculiar feature of QCD is the spontaneous breaking of chiral symmetry which governs the low-energy dynamics of hadrons [10].

The possibility of transition from hadrons to quark-gluon plasma was anticipated shortly after discovery of QCD [11–14]. Later, QGP was observed experimentally [15]. Despite extensive theoretical and experimental work, there are still many open questions regarding properties of such medium. Although QGP created during heavy-ion collisions is a dynamical system, there is evidence that it is almost in equilibrium [16, 17]. Therefore, to fully understand its properties, it is important to investigate thermodynamics of the strongly interacting matter. This includes investigation of the QCD phase diagram.

The phase structure of QCD is expected to be very rich [16, 18, 19], and can be explored in a wide range of parameters. From the phenomenological perspective, the most interesting ones are temperature and baryon chemical potential. The latter is related to baryon number density of a system and hence is relevant for the proper description of relativistic heavy-ion collisions [16, 19–21]. Another parameter relevant for phenomenology of QCD is magnetic field [20, 22–26]. Although gluons have no electric charge, they may be affected by magnetic fields as well, due to their coupling to quarks. There are several areas where intensities of the magnetic field can be large enough to affect strong interactions in an observable manner. In non-central heavy-ion collisions the remnants of colliding nuclei generate extremely strong, although short-lived, magnetic fields of the order of $10^4 - 10^5 \text{ MeV}^2$ (where $1 \text{ MeV}^2 \approx 1.44 \times 10^9 \text{ T}$) [27–32]. Strong magnetic fields ($\sim 10^{10} - 10^{12} \text{ T}$) are also expected to be present at surfaces of the specific types of neutron stars, the magnetars [33, 34], with possibly higher field intensities in the core [34]. There is also a possibility that strong fields existed in the Early Universe [35].

From the theoretical standpoint, the task of exploring QCD phase diagram is extremely difficult because QCD for the energies relevant for phase transitions is strongly coupled and thus requires non-perturbative description [16]. The main source of knowledge about QCD thermodynamics are first-principle numerical simulations in which QCD is put onto a discretized space-time grid, the approach known as lattice QCD (LQCD) [36–39]. They give a strong evidence that the transition from the hadronic matter to QGP at vanishing and small baryon chemical potentials, $\mu_B/T \ll 1$, is a smooth crossover [40–46]. These methods, unfortunately, fail for larger chemical potentials due to the so-called sign problem [39, 47]. On the other hand, lattice simulations at finite magnetic field are possible [48, 49], and it was found that this quantity affects chiral dynamics and deconfinement in a non-trivial way.

Since lattice methods are currently not capable of describing QCD thermodynamics at large baryon chemical potential, different approaches have to be considered to investigate this part of the QCD phase diagram. Exceptionally useful for that purpose are effective theories, or models. In this approach, one does not attempt to solve QCD directly but considers theories which exhibit some particular features of QCD, for example symmetries or confinement, while having considerably simpler structure which makes them more tractable mathematically [50]. Effective modeling gives an opportunity to obtain qualitative insights into a possible phase structure of QCD in parameter range currently inaccessible to LQCD methods. Especially, many models predict the existence of the critical point (CP) in the phase diagram [20, 21, 51–53]. However, since models are only approximations of QCD, it is important to confront their results with the existing LQCD and experimental data to obtain more accurate predictions.

An important feature of the effective approach is that one can temporarily include, or suppress, certain class of interactions (or diagrams) as well as explore the role of different parameters, which makes this approach a powerful explanatory tool, complementary to more advanced techniques. For understanding the dynamics of QCD, two particular

limits are useful: the chiral limit and the pure gauge limit. In the chiral limit, quarks are assumed to be massless and thus the chiral symmetry of the QCD Lagrangian becomes exact. This limit is particularly useful for gaining insights into physics of light quarks (up, down and strange) and investigation of the chiral phase transition [54, 55]. In the pure gauge limit, quarks are assumed to be infinitely heavy, and thus decouple from the gluon dynamics. In this limit deconfinement becomes a true phase transition which can be related to the spontaneous breaking of the so-called $Z(3)$ center symmetry with the corresponding order parameter being the Polyakov loop [56–59].

The QCD phase diagram can also be explored experimentally with the aid of relativistic heavy-ion collisions [16, 17, 60]. The density and temperature of a system created during a collision depends on the beam energy. Hence, systems with different temperatures and baryon number densities can be created by varying the beam energies, which allows to explore different regions of the QCD phase diagram in μ_B and T plane [61]. One of the important goals of such experiments is to search for the signatures of the conjectured critical point in the QCD phase diagram. In general, a system near a critical point exhibits large fluctuations [62, 63]. Thus, the QCD critical point may affect observable quantities [64, 65]. In particular, a non-monotonic beam-energy dependence of the fluctuations of conserved charges is considered as a conceivable experimental signature of the chiral critical behavior and of the CP in heavy-ion collisions [66–70]. Such a behavior is typically associated with the divergence of the correlation length and the fluctuations of the critical mode at the CP [49, 51, 64, 65, 71–73]. Another, indirect way of verifying the existence of the CP is given by searching for non-uniform structures in multiplicity distributions due to domain formations in the region of the first-order phase transition adjacent to the critical point [74–76].

The goal of this thesis is to investigate various aspects of two characteristic phase transitions of QCD – deconfinement and chiral symmetry restoration. Thorough understanding of these phenomena and their consequences is important for a proper description of strongly interacting matter and interpretation of experimental data. Our main theoretical tool is the effective approach. We focus mainly on the finite temperature and magnetic field and show how the existing LQCD data can be used to constraint effective models. We also emphasize the importance of fluctuations in studying the QCD phase diagram. The structure of the thesis is the following:

- In Chapter 2 we provide a general overview of QCD. We discuss the mathematical form of the Lagrangian, its symmetries and their realization in nature. We also discuss some aspects of confinement.
- Since our main goal is to study phase transitions of QCD, in Chapter 3 we review particular features of physics of phase transitions which are relevant for this purpose. Then, we proceed with the discussion of deconfinement and chiral symmetry restoration. Finally, discuss the conjectured QCD phase diagram.
- In Chapter 4 we present results of our effective model study of deconfinement [77].

To investigate features of deconfinement, we use an effective Polyakov loop model. We investigate the order parameter, its susceptibilities as well as their ratios. We show that properties of ratio observables observed in LQCD can be successfully captured in our model. Furthermore, we find that in our approach these observables are sensitive to the strength of explicit center symmetry breaking due to dynamical quarks. We also make an attempt to estimate the breaking strength of LQCD from the existing data.

- In Chapter 5, we extend the model discussed previously to a finite magnetic field, following Ref. [78]. We argue that magnetic field enhances the strength of explicit center symmetry breaking and show how this affects deconfinement of heavy quarks. Next, we show how our model can be used to understand the increasing deconfinement temperature in the class of chiral models and how the correct trend, as seen in lattice simulations, can be enforced by an improved constituent quark mass function. Next, following Refs. [79, 80], we discuss how screening of four-quark interaction affects the chiral transition at the vanishing and finite magnetic fields. Finally, following Ref. [81], we examine simultaneous effect of chemical potential and external magnetic field on deconfinement of heavy quarks.
- In Chapter 6 we discuss net-proton number fluctuations (as a proxy for net-baryon number fluctuations) in the vicinity of CP with the phenomenological model in which the critical mode fluctuations are coupled to protons and anti-protons (the results were published in Ref. [82]). We calculate net proton-number cumulants along the phenomenological freeze-out line and discuss how our results depend on the model parameters and the proximity of the chemical freeze-out line to the CP. We show that the ratio of variance and mean, C_2/C_1 , as well as kurtosis, C_4/C_2 as a function of beam energy resemble qualitative properties observed in the heavy-ion collisions data obtained by the STAR Collaboration at RHIC. The skewness, however, exhibits properties that contrast with the criticality expected due to the CP.
- Finally, in Chapter 7 we summarize the thesis.

Chapter 2

Quantum Chromodynamics

In this chapter, we provide an overview of quantum chromodynamics, the theory of strong interactions. We review the mathematical formulation of QCD and its symmetries, exact as well as approximate. Then, two distinctive properties of QCD – spontaneous chiral symmetry breaking and confinement are discussed.

2.1 QCD Lagrangian

Quantum chromodynamics is a non-Abelian gauge theory [83] with the gauge group $SU(3)$. The interactions are carried by spin-1 gauge bosons named gluons, and matter particles are spin 1/2 fermions called quarks. Each quark has three color components,

$$q = \begin{pmatrix} q_r \\ q_g \\ q_b \end{pmatrix} \quad (2.1)$$

often referred to as red, green, and blue. There are six quark flavors, grouped in three generations in the Standard Model of particle physics. Table 2.1 contains selected physical properties of each quark flavor. Note that because of confinement, quarks do not exist as asymptotic states but are bound into hadrons. Thus, their masses are not observable, and their values depend on the renormalization prescription [4].

The QCD Lagrangian reads

$$\mathcal{L} = \sum_{f \in \text{flavors}} \bar{q}_f (i\not{D} - m_f) q_f - \frac{1}{4} F_{\mu\nu}^a F_a^{\mu\nu}, \quad (2.2)$$

where f runs over quark flavors and color indices of quarks (as seen in Eq. (2.1)) are suppressed. $F_{\mu\nu}^a$ is the field-strength tensor,

$$F_{\mu\nu}^a = \partial_\mu A_\nu^a - \partial_\nu A_\mu^a + gf^{abc} A_\mu^b A_\nu^c, \quad (2.3)$$

where A_μ^a are the gluon fields, f^{abc} the structure constants of the gauge group, g the coupling strength and $a, b, c = 1, \dots, N_c^2 - 1$ (8 for QCD). Similarly to quantum electrodynamics (QED), for which the gauge group is Abelian, the interaction between quarks and gluons is introduced via the covariant derivative acting in the color space of quarks (i.e. it acts on the color vector (2.1)),

$$D_\mu = \partial_\mu - igT^a A_\mu^a \quad (2.4)$$

where $T^a = \lambda^a/2$ are 8 generators of the gauge group, with λ_a the Gell-Mann matrices. They satisfy the following commutation relations:

$$[T^a, T^b] = if^{abc}T^c. \quad (2.5)$$

The non-Abelian structure of QCD introduces $O(g)$ three- and $O(g^2)$ four-gluon vertices. The fact that in QCD not only quarks but also gluons are color-charged makes its dynamics much more intricate than the dynamics of QED, in which photons have no electric charge. One of the most striking examples is the asymptotic freedom – the strong coupling decreases with the energy scale and hence for very high energies, quarks may be seen as free particles. The running of the QCD coupling is governed by renormalization group (RG) equation [3]

$$\beta = \frac{\partial}{\partial \ln \mu} g(\mu) \quad (2.6)$$

where μ is the energy scale at which the coupling is measured. The sign of β function determines whether the coupling strength decreases or increases with μ . For QCD, the β function up to the lowest order in g , and in the limit where quark masses are much smaller than considered energies (and thus can be neglected), reads [5–7]

$$\beta(g) = -\frac{1}{16\pi^2} \left(11 - \frac{2}{3}n_f \right) g^3 \quad (2.7)$$

Generation	Flavor	Symbol	Mass [MeV]	Charge [e]
1	Up	u	$2.16^{+0.49}_{-0.26}$	2/3
	Down	d	$4.67^{+0.48}_{-0.17}$	-1/3
2	Charm	c	$(1.2 \pm 0.02) \times 10^3$	2/3
	Strange	s	93^{+11}_{-5}	-1/3
3	Top	t	$1.62 \times 10^5 - 1.72 \times 10^5$	2/3
	Bottom	b	$4.18^{+0.03}_{-0.02} \times 10^3$	-1/3

Table 2.1: Selected physical properties of three generations of quarks. Masses have been obtained from the Review of Particle Physics (Ref. [4]).

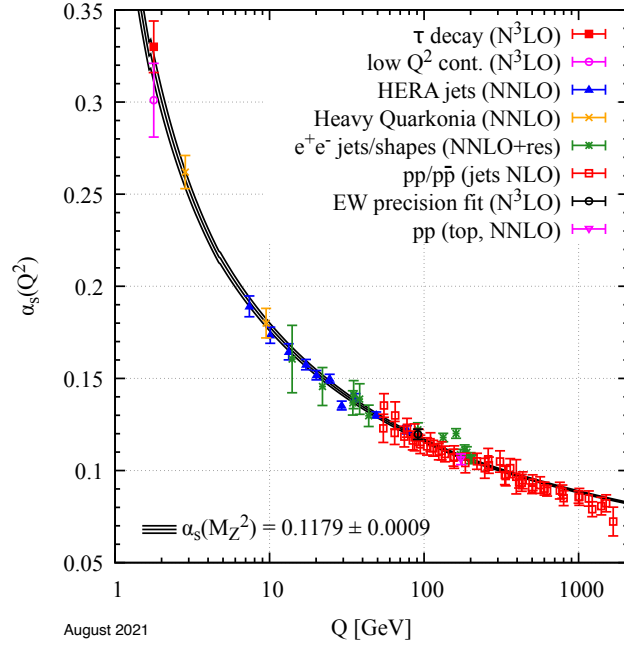


Figure 2.1: The QCD running coupling in function of the energy scale Q (the black line), together with experimental values determined in different experiments. Figure taken from the Review of Particle Physics (2021) [4].

and is negative for $n_f \leq 16$. Since there are only six quark flavors known, the β function of QCD is negative and its coupling strength decreases with the energy scale μ . This means that for large energies, the dynamics of QCD can be well described with the means of the perturbative expansion with respect to g . The running of the QCD coupling has been confirmed in numerous experiments (see Fig. 2.1 for the summary of various experimental results compared to the theoretical prediction, given by the black line [4]). When the RG equation is solved, the scale parameter Λ_{QCD} appears (its value depends on renormalization conditions, for example for the $\overline{\text{MS}}$ scheme and $N_f = 3$ $\Lambda_{QCD} \approx 300$ MeV [84]). Intuitively, for energies exceeding this parameter, the QCD dynamics has perturbative character, while for energies below the perturbative approach is no longer justified [84].

QCD, being a non-abelian gauge theory, is invariant under local $SU(3)$ transformations acting in the color space (i.e. on the color vector 2.1) which are defined as

$$\begin{aligned} A_\mu &\rightarrow A_\mu^U = U(x)A_\mu U^\dagger(x) + \frac{i}{g}U(x)\partial_\mu U^\dagger(x), \\ q_f &\rightarrow q_f^U = U(x)q_f \end{aligned} \quad (2.8)$$

where $A_\mu \equiv A_\mu^a T^a$ and $U(x)$ is the $SU(3)$ matrix which can be parametrized as

$$U(x) = \exp(ig\theta_a(x)T_a), \quad (2.9)$$

where $\theta_a(x)$ are real functions which depend on space-time coordinates x . Note that the field-strength tensor $F_{\mu\nu} \equiv F_{\mu\nu}^a T^a$ transforms as

$$F_{\mu\nu} \rightarrow F'_{\mu\nu} = U F_{\mu\nu} U^\dagger \quad (2.10)$$

and is not gauge-invariant. However, what is gauge invariant is the color trace of its square, $F_{\mu\nu}^a F_a^{\mu\nu}$, which enters the QCD Lagrangian. Similarly, the quark part of the Lagrangian also remains unchanged after applying the gauge transformation (2.8).

2.2 Symmetries of quantum chromodynamics

2.2.1 General overview of symmetries

Before discussing symmetries of QCD, we first provide a general overview of continuous symmetries, their consequences for a physical system as well as their different realizations (the discussion is based mostly on Refs. [8, 55]). According to the Noether's theorem [85], global, continuous symmetries can be related to conservation laws. If a given system is invariant under such a symmetry, there exists the corresponding conserved current j^μ ,

$$\partial_\mu j^\mu = 0, \quad (2.11)$$

for which the charge can be defined,

$$N = \int d^3x j^0(t, \vec{x}). \quad (2.12)$$

This charge is also conserved,

$$\frac{dN}{dt} = \int d^3x \partial_0 j^0(t, \vec{x}) = - \int d^3x \partial_i j^i(t, \vec{x}) = 0, \quad (2.13)$$

where it is assumed that fields, and hence the current, vanish at spatial infinity.

In our discussion, we focus on the internal transformation of fields, i.e. transformations for which the space-time coordinates remain unchanged [86]. Under such transformations, the vector of fields $\vec{\phi} = (\phi_1, \dots, \phi_n)$ changes into $\vec{\phi}'$ such that

$$\begin{aligned} \phi'_i(x) &= U(\varepsilon)_{ij} \phi_j(x) \\ &\approx \phi_i(x) + i\varepsilon^a t_{ij}^a \phi_j(x) \end{aligned} \quad (2.14)$$

where U is the transformation matrix corresponding to the symmetry group G and the second approximation holds in case of infinitesimal transformations, $\varepsilon \ll 1$. Generators of G , t^a , are matrices acting in the internal field space (note that they should not be

mistaken with the generators of the gauge group). If the action is invariant under these transformations, a set of conserved currents can be defined, one for each generator of G [8, 55],

$$j_a^\mu = -i \frac{\partial \mathcal{L}}{\partial(\partial_\mu \phi_i)} t_{ij}^a \phi_j, \quad (2.15)$$

and the corresponding charges are

$$N^a = -i \int d^3x \frac{\partial \mathcal{L}}{\partial(\partial_0 \phi_i)} t_{ij}^a \phi_j. \quad (2.16)$$

On the quantum level, the charge conservation implies that the corresponding charge operator commutes with the Hamiltonian,

$$[H, N^a] = 0. \quad (2.17)$$

Moreover, it can be shown that charges satisfy the Lie-algebra relations of the corresponding symmetry group G [55],

$$[N^a, N^b] = i C^{abc} N^c, \quad (2.18)$$

where C^{abc} are the structure constants, i.e. the charges are in fact generators of the symmetry group [8]. Equation (2.17) implies that transformations belonging to G leave the Hamiltonian invariant,

$$U H U^\dagger = H \quad (2.19)$$

with the transformation operator being

$$U = e^{i\varepsilon^a N^a}. \quad (2.20)$$

One of the important consequences of symmetries in quantum mechanics is that the symmetry leads to degeneracy of states. To see this, consider an eigenstate $|a\rangle$ with the energy E_a ,

$$H|a\rangle = E_a|a\rangle. \quad (2.21)$$

Then, the state $|a'\rangle = U|a\rangle$ is also the eigenstate with the energy E_a which can be shown by acting with the transformation operator U on both sides of Eq. (2.21):

$$\begin{aligned} UH|a\rangle &= U(E_a|a\rangle) \\ UH U^\dagger U|a\rangle &= E_a U|a\rangle \\ H|a'\rangle &= E_a|a'\rangle, \end{aligned} \quad (2.22)$$

where the transformation property (2.19) was used. Therefore, the spectrum is degenerate with multiplicities determined by irreducible representations of the symmetry group [8].

These considerations are valid under the assumption that the ground state is invariant under the corresponding symmetry group G . If the ground state is invariant under some symmetry group, then the Hamiltonian is invariant too [87] and hence the spectrum of the theory is degenerate. Such a realization of the symmetry is called the Wigner-Weyl mode [55]. There is also a possibility that the Hamiltonian is invariant under certain symmetry, but the ground state is not. This is the Nambu-Goldstone realization of the symmetry [55] and in this case, one says that the symmetry is spontaneously broken, or hidden. When the symmetry is spontaneously broken, the spectrum of the theory does not follow the pattern seen in Eq. (2.22). Instead, massless particles appear in the system, named Nambu-Goldstone bosons. This idea has been first investigated by Y. Nambu and G. Jona-Lasinio [88–90] and then has been formalized in terms of the Goldstone theorem [91, 92]. The number of Nambu-Goldstone bosons in a system is connected with the group structure of the theory. If the symmetry group G is broken to its subgroup H , which means that the ground state remains invariant under transformations belonging to H , then the number of particle species is $n_G - n_H$, where n_G is the number of generators of the group G and n_H is the number of generators of group H , i.e. the number of Nambu-Goldstone bosons is given by the number of broken generators [55].

If the symmetry is realized in the Wigner-Weyl mode, vacuum expectation values of operators which are not invariant under G have to vanish. To see this, consider an operator \mathcal{O} which transforms non-trivially under the symmetry transformation U , i.e. $\mathcal{O} \neq U\mathcal{O}U^\dagger$. Its vacuum expectation value satisfies [10]

$$\langle \mathcal{O} \rangle = \langle 0 | \mathcal{O} | 0 \rangle = \langle 0 | U^\dagger U \mathcal{O} U^\dagger U | 0 \rangle = \langle 0 | U \mathcal{O} U^\dagger | 0 \rangle \equiv \langle \mathcal{O}' \rangle, \quad (2.23)$$

where the invariance of the ground state was utilized. This holds for any symmetry transformation U and therefore the expectation value $\langle \mathcal{O} \rangle$ has to vanish. In the Nambu-Goldstone phase, however, these equalities are no longer true because the ground state is not invariant under the symmetry group G , $U|0\rangle \neq |0\rangle$. Therefore, a non-invariant operator may have non-zero expectation value which allows to distinguish whether the symmetry is spontaneously broken, or not (a familiar example is the magnetization in the Ising model). Such an operator is called an order parameter [10].

The symmetry may also be broken explicitly, i.e. terms which are not invariant under the symmetry group G may be present in the Lagrangian. In this case, the corresponding currents and charges are no longer conserved. For a discussion related to QCD, it is useful to consider a Lagrangian of the form $\mathcal{L} = \mathcal{L}_0 + \mathcal{L}_1$, where \mathcal{L}_0 is invariant under the symmetry group G , and \mathcal{L}_1 breaks the symmetry explicitly. In this case, the divergence of a current is [55, 93, 94]

$$\partial_\mu j^{\mu,a} = \frac{\partial \delta \mathcal{L}_1}{\partial \varepsilon^a} \quad (2.24)$$

with $\delta\mathcal{L}_1$ being the variance of the explicit breaking term, $\delta\mathcal{L}_1 = \mathcal{L}_1(\vec{\phi}') - \mathcal{L}_1(\vec{\phi})$. This shows how the explicit symmetry breaking is related to the non-conservation of the current [94]. Moreover, the notion of charges is still useful because the commutation relations (2.18) remain satisfied (at the given moment of time), even though charges are time-dependent [8].

2.2.2 Exact and approximate symmetries of the QCD Lagrangian

After providing a general overview of symmetries, we can discuss exact and approximate symmetries of the QCD Lagrangian. To this end, it is convenient to divide it into three parts,

$$\mathcal{L} = \mathcal{L}_{kin} + \mathcal{L}_{mass} + \mathcal{L}_{glue}, \quad (2.25)$$

where

$$\mathcal{L}_{glue} = -\frac{1}{4}F_{\mu\nu}^a F_a^{\mu\nu} \quad (2.26)$$

is the gluon Lagrangian,

$$\mathcal{L}_{kin} = \sum_{f=1}^{N_f} \bar{q}_f i\gamma^\mu D_\mu q_f \equiv \bar{q} i\gamma^\mu D_\mu q, \quad (2.27)$$

is the kinetic term with q being the quark flavor vector and

$$\mathcal{L}_{mass} = \bar{q}\mathcal{M}q, \quad (2.28)$$

the quark mass term, where $\mathcal{M} = \text{diag}(m_1, \dots, m_{N_f})$ is the diagonal quark mass matrix. To make the discussion more general, we consider QCD Lagrangian with an arbitrary number of flavors, N_f .

Apart from the local $SU(3)$ gauge symmetry, QCD is invariant under Poincaré transformations and features a set of discrete symmetries – charge conjugation (C), parity (P) and time reversal (T). For massless quarks, QCD is also invariant under rescaling of fields. The scale invariance, however, is broken by quantum effects [54, 95]. Below, we focus only on global symmetries of QCD which involve continuous transformations of fermion fields and hence we consider transformation properties of Eqs. (2.27) and (2.28). These symmetries are important for the phenomenology of QCD, even though not all of them are exact for the physical number of quark flavors and their masses. We also note that the additional term could be present in the QCD Lagrangian [3, 55],

$$\mathcal{L}_\theta = \frac{g^2\theta}{64\pi^2}\varepsilon^{\mu\nu\rho\sigma}F_{\mu\nu}^a F_{\rho\sigma}^a \quad (2.29)$$

where $\varepsilon^{\mu\nu\rho\sigma}$ is the Levi-Civita tensor and θ is a dimensionless parameter. Its magnitude may be determined experimentally, since for a non-zero value of θ , CP and P symmetries would be broken by strong interactions which could be seen in experiments. Various measurements suggest that $|\theta| \lesssim 10^{-10}$ [4]. The question why this parameter is so small is known as the strong CP problem [96]. Here, we neglect the θ term completely and set $\theta = 0$.

We first consider the global $U(1)$ transformations,

$$q \rightarrow e^{-i\alpha}q, \quad (2.30)$$

due to which each quark field is rotated by a single phase α . Both kinetic and mass terms of the QCD Lagrangian are invariant under this symmetry. The corresponding Noether current is

$$j^\mu = \sum_{f=1}^{N_f} \bar{q}_f \gamma_\mu q_f \equiv \bar{q} \gamma_\mu q \quad (2.31)$$

and the relevant conserved charge is the baryon number. In fact, this symmetry is the special case of a more general symmetry in which each of the flavors is multiplied by a different phase factor,

$$q_f \rightarrow e^{-i\alpha_f}q_f, \quad (2.32)$$

which can be described by the diagonal unitary matrix,

$$U(N_f) = \text{diag}(e^{i\alpha_1}, \dots, e^{i\alpha_{N_f}}), \quad (2.33)$$

acting on the vector in the internal quark flavor space. Such a symmetry leads to the following set of currents,

$$j_f^\mu = \bar{q}_f \gamma_\mu q_f \quad (2.34)$$

(with no summation with respect to f). Therefore, not only a total baryon number is conserved by strong interactions but also each flavor number separately (weak interactions, however, allow for the mixing between flavors [3]).

Next, we consider the global $U(1)$ axial transformations,

$$q \rightarrow e^{-i\alpha\gamma_5}q \quad (2.35)$$

with $\gamma_5 = i\gamma^0\gamma^1\gamma^2\gamma^3$ being the fifth Dirac matrix. The kinetic term is invariant under these transformations, leading to the following Noether current,

$$j_5^\mu = \bar{q} \gamma_\mu \gamma_5 q. \quad (2.36)$$

For the mass term, however, one finds that it transforms as

$$\mathcal{L}'_{mass} = \bar{q}\mathcal{M}e^{-i2\alpha\gamma_5}q, \quad (2.37)$$

and hence it is not invariant under the axial transformations. Therefore, following Eq. (2.24), we can write the divergence of the axial current in the presence of the mass term as

$$\partial_\mu j_5^\mu = 2i\bar{q}\mathcal{M}\gamma_5q. \quad (2.38)$$

Moreover, this symmetry is broken further on the quantum level even for vanishing quark masses, which is known as the axial anomaly [97, 98].

Next, we consider transformations acting in the internal quark flavor space. The $SU(N_f)$ flavor transformations,

$$q \rightarrow e^{-it^a\alpha^a}q, \quad (2.39)$$

where t^a are generators of the $SU(N_f)$ group, leave the kinetic term of the QCD Lagrangian unchanged. This allows to introduce a set of $N_f^2 - 1$ Noether currents,

$$j^{\mu,a} = \bar{q}t^a\gamma^\mu q, \quad (2.40)$$

corresponding to each of generators of the symmetry group. This is not the case for the mass term, which transforms as (up to the lowest order in α^a)

$$\mathcal{L}'_{mass} = \bar{q}\mathcal{M}q - i\alpha^a\bar{q}[t^a, \mathcal{M}]q. \quad (2.41)$$

Hence, it is not invariant under $SU(N_f)$ transformations, except for the special case of equal quark masses for which the mass term is

$$\mathcal{L}_{mass} = m\bar{q}q \quad (2.42)$$

and remains invariant under transformations defined in Eq. (2.39). For quark masses which are not equal, one finds the following divergence:

$$\partial_\mu j^{\mu,a} = i\bar{q}[t^a, \mathcal{M}]q. \quad (2.43)$$

The $SU(N_f)$ axial rotations are defined as,

$$q \rightarrow e^{-it^a\gamma_5\alpha^a}q. \quad (2.44)$$

Similarly to $SU(N_f)$ vector transformations, they leave the kinetic term invariant which allows to introduce the corresponding $N_f^2 - 1$ currents,

$$j_5^{\mu,a} = \bar{q}t^a\gamma^\mu\gamma_5q, \quad (2.45)$$

This symmetry is explicitly broken by finite quark masses – the mass term transforms as

$$\mathcal{L}'_{mass} = \bar{q}\mathcal{M}q - i\alpha^a \bar{q}\{T^a, \mathcal{M}\}\gamma_5 q, \quad (2.46)$$

where $\{a, b\} = ab + ba$ is the anti-commutator. The corresponding divergence is

$$\partial_\mu j^{\mu,a} = i\bar{q}\{T^a, \mathcal{M}\}\gamma_5 q. \quad (2.47)$$

Finally, we discuss the chiral symmetry of QCD. To this end, it is convenient to introduce the left- and right-handed quark fields,

$$\begin{aligned} q_L &= P_L q, \\ q_R &= P_R q, \end{aligned} \quad (2.48)$$

where

$$\begin{aligned} P_L &= \frac{1}{2}(1 - \gamma_5), \\ P_R &= \frac{1}{2}(1 + \gamma_5) \end{aligned} \quad (2.49)$$

are chiral projection operators (acting on the Dirac indices) which satisfy the usual relations: $(P_{L,R})^2 = P_{L,R}$ – idempotence, $P_L P_R = P_R P_L = 0$ – orthogonality, and completeness $P_L + P_R = 1$.

The kinetic term of the QCD Lagrangian, written in terms of right- and left-handed quarks, has the following form,

$$\mathcal{L}_{kin} = \bar{q}_L i \not{D} q_L + \bar{q}_R i \not{D} q_R, \quad (2.50)$$

and the mass term becomes

$$\mathcal{L}_{mass} = \bar{q}_L \mathcal{M} q_R + \bar{q}_R \mathcal{M} q_L. \quad (2.51)$$

Therefore, in the kinetic term, the left- and right-handed quarks decouple while in the mass term they are mixed. One can immediately see that the kinetic term is invariant under independent rotations of the right and left-handed fields,

$$\begin{aligned} q_L &\rightarrow e^{it^a \theta_L^a} q_L, \\ q_R &\rightarrow e^{it^a \theta_R^a} q_R. \end{aligned} \quad (2.52)$$

Invariance under such transformations is called chiral symmetry. In consequence, there are $N_f^2 - 1$ Noether currents corresponding to transformations of the left-handed fields,

$$j_L^{\mu,a} = \bar{q}_L \gamma^\mu t^a q_L \quad (2.53)$$

and $N_f^2 - 1$ currents corresponding to transformations of the right-handed fields,

$$j_R^{\mu,a} = \bar{q}_R \gamma^\mu t^a q_R. \quad (2.54)$$

The corresponding charges are

$$N_L^a = \int d^3x \bar{q}_L \gamma^0 t^a q_L \quad (2.55)$$

and

$$N_R^a = \int d^3x \bar{q}_R \gamma^0 t^a q_R. \quad (2.56)$$

These charges satisfy the following commutation relations [55],

$$\begin{aligned} [N_L^a, N_L^b] &= iC^{abc} N_L^c, \\ [N_R^a, N_R^b] &= iC^{abc} N_R^c, \\ [N_L^a, N_R^b] &= 0 \end{aligned} \quad (2.57)$$

and the last property allows to express the chiral symmetry as the direct product of two independent transformations, $SU(N_f)_L \times SU(N_f)_R$. Chiral right- and left-handed currents can be related to the vector, Eq. (2.40), and axial, Eq. (2.45), currents by the following linear combinations [55].,

$$\begin{aligned} j^{\mu,a} &= j_R^{\mu,a} + j_L^{\mu,a}, \\ j_5^{\mu,a} &= j_R^{\mu,a} - j_L^{\mu,a}. \end{aligned} \quad (2.58)$$

These currents have well-defined transformation properties under the parity ($j^{\mu,a}$ transforms as a vector and $j_5^{\mu,a}$ as a pseudovector), while it is not the case for chiral currents, $j_R^{\mu,a}$ and $j_L^{\mu,a}$. Due to the mixing between left- and right-handed fields, the mass term is not invariant under chiral transformations. Therefore, finite quark masses break the chiral symmetry explicitly and divergences of the corresponding currents are

$$\begin{aligned} \partial_\mu j_L^{\mu,a} &= -i(\bar{q}_L T^a \mathcal{M} q_R - \bar{q}_R T^a \mathcal{M} q_L) \\ \partial_\mu j_R^{\mu,a} &= -i(\bar{q}_R T^a \mathcal{M} q_L - \bar{q}_L T^a \mathcal{M} q_R). \end{aligned} \quad (2.59)$$

For physical quark masses, only transformations described by Eqs. (2.30) and (2.32) leave the QCD Lagrangian invariant, while other symmetries are explicitly broken. Nevertheless, remnants of the broken symmetries may be seen in the hadron spectrum if the breaking strength is small enough. Since vector symmetries cannot be spontaneously broken in QCD [99], it should be possible to group hadrons into multiplets of the $SU(N_f)$ group. If the symmetry was exact, the particles within the multiplet would have the same masses and the mass difference within the multiplet may be seen as a measure of the breaking strength [8].

From Tab. 2.1 one can see a large mass separation between in the quark sector $m_u, m_d \ll m_s \ll m_c, m_b, m_t$ (the origin of such differences cannot be explained by strong interactions and remains unknown [54]). For particles composed of up and down quarks the $SU(2)$ symmetry, called also the isospin invariance, is very weakly broken [8]. The strange quark is much heavier than the up and down ones. Nevertheless, the light baryons and pseudoscalar mesons composed of these particles can be still grouped into (approximate) multiplets of the $SU(3)$ group which was noticed by Gell-Mann [100] and Ne'eman [101] and provided further motivation for development of the quark model [102]. On the other hand, the $SU(4)$ flavor symmetry due to very large mass of the charm quark (compared to up, down and strange) is badly broken [8]. Therefore, the approximate symmetry group of the QCD Lagrangian is $U(1) \times SU_L(3) \times SU_R(3)$. Up, down and strange quarks are commonly called "light" and the remaining ones "heavy" [55]. For studying the low-energy dynamics of QCD, often the masses of heavy quarks are assumed to be infinite (and hence decouple from QCD dynamics) and thus the 3 flavor QCD is considered. Additionally, due to small mass difference between u and d quarks, the additional approximation in which $m_u = m_d$ can be made, called 2 + 1 flavor QCD.

2.3 Spontaneous chiral symmetry breaking

In the previous section we argued that the approximate symmetry group of QCD is $U(1) \times SU_L(3) \times SU_R(3)$, with the chiral symmetry $SU_L(3) \times SU_R(3)$ being broken explicitly by finite masses of light quarks. The remnants of the $SU(3)$ vector symmetry can be seen in the spectrum of light hadrons, which indicates that this symmetry is realized in the Wigner-Weyl mode. On the other hand, the axial part of the chiral symmetry is not observed in the particle spectrum.

To see this, consider QCD with massless quarks and note that the axial charge operator transforms under parity as $P^{-1}Q_AP = -Q_A$ [55]. Therefore, a state $|\phi\rangle = |m, \pi\rangle$ with mass m and parity π is transformed by the axial charge operator to the state $|\phi'\rangle = Q_A|\phi\rangle$ which has the opposite parity. Indeed [55],

$$\begin{aligned} P|\phi'\rangle &= PQ_A|\phi\rangle = PQ_AP^{-1}P|m, \pi\rangle \\ &= -Q_AP|m, \pi\rangle = -\pi Q_A|m, \pi\rangle \\ &= -\pi|\phi'\rangle. \end{aligned} \tag{2.60}$$

Therefore, if the axial symmetry was realized in the Wigner-Weyl mode, a given particle should have its parity partner with the same mass but opposite parity. For massive quarks the axial symmetry is explicitly broken but the mass difference should be small. However, when one considers the spectrum of light hadrons, such degenerate parity partners are not found [8, 55]. This indicates that the chiral symmetry is spontaneously broken – the QCD vacuum is not invariant under axial transformations. The pattern of the breaking

is:

$$SU(3)_L \times SU(3)_R \rightarrow SU(3)_V. \quad (2.61)$$

The spontaneous breaking of chiral symmetry has profound consequences for the low-energy dynamics of QCD. Masses of light pseudoscalar mesons, π , K and η are considerably smaller than masses of other light mesons and baryons ~ 1 GeV. They are, in fact, (pseudo-) Goldstone bosons related to the 8 broken generators of the full symmetry group. For massless quarks, these particles would be massless too, as follows from the Goldstone theorem. Due to explicit breaking by the non-zero quark masses, pseudoscalar mesons are not massless. The scale of the spontaneous chiral symmetry breaking is $\Lambda_\chi = 4\pi f_\pi \approx 1170$ MeV [103], where $f_\pi \approx 93$ MeV is the pion decay constant. This scale provides additional motivation for calling u, d and s quarks "light" – their masses are much below Λ_χ , while masses of c, b, and t quarks are comparable or exceed this scale. Additionally, due to the spontaneous breaking of the chiral symmetry, the expectation values of chiral non-invariant operators may be non-zero. Such operators could be used to define order parameters of chiral symmetry breaking. The simplest of these operators is $\bar{q}q$ and its expectation value is called the quark condensate. LQCD simulations find $\langle \bar{q}q \rangle \sim (-250 \text{ MeV})^3$ [39]. Moreover, several low-energy theorems involving one or more soft pions can be formulated [8, 104], but they will not be discussed there.

2.4 Confinement

2.4.1 Overview

Although the fundamental degrees of freedom in the QCD Lagrangian are quarks and gluons, these particles are not present in the observed hadron spectrum. In fact, all experimental searches of free quarks were not successful [4]. The spectrum of QCD consists of hadrons, which are colorless bound states of quarks and gluons. This peculiar feature of QCD is called confinement and is still not fully understood. Below, we provide a brief overview on this phenomenon.

The intuitive picture of confinement comes from the analysis of experimental measurements of light mesons [105, 106]. It was found [107] that hadrons with the same flavor content follow a linear trajectory when their spin J is plotted against their mass squared m^2 ,

$$J(m^2) = \alpha(0) + \alpha' m^2, \quad (2.62)$$

where $\alpha(0)$ is the intercept with the y -axis and α' is the slope of the trajectory (these trajectories are named "linear Regge trajectories" [105, 108]). This remarkable result can

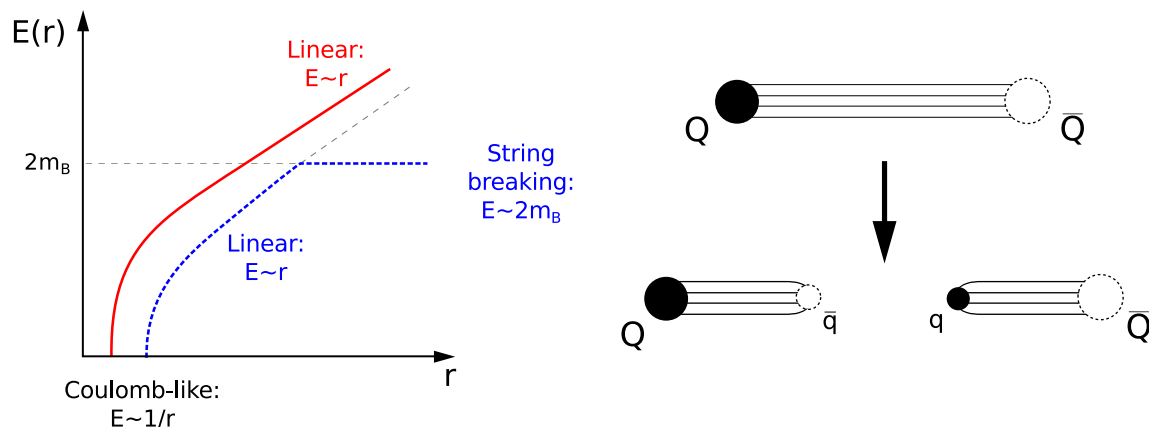


Figure 2.2: Right: The qualitative behavior of the energy of static quark and antiquark pair in the pure gauge theory (the red solid line) and full QCD (the dashed blue line). In the first case, the energy is Coulomb-like at short distances and diverges linearly at large. For QCD, the energy rises linearly until it is more favorable to form a meson-antimeson pair. At large distances $E \sim 2m_B$, with m_B the meson mass. Left: The pictorial representation of the string breaking due to creation of virtual quark-antiquark pair.

be understood in terms of a string model [109] in which quarks are joined by a flux tube with a constant energy density per unit length, σ (known as the string tension).

For simplicity, we consider a meson composed of massless quarks joined by a flux tube of length L , which rotates about the perpendicular axis passing through the middle of the string. Ends of the rotating string move at the speed of light and the energy stored in such a system is [105, 108, 110]:

$$E \equiv m = \frac{1}{2}\pi\sigma L, \quad (2.63)$$

where the factor π arises from the Lorentz contraction, and the corresponding angular momentum is

$$J = \frac{1}{8}\pi\sigma L^2. \quad (2.64)$$

This leads to the linear relation between J and m^2 ,

$$J = \frac{m^2}{2\pi\sigma}. \quad (2.65)$$

The experimental measurements indicate that the string tension has the value of $\approx 0.18 \text{ GeV}^2$ [105].

Equation (2.63) suggests that, at large distances, the energy stored in the quark anti-quark system grows linearly with the separation of particles. The linear growth of the energy can be considered as one of the signals of confinement [106] (in fact, the potential cannot rise faster than $\sim R$ [111]). To gain further insights into physics of confinement, we discuss how the energy of a quark-antiquark pair can be investigated in quantum field theoretical manner, following Refs. [8, 112]. To this end, we consider a system composed of a static quark and anti-quark, placed at the origin and $\vec{R} = (R, 0, 0)$, respectively. The $q\bar{q}$ state can be written as [112]

$$|q(t, \vec{0}), \bar{q}(t, \vec{R})\rangle = \sum_C \psi[C] M[(t, \vec{0}), (t, \vec{R}), C] |0\rangle, \quad (2.66)$$

where the sum runs over paths (C) joining quark and antiquark (which may be seen as a superposition of different states with amplitudes $\psi[C]$), and $M(y, x, C)$ is the static "meson" creation operator which creates a quark at point y and an antiquark at point x ,

$$M[y, x, C] = \bar{q}(y) U(y, x, C) q(x), \quad (2.67)$$

where $U(y, x, C)$ is the so-called Wilson line [36]. It is given by

$$U[y, x, C] = \mathcal{P}_C \exp \left(ig \int_x^y A_\mu(z) dz^\mu \right), \quad (2.68)$$

where C is the path joining x and y and \mathcal{P}_C is the path ordering along C . The appearance of the Wilson line in the meson creation operator $M[y, x, C]$ ensures that the meson states (2.66) are gauge invariant [112] (note that this operator is a $SU(N_c)$ matrix). To investigate the energy of such a meson state, we consider an overlap between two states at different Euclidean times, $t = 0$ and $t' = T$, where for the path C we choose a straight line from 0 to $\vec{R} = (R, 0, 0)$ (and we do not consider other curves),

$$\begin{aligned} \Omega[T, R] &= \langle q(0, \vec{0}), \bar{q}(0, \vec{R}) | q(T, \vec{0}), \bar{q}(T, \vec{R}) \rangle \\ &= \langle 0 | M[(0, \vec{0}), (0, \vec{R}), C]^\dagger M[(T, \vec{0}), (T, \vec{R}), C] | 0 \rangle. \end{aligned} \quad (2.69)$$

On the one hand, by inserting the complete sum over states into the overlap function, one finds

$$\Omega[T, R] = \sum_n |\langle 0 | M[(0, \vec{0}), (0, \vec{R}), C]^\dagger | n \rangle|^2 e^{-E_n T}. \quad (2.70)$$

For large Euclidean time T the lowest energy state, corresponding to the potential energy of the quark-antiquark pair [106], will dominate the sum

$$\Omega[T, R] \sim e^{-E(R)T}, \quad T \rightarrow \infty. \quad (2.71)$$

On the other hand, the overlap function $\Omega[T, R]$ can be also written as

$$\Omega[T, R] \sim e^{-2m_0 T} W[\mathcal{C}], \quad (2.72)$$

where m_0 is the mass of a static quark and

$$W[\mathcal{C}] = \langle 0 | \text{Tr} U[x, x, \mathcal{C}] | 0 \rangle, \quad (2.73)$$

is the so-called Wilson loop [36], which is the vacuum expectation value of the trace of Wilson line calculated around the closed path. In the current discussion, \mathcal{C} is the rectangle joining points $(0, \vec{0})$, $(0, \vec{R})$, (T, \vec{R}) and $(T, \vec{0})$. By combining both expressions for the overlap function, one finds the following relation,

$$W[\mathcal{C}] \sim \exp[-T(E(R) - 2m_0)], \quad (2.74)$$

which links the energy of the static meson with the behavior of the Wilson loop. For a linearly rising energy, $E(R) = \sigma R$, one finds that the Wilson line decreases exponentially with the rate proportional to the area of the rectangle \mathcal{C} ,

$$W[\mathcal{C}] \sim \exp(-\sigma T R). \quad (2.75)$$

These considerations can be generalized to any curve C . Let $A(C)$ be the area enclosed by C and $P(C)$ its perimeter. The Wilson criterion for confinement [36] is the following: the theory is confining if the Wilson loop obeys the area law,

$$W[C] \sim \exp[-A(C)], \quad (2.76)$$

and if there is no confinement, the Wilson loop obeys the perimeter law,

$$W[C] \sim \exp[-P(C)]. \quad (2.77)$$

The Wilson line depends only on the gauge fields and thus allows to investigate confinement even in theory without dynamical quarks, i.e. in the pure gauge limit. The area law of the Wilson line is one of the indicators of confinement [106]. One may also ask whether this phenomenon can be related to some underlying symmetry properties of QCD. In the pure gauge limit this is possible, and the relevant symmetry is the center symmetry – the linear rising of the static quark potential is possible when the system is in center symmetric (i.e. disordered) phase [106]. In this thesis, however, we do not investigate dynamical aspects of (de)confinement but consider models based on properties of the center symmetry (these aspects will be further discussed in the next chapter).

2.4.2 Lattice results on confinement

Lattice simulations allow to study from first principles confinement as well as many other non-perturbative aspects of QCD, and thus are invaluable theoretical tool. In this approach, one considers QCD on the discretized space-time grid [36]. This introduces the ultraviolet cutoff in a natural way, since the largest momentum allowed is of the order

of inverse lattice spacing a [38]. In this approach, the (Euclidean) partition function of QCD, which for the continuous space-time is expressed in terms of the functional integral,

$$Z_{QCD} = \int \mathcal{D}A_\mu^a \mathcal{D}\bar{q} \mathcal{D}q e^{-S_{QCD}^E}, \quad (2.78)$$

is approximated by a $N_\tau \times N_\sigma^3$ -dimensional integral (where N_τ is the number of temporal links and N_σ the number of spatial links) [39]

$$Z_{QCD} \approx \left(\prod_{x,\mu} \int dU_{x,\mu} \right) \det(i\mathcal{D} + \mathcal{M}) e^{-S_{YM}(U)}, \quad (2.79)$$

where $U_{x,\mu}$ are the link variables which represent gluon fields (they are $SU(3)$ matrices) and $\det(i\mathcal{D} + \mathcal{M})$ is the fermion determinant which comes from the integration over quark fields. Since the lattice introduces a UV cutoff, the partition function as well as correlation functions are finite. The resulting multidimensional integrals can be calculated using Monte-Carlo techniques which allows to obtain insights into non-perturbative dynamics of QCD (in vacuum and at finite temperature) after the continuum limit, $a \rightarrow 0$ is taken. Below, we discuss selected lattice results on confinement.

For a pure $SU(3)$ system, lattice simulations found that the quark-antiquark energy diverges linearly with the quark separation [113–115], i.e. the theory is confining. We also note that at short distances, due to the asymptotic freedom, one expects the energy to be Coulomb-like [106]. The behavior of the static quark-antiquark energy $E(R)$ in the pure gauge limit is schematically shown by the red solid line in the left panel of Fig. 2.2. Moreover, the flux tube picture is supported by lattice calculations of the action density for different color groups [116, 117].

When there are dynamical quarks in the system, the flux tube does not extend indefinitely. Dynamical quarks can form a bound state with a static quark (which can be seen as a "meson" composed of a light and static quark), of mass m_B . When the energy stored in the flux tube joining the quark-antiquark pair exceeds $2m_B$, the string breaks and the pair of two mesons is created. This process is schematically shown in the right panel of Fig. 2.2. The energy of a static quark-antiquark pair in this case changes rapidly its behavior from linear to \sim constant and becomes flat at large distances, which is schematically shown by the blue dashed line in the left panel of Fig. 2.2. Therefore, at large separations, one expects the screening of the static quark-antiquark potential. This expectation is confirmed by the lattice simulations for QCD-like theories [115] as well as in QCD (see e.g. Refs. [118–120]).

The string breaking involves a mixing between string-like $q\bar{q}$ states and meson-like states [115, 121, 122]. In the left panel of Fig. 2.3 we show the lattice data [118] on two lowest energy levels of QCD in function of distance, where the energies are normalized to $2m_B$ (the blue dashed line). The energy corresponding to the lowest level, E_1 (the red points), is identified with the quark-antiquark pair energy. One can clearly see the string breaking

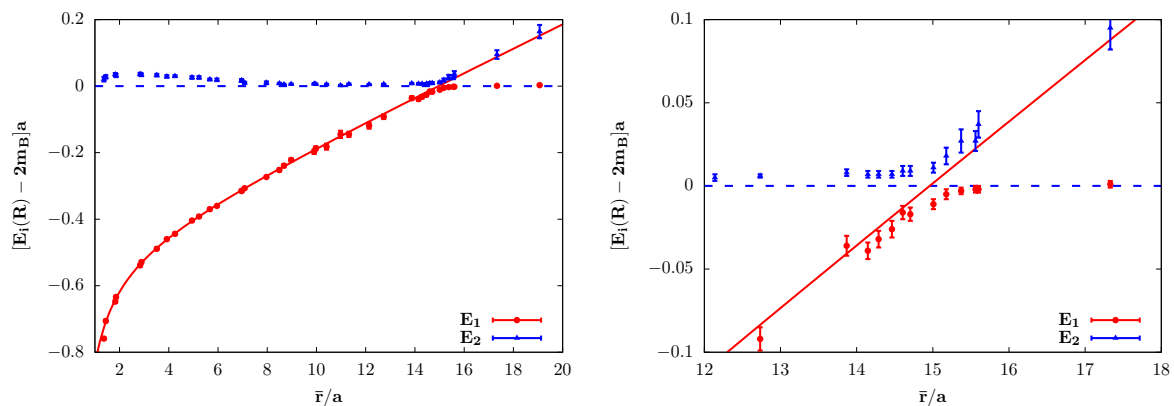


Figure 2.3: Left: The lattice data on energies E_1 (the red dots) and E_2 (the blue squares), corresponding to the two lowest excited states of the QCD Hamiltonian, in function the quark separation. Right: the closeup on the string breaking region. Data obtained from Ref. [118]

phenomenon, i.e. the sudden saturation of the energy. As a consequence of the string breaking, the Wilson line will not obey the area law (2.76) which suggests that there is no confinement in QCD – this is because this operator singles out the lowest energy state. Nevertheless, the quark-antiquark potential may be still seen as confining, which can be seen by looking at the second excited state, E_2 (the blue triangles). Above the string breaking distance, it changes its behavior from approximately constant to linear and data points follow the fit [118] to the confining part of the first energy level (the red solid line). One can also see that energy levels do not simply cross, but there is an energy gap which is related to mixing between two states (the closeup on the string breaking region is shown in the right panel of Fig. 2.3). We also note that both static quarks remain confined in the static-light quark “meson”. In fact, the precise definition of confinement is nontrivial [106] and the complications arising from the string breaking suggest that this phenomenon is most conveniently studied in the pure gauge limit [123].

Chapter 3

Aspects of QCD thermodynamics

In this chapter, we provide an overview of the physics of phase transitions, relevant for our further discussion of QCD thermodynamics. We first discuss general properties of continuous and discontinuous phase transitions. Then, we proceed with the discussion of deconfinement and chiral symmetry restoration – two phase transitions which will be explored in the remaining part of this thesis. Finally, we describe the conjectured QCD phase diagram.

3.1 Phase transitions and critical phenomena

3.1.1 General overview of phase transitions

Phase transitions are ubiquitous in Nature. The familiar examples from everyday life are, for example, boiling of water or melting the ice. However, the change of state of matter is not the only possible type of phase transition. Other possibilities are, for example, changes of the crystal structure of a solid, transition between ferro- and para-magnet or super-fluid transition in the liquid helium. High-energy physics provides the opportunity to investigate phase transitions which are expected to occur at extreme conditions, such as deconfinement or chiral symmetry restoration.

In equilibrium, a phase of matter can be defined as a macroscopic part of a thermodynamic system which has uniform physical properties (e.g. a density, magnetization or crystal structure) and which is separated from other parts (phases) by a phase boundary (for example, the boundary between water and vapor or the boundary between magnetic domains in a ferromagnet). At the phase boundary, some physical properties of the system change discontinuously while others, like temperature, remain constant. The phase transition is an abrupt change of the properties of the system under a small variation of external parameter (usually the temperature), during which one phase changes into

another [124, 125]. Outside the transition region, a small variation of external parameters leads to small change of physical properties of the system [124].

From the mathematical point of view, phase transitions are related to non-analytic properties of thermodynamic potentials. As a consequence, some of their derivatives may be discontinuous at the transition point. This is the cornerstone of the Ehrenfest's classification of phase transitions, according to which the transition is n th order if at least one of n th derivatives of the Gibbs free energy is discontinuous [62, 126]. This classification, however, is not sufficient to capture all the variety of phase transitions and the modern classification simply divides phase transitions into two classes – discontinuous and continuous [62, 125] (nevertheless, the names "first-order" for the former and the "second-order" for the latter remain in use)

First-order transitions, following Ehrenfest's classification, are characterized by discontinuity of first derivatives of thermodynamic potentials. Their characteristic property is non-zero latent heat (the energy which is released, or absorbed, during the transition). In case of continuous transitions, there are no discontinuities of the first derivatives of thermodynamic potentials and nonanalyticities appear in the higher-order derivatives. Points of continuous phase transitions are called critical points [125]. Depending on the dimensionality of the parameter space, higher-dimensional critical surfaces can also be defined.

The fundamental property of continuous transitions is that they can be related to the change of the symmetry of the system [127]. The system changes between the ordered (usually a low-temperature) phase and the disordered one. The symmetry of the disordered phase is larger than the symmetry of the ordered one, which means that the symmetry group of the ordered phase is a subgroup of the symmetry group of the disordered phase. Therefore, such a phase transition is related to the restoration of a spontaneously broken symmetry and different phases can be distinguished by an order parameter.

3.1.2 Statistical mechanics

Methods of statistical mechanics allow to infer the thermal properties of a system from its underlying dynamics, determined by its Hamiltonian, H . For a system which is in the thermal and chemical equilibrium with its surroundings (i.e. it is allowed to exchange both the energy and particles with the reservoir), the fundamental object containing all the thermodynamic information is the grand partition function [128, 129],

$$Z(T, V, \mu) = \text{Tr} e^{-\beta(\hat{H} - \mu\hat{N})}, \quad (3.1)$$

where \hat{N} is a conserved number operator (e.g. the baryon number) and μ is the corresponding chemical potential. Note that in relativistic quantum systems, the total

number of particles is not conserved because of the pair creation and annihilation processes which take place in the medium. The total charge of the system, however, remains constant [129]. From the grand canonical partition function the grand potential can be obtained [128, 129],

$$\Omega(T, V, \mu) = -T \ln Z(T, V, \mu). \quad (3.2)$$

The grand potential is an extensive quantity (it grows proportionally to the system size). Non-analytic properties of thermodynamic functions obtained from the partition function, relevant for phase transitions, can appear only in the thermodynamic limit, in which $V \rightarrow \infty$ and $N \rightarrow \infty$ such that the number density, $n \equiv N/V$, remains constant [126]. It is therefore more convenient to consider the density of the grand potential,

$$\Omega(T, \mu) = \lim_{V \rightarrow \infty} \frac{\Omega(T, V, \mu)}{V} = -\frac{T}{V} \ln Z(T, V, \mu) \quad (3.3)$$

(where used the same symbol for both the grand potential and its density). The grand potential is directly related to the pressure,

$$\begin{aligned} P(T, V, \mu) &= -\frac{\Omega(T, V, \mu)}{V} \\ &= \frac{T}{V} \ln Z(T, V, \mu) \end{aligned} \quad (3.4)$$

and

$$P(T, \mu) = \lim_{V \rightarrow \infty} P(T, V, \mu) = -\Omega(T, \mu). \quad (3.5)$$

From the pressure other thermodynamic quantities can be determined, the entropy density,

$$s(T, \mu) = \left(\frac{\partial P(T, \mu)}{\partial T} \right)_{\mu}, \quad (3.6)$$

the number density,

$$n(T, \mu) = \left(\frac{\partial P(T, \mu)}{\partial \mu} \right)_T, \quad (3.7)$$

and the energy density,

$$\varepsilon = T s - P + \mu n. \quad (3.8)$$

Thermodynamic quantities describe the bulk properties of the system. In addition, its microscopic features can be investigated in terms of the correlation functions. The expectation value of an observable $O(\vec{x})$ in the grand canonical ensemble is defined as [128, 129]

$$\langle O(\vec{x}) \rangle = \frac{1}{Z} \text{Tr} O(\vec{x}) e^{-\beta(\hat{H} - \mu \hat{N})}. \quad (3.9)$$

Similarly, higher order correlation functions can be defined,

$$\langle O(\vec{x}_1)\dots O(\vec{x}_n) \rangle = \frac{1}{Z} \text{Tr} O(\vec{x}_1)\dots O(\vec{x}_n) e^{-\beta(\hat{H}-\mu\hat{N})}. \quad (3.10)$$

The n -point correlation function, however, contains also the information about the lower order correlations as well [62]. To remove these contributions, the connected correlation function is introduced. A very useful example is the two point function, which probes the fluctuations of O ,

$$\langle O(\vec{x}_1)O(\vec{x}_2) \rangle_c = \langle O(\vec{x}_1)O(\vec{x}_2) \rangle - \langle O(\vec{x}_1) \rangle \langle O(\vec{x}_2) \rangle, \quad (3.11)$$

where c stands for ‘‘connected’’. When degrees of freedom become uncorrelated, the connected two-point function as well as the higher-order connected correlation functions vanish. Especially, for studying phase transitions, it is useful to consider correlation functions of the order parameter, $\varphi(\vec{x})$. For large separations, its two-point connected correlation function is expected to fall exponentially,

$$G(\vec{r}) \equiv \langle \varphi(\vec{r})\varphi(\vec{0}) \rangle_c \sim e^{-|\vec{r}|/\xi}. \quad (3.12)$$

Here, ξ is the correlation length which may be understood as a characteristic length scale over which the degrees of freedom are strongly correlated [63].

3.1.3 Continuous phase transitions and critical phenomena

During the continuous phase transition, the system changes continuously between the ordered and disordered phases, distinguished by the order parameter. The Landau theory [127] allows to obtain qualitative insights into these transitions and is often used as a first step for studying phase transitions in a system, before more advanced techniques are employed. In this approach, thermodynamic potentials are generalized to have an explicit dependence on the order parameter, e.g. for the free energy

$$\mathcal{F}(T) \rightarrow \mathcal{F}(T; \varphi). \quad (3.13)$$

At this point, the order parameter can be arbitrary. To determine its physical value, one assumes that it minimizes the Landau free energy, $\mathcal{F}(T; \varphi)$. This condition can be written in terms of the gap equation,

$$\frac{\partial \mathcal{F}}{\partial \varphi} = 0. \quad (3.14)$$

The physical form of the free energy is obtained by substituting the solution of the gap equation into the generalized potential, $\mathcal{F}(T; \varphi(T))$. The important feature of the Landau theory is that the exact form of the potential is not required to obtain qualitative results

about the phase transition in the system. It is assumed that close to the phase transition, the potential can be expanded in terms of the order parameter,

$$\mathcal{F}(\varphi) \approx f_0 + f_1\varphi + f_2\varphi^2 + f_3\varphi^3 + f_4\varphi^4 + \dots, \quad (3.15)$$

where the coefficients of the expansion are determined from symmetry properties of the system, e.g. for a system invariant with respect to $Z(2)$ symmetry, $\varphi \rightarrow -\varphi$, the even-powered terms have to vanish. The generalization to more complicated order parameters is also possible. Therefore, the features of the phase transition in this approach are strongly constrained by the symmetry of the system.

The schematic behavior of the Landau free energy corresponding to a continuous phase transition is shown in the left panel of Fig. 3.1. Below the critical temperature, T_c , the potential has two minima at non-zero values of the order parameter, $\pm\varphi_0$ (the blue dashed line). Physically, only one value of the order parameter can be chosen which indicates that below the critical temperature the symmetry is broken spontaneously. As the temperature reaches T_c both minima continuously approach the single value, $\varphi = 0$ (the black solid line). Above T_c the potential has only one minimum at $\varphi = 0$. The corresponding temperature dependence of the order parameter (the blue solid line, where the positive solution is shown) can be seen in the left panel of Fig. 3.2. As expected, the order parameter vanishes continuously as temperature approaches T_c and is 0 above. The red dash-dotted line is the susceptibility of the order parameter, defined as

$$\chi = \frac{\partial\varphi}{\partial h}, \quad (3.16)$$

where h is the external field conjugate to φ . The susceptibility diverges at the critical temperature and remains finite above and below T_c . We note that while the Landau theory captures qualitative aspects of continuous phase transitions, it is, in general, not sufficient to obtain accurate predictions. This is because the Landau theory is a mean-field theory, i.e. the spatial dependence of the order parameter is neglected, $\varphi(\vec{x}) \approx \varphi_0$. Unless the dimension of the system under consideration is large enough, the mean-field approach predicts wrong critical behavior and to obtain accurate predictions more sophisticated methods which allow to include fluctuations systematically have to be employed [62, 63].

A characteristic feature of continuous phase transitions is the power-law behavior of thermodynamic quantities close to the critical point. It can be characterized by a set of critical exponents,

$$\begin{aligned} C &\sim |t|^{-\alpha}, \\ \varphi &\sim |t|^\beta, \\ \chi &\sim |t|^{-\gamma}, \end{aligned} \quad (3.17)$$

where C is the specific heat and $t = (T_c - T)/T_c$ is the reduced temperature which vanishes at the critical point. At the critical temperature, the behavior of the order

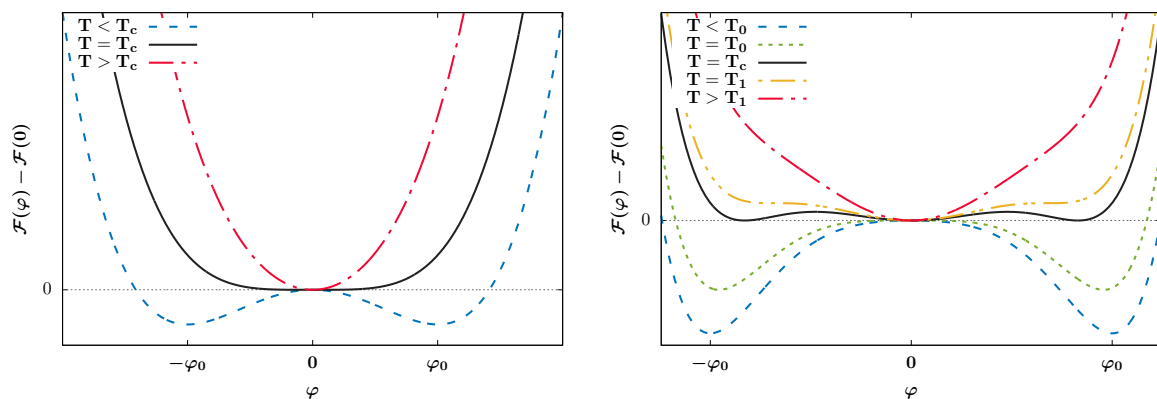


Figure 3.1: The schematic behavior of the Landau free energy in function of the order parameter for the continuous phase transition (the left panel) and for the first-order phase transition (the right panel).

parameter for a small external field is described by the another critical exponent,

$$\varphi \sim |h|^{1/\delta}. \quad (3.18)$$

Two additional exponents can be introduced to describe the behavior of correlation functions near the continuous phase transition. As $T \rightarrow T_c$, the correlation length diverges,

$$\xi \sim |t|^{-\nu}. \quad (3.19)$$

At the critical point, the correlation length is infinite and Eq. (3.12) no longer holds. Instead, the correlation function behaves as

$$G(\vec{r}) \sim \frac{1}{|\vec{r}|^{d-2+\eta}}, \quad (3.20)$$

where d is the number of dimensions of the system. Since η may be seen as a "correction" to the actual number of dimensions, it is also called the anomalous dimension [63].

The critical exponents are not independent but are connected by the so-called scaling relations [62]:

$$\begin{aligned} \alpha + 2\beta + \gamma &= 2, \\ \alpha + \beta(\delta + 1) &= 2, \\ (2 - \eta)\nu &= \gamma, \\ 2 - \alpha &= \nu d, \end{aligned} \quad (3.21)$$

which are known as laws of Rushbrooke, Griffiths, Fisher and Josephson, respectively [62]. Therefore, only two of six critical exponents are independent. This, however, does not

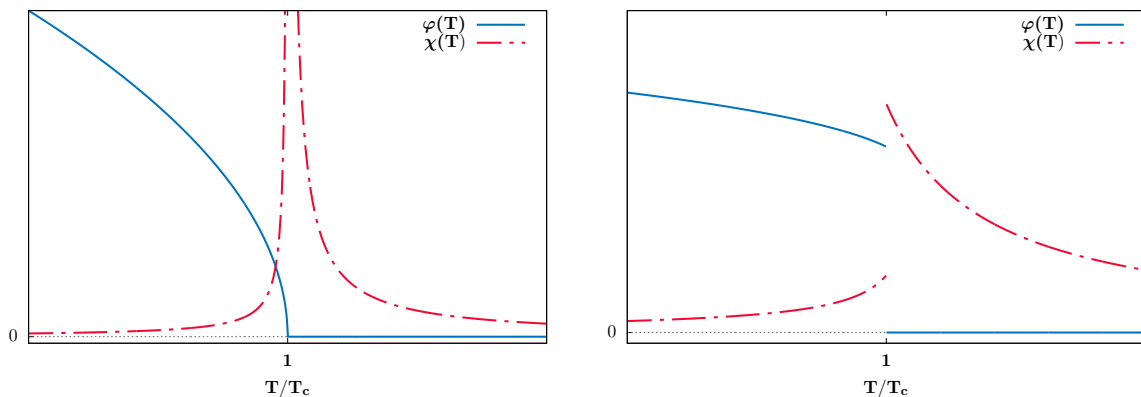


Figure 3.2: The schematic behavior of the order parameter and its susceptibility in function of the reduced temperature T/T_c for the continuous phase transition (the left panel) and for the first-order phase transition (the right panel).

follow directly from thermodynamics and to derive scaling relations additional assumptions on the behavior of the thermodynamic potentials close to critical point have to be made. First two equalities from Eq. (3.21) can be obtained by assuming that the free energy of the system can be decomposed into the regular and singular parts,

$$f(t, h) = f_{reg}(t, h) + f_{sing}(t, h), \quad (3.22)$$

where the regular part is analytic near the critical point and the singular part (also known as the scaling function) is assumed to be a generalized homogeneous function, which means that it has the following property,

$$f_{sing}(\lambda^{a_t} t, \lambda^{a_h} h) = \lambda^p f_{sing}(t, h), \quad (3.23)$$

where p , a_t and a_h are auxiliary parameters and λ is the scaling factor. This assumption on the behavior of the free energy is known as the Widom scaling [130]. The appropriate rescaling and differentiation of the free energy allows to obtain the Rushbrooke and Griffiths laws [62]. The Fisher and Josephson laws can be obtained by assuming that close to the critical point the correlation function is also a generalized homogeneous function,

$$G\left(\frac{r}{\lambda}; \lambda^{a_t} t, \lambda^{a_h} h\right) = \lambda^{2(d-y_h)} G(r; t, h), \quad (3.24)$$

which is known as the Kadanoff scaling [131].

Another important feature of continuous phase transitions is their universality. Systems which undergo continuous phase transitions can be divided into the small number of universality classes which depend on the dimensionality of the system, its symmetries and the dimensionality of the order parameter but are not sensitive to its microscopic

details [62]. Intuitively, this may be understood from the fact that at the critical point the correlation length diverges and the microscopic details of the system, such as structure of particles or lattice spacing, become irrelevant.

3.1.4 First-order phase transitions

The Landau theory may also be used to study first-order phase transitions [132]. A schematic behavior of the Landau free energy which leads to the first-order transition related to the spontaneous symmetry breaking can be seen in the right panel of Fig. 3.1. In this case, the behavior of the thermodynamic potential is more involved than for the continuous phase transitions. Deep in the ordered phase, the free energy has two minima $\pm\varphi_0$ (the blue dashed line). As was the case for the continuous transition, only one value of the order parameter can be realized in the system, and hence the symmetry is broken spontaneously. As the temperature grows, the additional minimum at $\varphi = 0$ begins to form at certain temperature $T = T_0$ (the green dotted line). At first, the energy corresponding to the new minimum is larger than the one corresponding to the non-zero value of the order parameter and hence the latter is more favorable energetically. At the critical temperature, both minima lead to the same value of the free energy, and above T_c the minimum at $\varphi = 0$ becomes energetically favorable. Thus, the order parameter vanishes discontinuously, which corresponds to the first-order transition. Three minima are present until the temperature reaches the specific value T_1 (the yellow double-dot-dashed line) and, finally, for $T > T_1$ the only one minimum at $\varphi = 0$ remains (the red dot-dashed line). The qualitative behavior of the order parameter and its susceptibility can be seen in the right panel of Fig. 3.2. As expected, the order parameter (the blue solid line, where the positive solution is shown) and its susceptibility (the red dot-dashed line) have a discontinuous jump at T_c . Additionally, the susceptibility does not diverge at T_c .

Finally, we note an important feature of the first-order transitions, which is the stability under small perturbations [132]. For example, for a system described by an effective potential, the perturbation may be seen as a term which breaks the symmetry explicitly. In such a case, the transition becomes weaker but remains first-order if the perturbation is small enough. The order parameter, however, is no longer zero above the critical temperature. The transition disappears for sufficiently large perturbation. This should be contrasted with the continuous transitions which turn into crossover even for infinitesimal perturbations.

3.2 QCD phase transitions

3.2.1 Deconfinement

In the previous chapter we discussed the confining property of QCD due to which quarks and gluons in vacuum are bound into colorless hadrons. On the other hand, due to the asymptotic freedom, at very large temperatures the strong coupling is expected to be small and the effective degrees of freedom are in this case quarks and gluons. Deconfinement is the liberation of quarks and gluons from hadrons. Its precise formulation can be given in the pure gauge limit, where it is related to the spontaneous breaking of the center symmetry. To this end, it is convenient to consider a field-theoretical representation of the partition function [129, 133, 134], in which one works in the Euclidean space with the compactified time dimension, $\mathcal{M} = \mathbb{R}^3 \times L$, with $L = [0, \beta)$, $\beta = 1/T$. The partition function in this representation is [129, 133, 134]

$$Z_{QCD} = \int_{\text{periodic}} \mathcal{D}[A_\mu] \int_{\text{anti-periodic}} \mathcal{D}[\bar{q}] \mathcal{D}[q] \exp \left(- \int_0^\beta d\tau \int d^3x \mathcal{L}_{QCD}^E \right) \quad (3.25)$$

where \mathcal{L}_{QCD}^E is the QCD Lagrangian in the Euclidean metric. The trace operation in the partition function (3.1) is in the path integral formulation reflected by the fact that bosonic fields obey periodic boundary conditions in the Euclidean time,

$$A_\mu(\vec{x}, \tau + \beta) = A_\mu(\vec{x}, \tau) \quad (3.26)$$

while fermionic fields are anti-periodic,

$$q(\vec{x}, \tau + \beta) = -q(\vec{x}, \tau) \quad (3.27)$$

which follows from their anti-commuting nature [129, 133, 134]. The periodicity of gluon fields imposes a constraint on gauge transformations, which also have to be periodic [135],

$$U(\vec{r}, \tau + \beta) = U(\vec{r}, \tau). \quad (3.28)$$

These are, however, not the only possible transformations which leave the gluon field periodic in the imaginary time direction. One can also consider "twisted" gauge transformations for which

$$U(\vec{r}, \tau + \beta) = hU(\vec{r}, \tau) \quad (3.29)$$

where h is a constant matrix [56, 136]. In this case, the periodicity condition for the gluon field is

$$A_\mu^U(\vec{x}, \tau + \beta) = h^\dagger A_\mu^U(\vec{x}, \tau) h. \quad (3.30)$$

To satisfy the periodic boundary conditions (3.26), h must commute with A_μ . This requirement can be satisfied if h belongs to the center of the group [135]. We remind that the center of the group is the set of all elements which commute with every other group element. In case of the $SU(N_c)$ group, the center is the set of N_c complex roots of unity,

$$Z(N) = \{1, e^{2\pi i/N_c}, \dots, e^{2\pi(N_c-1)i/N_c}\}. \quad (3.31)$$

The invariance under twisted transformations is called the $Z(N_c)$ (center) symmetry. On the other hand, the quark fields transform under twisted gauge transformations as

$$q^U(\vec{x}, \tau + \beta) = U(\vec{x}, \tau + \beta)q(\vec{x}, \tau + \beta) = -h_c U(\vec{x}, \tau)q(\vec{x}, \tau) = -h_c q^U(\vec{x}, \tau), \quad (3.32)$$

and their boundary conditions (3.27) can be only satisfied if $h_c = 1$. Hence, the presence of dynamical quarks breaks the center symmetry explicitly.

The center symmetry is important because deconfinement in the pure gauge limit can be related to its spontaneous breaking. Indeed, although the QCD action remains invariant under center transformations, there are operators which transform in a non-trivial way and hence can be used to define the order parameter. The simplest example of such operator is the Polyakov loop [56–59],

$$\ell(\vec{r}) = \frac{1}{N_c} \text{Tr}_c L(\vec{r}) \quad (3.33)$$

where

$$L(\vec{r}) = \mathcal{P} \exp \left(ig \int_0^\beta A_4(\tau, \vec{r}) \right) \quad (3.34)$$

is the Wilson line winding around the temporal direction, in which $A_4(\vec{r}, \tau)$ is the 4th component of the gluon field (in the Euclidean space-time) and \mathcal{P} denotes the path ordering. The trace in Eq. (3.33) is taken over color indices. Because $\ell(\vec{r})$ is the trace of the Wilson line, it is invariant under periodic gauge transformations, (3.28). However, it acquires a non-trivial phase when transformed under twisted gauge transformations, (3.29) because the thermal Wilson line $L(\vec{r})$ transforms under gauge transformations as [95],

$$L^U(\vec{r}) = U^\dagger(\vec{r}, \beta)L(\vec{r})U(\vec{r}, 0) = h_c U^\dagger(\vec{r}, 0)L(\vec{r})U(\vec{r}, 0), \quad (3.35)$$

where $U^\dagger(\vec{r}, 0)$ and $U^\dagger(\vec{r}, \beta)$ arise from the lower and upper limits of the integration in (3.33), respectively. Therefore, under the twisted gauge transformation the Polyakov loop transforms as

$$\ell^U(\vec{r}) = z\ell(\vec{x}), \quad (3.36)$$

where z is one of the non-trivial roots of unity. This shows that the Polyakov loop is not invariant under the center symmetry, and hence may be used to define the order parameter of its breaking.

The expectation value of the Polyakov loop can be attributed to the free energy of a static quark immersed in a hot gluon medium [59, 137, 138]. The free energy of a static quark-antiquark pair is given by the correlator of Polyakov loop and its conjugate [137],

$$\langle \ell(0) \bar{\ell}(\vec{r}) \rangle = e^{-F_{q\bar{q}}(\vec{r})/T}. \quad (3.37)$$

Assuming that the cluster decomposition holds, one finds that at large distances

$$\langle \ell(0) \bar{\ell}(\vec{r}) \rangle \xrightarrow{|\vec{r}| \rightarrow \infty} \langle \ell(0) \rangle \langle \bar{\ell}(\vec{r}) \rangle = |\langle \ell(0) \rangle|^2 \quad (3.38)$$

and hence in this case

$$F_{q\bar{q}}(\vec{r}) \xrightarrow{|\vec{r}| \rightarrow \infty} 2F_q \quad (3.39)$$

with the static quark free energy satisfying

$$|\langle \ell \rangle| = e^{-F_q/T}. \quad (3.40)$$

The relation between deconfinement and center symmetry can be now seen. Polyakov loop transforms non-trivially under the center symmetry, see Eq. (3.36). When the system is in the center-symmetric phase, the Polyakov loop expectation value has to vanish. For $T > 0$ this is possible only if the free energy of a static quark is infinite, which is interpreted as confinement [135]. Physically this may be understood as follows: in confined phase the string forms, and the energy stored in a system would diverge as the separation between quark and antiquark pair increases. Assuming that Eq. (3.39) holds, the single quark free energy is infinite. If the center symmetry is broken spontaneously, the Polyakov loop expectation value is not zero. In this case, the free energy of a single quark is finite which is interpreted as deconfinement [135]. The quark-antiquark correlator would saturate at non-zero value at large separations which is caused by the screening of the quark-antiquark potential [19]. Hence, deconfinement in the pure gauge limit can be related to the spontaneous breaking of the center symmetry and Polyakov loop can be considered as an order parameter of the transition.

Having introduced the order parameter of deconfinement, one may ask what are the properties of the transition. The order of the transition can be inferred from symmetry considerations [59, 135, 143, 144]. For the color group $SU(2)$, the center is $Z(2) = \{-1, 1\}$ and the system has the same symmetry as the 2-dimensional Ising model. Owing to the universality, one expects the second order transition. For the color group $SU(3)$, the center is $Z(3) = \{1, e^{2\pi i/3}, e^{4\pi i/3}\}$ which corresponds to rotations by 120° . The model which shares the same symmetry is the 3-dimensional 3-state Potts model [145], for which

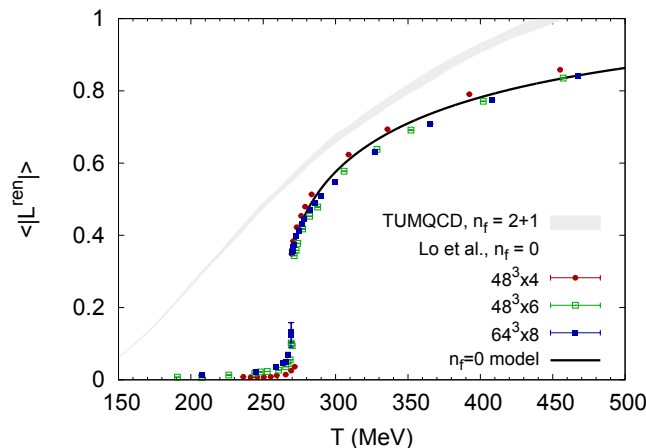


Figure 3.3: Lattice results on the Polyakov loop expectation value in pure $SU(3)$ theory (points, data from Ref. [139]) and 2+1 QCD (gray band, data from Ref. [140]). Solid black line – the result obtained using the effective potential [141].

the first-order phase transition is found [146]. Therefore, deconfinement for three colors is expected to be first-order. These predictions are confirmed by lattice simulations. For two colors, the second order transition has been found [147] and the critical exponents agree with the 3-dimensional Ising model [148]. For the three colors, the transition was confirmed to be first-order [149–151]. For the latter, the deconfinement critical temperature T_d is approximately 270 MeV [39]. The lattice results for the Polyakov loop expectation value in the pure $SU(3)$ theory are shown as colored points in Fig. 3.3 (different symbols correspond to different lattice sizes, the data was obtained from Ref. [139]).

In the presence of dynamical quarks, the center symmetry is broken explicitly. Physically, this means that for a finite quark mass, the string will break at sufficiently large distance, even if temperature is below its critical value [152]. Since first-order transitions are stable with respect to small explicit symmetry breaking, the deconfinement transition may be still discontinuous if quarks are sufficiently heavy and will terminate if quark masses exceed some critical value. For 2 + 1 flavor QCD, the deconfinement phase diagram can be studied with the degenerate up and down quark masses, $m_{u,d}$, and the strange quark mass, m_s , treated as parameters. Such phase diagram is commonly referred to as the Columbia plot [53, 142]. Its schematic representation can be seen in Fig. 5.10. The pure gauge limit is realized in the upper-right corner, corresponding to the infinite quark masses. The deconfinement critical line is expected to belong to the $(Z)_2$ universality class [153]. For the physical quark masses, the center symmetry breaking is strong enough to turn the deconfinement into crossover. Consequently, the Polyakov loop becomes smooth (see the gray band on Fig. 3.3 for the recent lattice QCD results [140]) and is no longer a true order parameter. Nevertheless, it remains useful as it can be seen as a

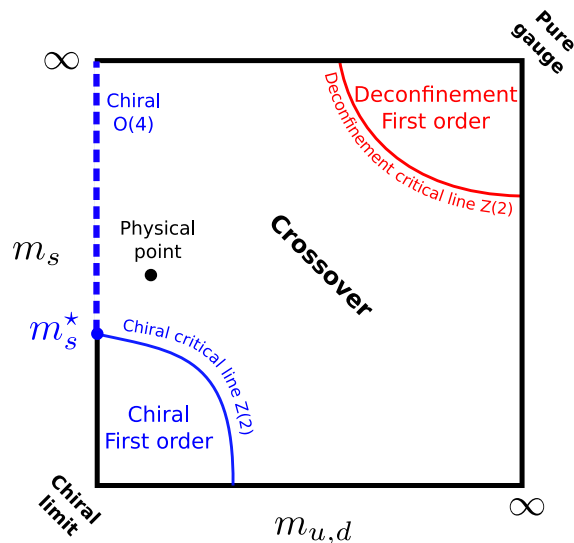


Figure 3.4: The QCD phase diagram in the $(m_{u,d}, m_s)$ plane, also known as the Columbia plot [53, 142]. In lower-left corner quarks are light and chiral transition is expected to be first- or second-order. In the upper-right corner, quarks are heavy and deconfinement becomes a true order transition.

probe of the screening properties of the QCD medium [154].

The gluon dynamics, which is responsible for deconfinement, is highly intricate and our goal in this thesis is not to calculate the Polyakov loop starting from the QCD Lagrangian. In fact, many insights into deconfinement may be obtained by considering effective Polyakov loop models [135, 154]. In this approach, the Polyakov loop is treated as an effective field which represents gluon degrees of freedom. Often, the system is described in terms of an effective Polyakov loop potential, whose functional form is determined by the center symmetry (as we argued above, the symmetry already imposes strong constraints on the order of the transition). The parameters of the potential can be determined from the lattice data [141, 155, 156]. As an example, by the solid black line in Fig. 3.3 we show the result obtained with the effective potential [141] (to be discussed in Chapter 4 in more detail, see also Appendix A). Such potentials are often merged with chiral models which allows to investigate the interplay between deconfinement and chiral physics [155–158].

3.2.2 Chiral symmetry restoration

As we argued in the previous chapter, the chiral symmetry of QCD is spontaneously broken in vacuum. In consequence, the octet of pseudo-Goldstone bosons appears in the spectrum and the quark condensate acquires a finite value. At finite temperature,

the condensate decreases which was observed in the framework of chiral perturbation theory [19, 143] as well as in lattice simulations [39, 40]. At sufficiently large temperature, the condensate melts completely and chiral symmetry becomes restored.

The order of the transition depends on the number of flavors, which can be seen by considering the Landau type effective potential close to the transition region [143, 159]. In this case, the order parameter is the $N_f \times N_f$ matrix in the flavor space, $\Phi_{ij} \sim \langle (\bar{q}_R)_i (q_L)_j \rangle$, and the effective potential in the chiral limit can be written as

$$\Omega \sim g_1 \text{Tr}(\Phi\Phi^\dagger) + g_2 \text{Tr}(\Phi\Phi^\dagger)^2 + g_3 \text{Tr}(\Phi\Phi^\dagger\Phi\Phi^\dagger) + \Omega_{U(1)_A}, \quad (3.41)$$

where the last term is Kobayashi–Maskawa–’t Hooft (KMT) term [160–163],

$$\Omega_{U(1)_A} = g_4(\det \Phi + \det \Phi^\dagger), \quad (3.42)$$

where the determinant acts in the quark flavor space. This term accounts for the breaking of the $U(1)_A$ symmetry while being invariant under the chiral symmetry.

The KMT term determines the order of chiral transition depending on the number of flavors [19]. For three flavors, the determinant introduces a cubic term and hence the transition is expected to be first-order. For two flavors, the determinant is quadratic in fields and the transition is expected to be continuous. In this case, the symmetry group is $SU(2) \times SU(2)$ which is isomorphic to the $O(4)$ group and therefore critical exponents are expected to belong to the $O(4)$ universality class [159].

Since first-order phase transitions are stable under small perturbations, for three flavors there is a range of masses of light and strange quarks for which the chiral transition remains first-order. This can be seen in the lower-left corner of the Columbia plot (Fig. 3.4). For massless up and down quarks the first order transition ends with the tricritical point at the critical mass of the strange quark, m_s^* , and becomes second-order (the blue dashed line along the m_s axis) with $O(4)$ critical exponents [19]. For physical quark masses, the transition is found to be crossover by LQCD simulations [39].

3.3 QCD phase diagram

What is commonly referred to as the QCD phase diagram is the phase diagram of strongly interacting matter plotted in terms of temperature and baryon chemical potential (the latter controls the net-baryon density). In particular, these parameters are relevant for understanding heavy-ion collisions. Here we review the state-of-the-art status of the QCD phase diagram, following Refs. [16, 19].

The conjectured QCD phase diagram is shown in Fig. 3.5. The part which mostly understood is the $\mu_B \ll T$ region which can be explored by lattice methods. At the vanishing

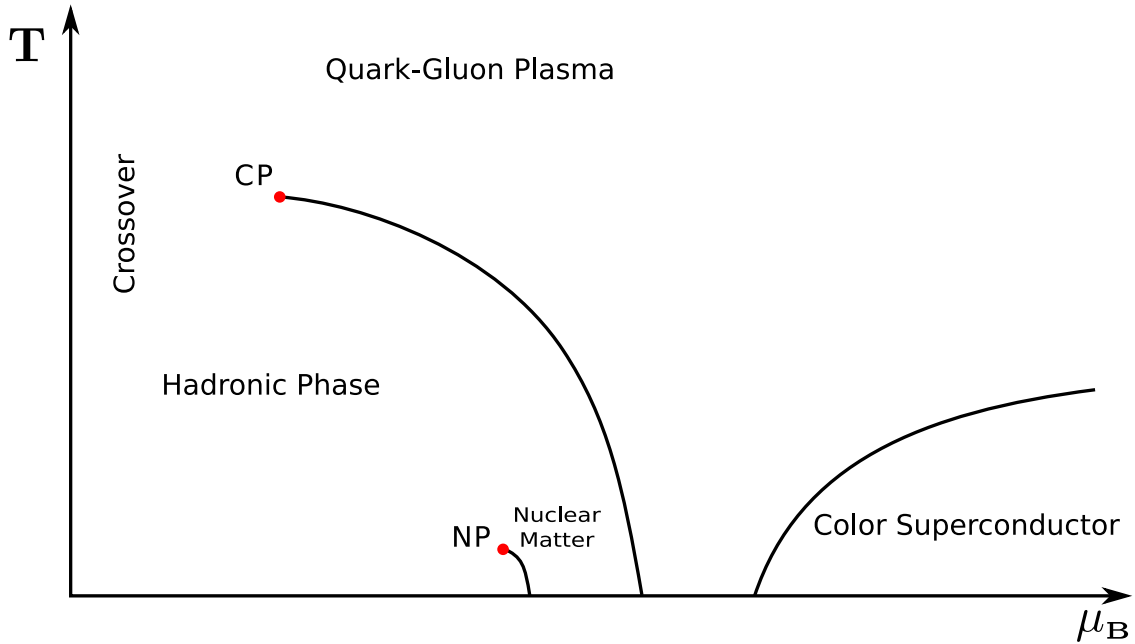


Figure 3.5: The conjectured QCD phase diagram in the (μ_B, T) plane. Two critical points are marked: (1) CP, the conjectured critical point of the chiral phase transition; (2) NP, the critical point of the nuclear liquid-gas transition.

chemical potential, LQCD simulations find that the transition from hadronic matter to QGP is not a real phase transition, but a rapid crossover [40]. In case of the crossover, the order parameter is smooth and the definition of the transition temperature is not unique. For QCD, the up-to-date pseudocritical temperature obtained from the peak of the chiral susceptibility, calculated on the lattice is 158.0 ± 0.6 MeV [164].

For $\mu_B > 0$ the sign problem hinders direct numerical computations. However, there are methods which allows to obtain meaningful results for small chemical potentials. One possibility is to expand observables in the series in terms of μ_B/T and calculate the coefficients at $\mu_B = 0$ [165]. Another way to probe QCD at finite density is to make simulations at imaginary chemical potential, for which the sign problem is absent, and then perform the analytic continuation to the real chemical potential [166, 167]. Lattice simulations find that the pseudocritical temperature decreases with baryon chemical potential [43–45, 45, 46].

Next, we consider the $T \approx 0$ region of the phase diagram. As the baryon chemical potential increases, the first-order nuclear liquid-gas transition takes place at $\mu_{NM} \approx 924$ MeV (which is the difference between nucleon mass $m_N \approx 939$ MeV and the binding energy of the symmetric nuclear matter ≈ 16 MeV [19]). During the transition, the space becomes filled by droplets of nuclear matter and the density changes continuously from

0 to the nuclear saturation density $\rho_0 \approx 0.15 \text{ fm}^{-3}$ [16]. For increasing temperature, the nuclear liquid-gas transition becomes weaker and ends with the critical point at $T \approx 18 \text{ MeV}$ [168–170], with $\mu_{LG \text{ CP}} \approx \mu_{NM}$ [19] (marked by NP on Fig. 3.5). Above NP, liquid and gas phases of nuclear matter are no longer distinguishable. The nuclear matter is a strongly correlated superfluid composed of approximately non-relativistic protons and neutrons [16].

For even larger chemical potentials, the phase structure of QCD remains obscure, as one can rely solely on approximate methods to explore this region of the phase diagram. In fact, many effective models predict the first-order chiral phase transition at $T = 0$ and sufficiently large chemical potential [51, 52]. Since at the vanishing chemical potential LQCD finds that the transition is a smooth crossover, it is natural to anticipate the critical point somewhere in the phase diagram (marked by CP in Fig. 3.5). The strong fluctuations close to the critical point may be visible in heavy-ion collisions [64, 65] and currently there are extensive experimental efforts to constrain its location [60].

For asymptotically large values of baryon chemical potential, $\mu_B \gg \Lambda_{QCD}$, and $T \approx 0$ the QCD medium is weakly coupled [16, 19]. It is expected, in analogy to Bardeen–Cooper–Schrieffer theory of superconductivity [171–173], that in this case the quark matter forms a color-superconducting phase [174–177]. We note that the form of the QCD phase diagram, especially for moderate values of the temperature and chemical potential, may be more complicated than presented here [18, 19]. The detailed discussion of possible phases of QCD and their phenomenological consequences, however, is beyond the scope of this work.

Chapter 4

Polyakov loop fluctuations in the presence of the external fields

In this chapter, we explore deconfinement at vanishing chemical potential and magnetic field using an effective Polyakov loop model. First, we discuss Polyakov loop susceptibilities and their ratios which can be used as additional probes of deconfinement, complementary to the Polyakov loop. Especially, in pure gauge limit ratios of Polyakov loop susceptibilities are robust probes of deconfinement and many of their features can be understood from center symmetry. Next, we discuss results of an effective model study of these observables obtained in Ref. [77]. Especially, it was found that the ratio observables are sensitive to the strength of explicit center symmetry breaking due to presence of dynamical quarks. This suggests that these observables may be used to infer additional information from LQCD, which may be useful for improving effective models of QCD.

4.1 Polyakov loop susceptibilities and ratio observables

4.1.1 Polyakov loop and its fluctuations

In the previous chapter we introduced the Polyakov loop which in the pure gauge limit may serve as an order parameter of the deconfinement, related to the spontaneous breaking of the center symmetry. When calculated on the lattice, Polyakov loop provides insights into non-perturbative dynamics of Yang-Mills theory. Although the detailed discussion of lattice methods is beyond the scope of this thesis, we begin this chapter with a remark about the calculations of the Polyakov loop.

To obtain physical values of observables in LQCD, the lattice spacing, which serves as a UV regulator, should be sent to 0 which is known as the continuum limit. As is usual in

the quantum field theory, when the UV regulator is removed one encounters divergences which, to obtain meaningful results, have to be removed by renormalization. The free energy of a static quark is of no exception – it diverges in the continuum limit and hence the bare Polyakov loop vanishes at all temperatures, since

$$\ell^{bare} = e^{-\beta F_Q^{bare}}. \quad (4.1)$$

The free energy can be renormalized by removing a divergent constant [178, 179],

$$F_Q^{ren} = F_Q^{bare} + C, \quad (4.2)$$

which leads to a multiplicative renormalization for the Polyakov loop,

$$\ell^{ren} = \ell^{bare} e^{-C/T}. \quad (4.3)$$

In fact, the renormalization constant C is scheme-dependent [178, 179] and hence, the Polyakov loop obtained on the lattice is renormalization scheme dependent as well. This calls into question the physical relevance of the deconfinement features deduced from the Polyakov loop, for example, the transition temperature T_d [180, 181] extracted from its inflection point (i.e. from the maximum of $\partial\ell/\partial T$). It is therefore crucial to study the deconfinement from the perspective of different observables and investigate whether a coherent picture can be obtained. One of possibilities is to investigate susceptibilities of Polyakov loop [139, 141]. For $N_c = 3$, the Polyakov loop is complex,

$$\ell = x + iy, \quad (4.4)$$

and one can investigate fluctuations of the real and imaginary parts, which are probed by the corresponding susceptibilities. Following Refs. [139, 141], we will refer to these susceptibilities as longitudinal and transverse, respectively. Thus, the longitudinal susceptibility is defined as

$$T^3\chi_L = VT^3(\langle x^2 \rangle - \langle x \rangle^2), \quad (4.5)$$

and the transverse one is

$$T^3\chi_T = VT^3(\langle y^2 \rangle - \langle y \rangle^2). \quad (4.6)$$

Additionally, the susceptibility of the Polyakov loop modulus can be introduced,

$$\begin{aligned} T^3\chi_A &= VT^3(\langle |\ell|^2 \rangle - \langle |\ell| \rangle^2) \\ &= VT^3(\langle x^2 + y^2 \rangle - \langle \sqrt{x^2 + y^2} \rangle^2), \end{aligned} \quad (4.7)$$

which measures the fluctuations of Polyakov loop modulus,

$$|\ell| = \sqrt{x^2 + y^2}. \quad (4.8)$$

Note that $\langle |L| \rangle \neq \sqrt{\langle x^2 \rangle + \langle y^2 \rangle}$. Similarly to the Polyakov loop, its susceptibilities also require renormalization. The possibility that the renormalization of susceptibilities is also multiplicative served as the motivation to consider their ratios [139, 141]. By taking the ratio, the renormalization factors would in this case cancel. Following Refs. [139, 141], we introduce the ratio of modulus to longitudinal susceptibilities,

$$R_A = \frac{\chi_A}{\chi_L}, \quad (4.9)$$

and the ratio of transverse to longitudinal susceptibilities,

$$R_T = \frac{\chi_T}{\chi_L}. \quad (4.10)$$

These quantities were investigated on the lattice. In the pure gauge limit, ratio observables show the step-function behavior with the discontinuity at the deconfinement temperature, as can be seen in Fig. 4.1 (where the pure gauge data from Ref. [139] is represented by colored points). For the R_T ratio (shown in the left panel) the data is clustered around unity below T_d and becomes smaller than 1 above. This shows that in the deconfined phase, fluctuations in the longitudinal direction are much larger than the fluctuations in the transverse one, while in the confined phase both fluctuations are equal. In case of the R_A ratio (the right panel), the data below deconfinement temperature is clustered slightly above 0.4 and jumps to unity above T_d . This shows that in the pure gauge limit, ratios of Polyakov loop susceptibilities are robust probes of deconfinement.

In the presence of light dynamical quarks, deconfinement is no longer a true phase transition but the analytic crossover. This is reflected in the behavior of ratio observables, which become considerably smoothed [140, 141]. The gray bands in Fig. 4.1 show the recent lattice results on these observables (data from Ref. [140], only the f_0 flow time results are shown). The R_T ratio is close to unity at low temperatures, and decreases monotonically as temperature grows. The R_A ratio stays below one at low temperatures and monotonically increases to one at larger temperatures. Unfortunately, in contrast to the pure gauge case, results of 2+1 QCD simulation are still marred by issues of the renormalization scheme dependence (this issue will be further discussed in Sec. 4.2.5).

In the further part of this chapter, we will investigate ratios of Polyakov loop susceptibilities using the effective model. We argue that they provide useful physical information even in the presence of dynamical quarks. Especially, ratio observables can be related to the strength of explicit center symmetry breaking due to dynamical quarks. To stress their connection with the center symmetry, we first show how the pure gauge results on ratio observables can be inferred from symmetry considerations.

4.1.2 Properties of ratio observables

Properties of ratio observables in the pure gauge theory may be understood with the means of general considerations based on the center symmetry (the discussion below

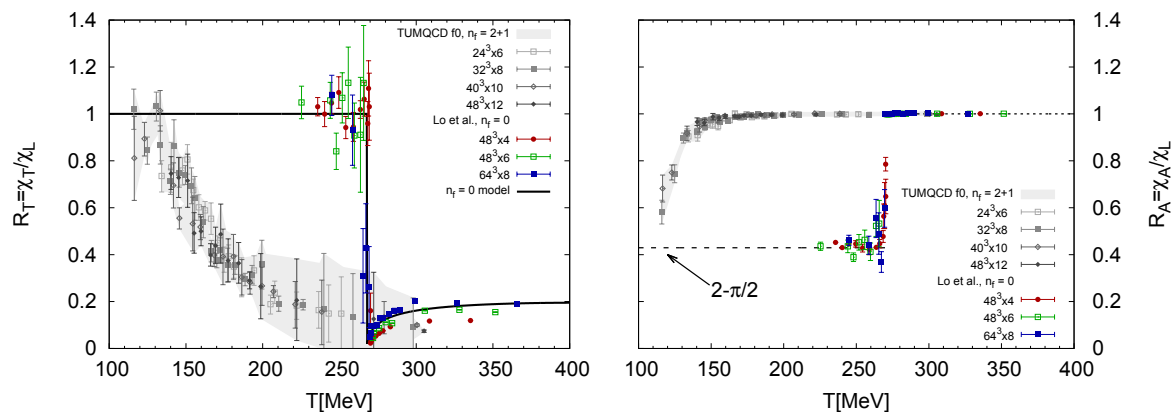


Figure 4.1: Lattice results on the ratio observables R_T (the left panel) and R_A (the right panel). Colored points correspond to the pure gauge data from Ref. [139] and the gray bands to the 2 + 1 QCD data from Ref. [140] (here we show only the f_0 flow time result). The black solid line in the left panel corresponds to the result obtained with the effective potential (4.44). The dashed lines in the right panel correspond to the center symmetry limits (see Sec. 4.1.2).

follows Ref. [139]). In the confined phase, the system is center-symmetric and hence the expectation value of any non-invariant operator, e.g. ℓ or ℓ^2 , vanishes. Therefore,

$$\begin{aligned}
 V(\langle \ell^2 \rangle - \langle \ell \rangle^2) &= V\langle (x + iy)^2 \rangle - V\langle x + iy \rangle^2 \\
 &= V\langle x^2 + 2ixy - y^2 \rangle - V(\langle x \rangle^2 + 2i\langle x \rangle \langle y \rangle - \langle y \rangle^2) = \\
 &= \chi_L - \chi_T = 0,
 \end{aligned} \tag{4.11}$$

where χ_L and χ_T are Polyakov loop susceptibilities defined in Eqs. (4.5) and (4.6), respectively, and we made use of the fact that in the confined phase, expectation values of real and imaginary parts of the Polyakov loop vanish, $\langle x \rangle = \langle y \rangle = 0$. The same holds for the mixed term. Therefore, in the confined phase the longitudinal and transverse susceptibilities are equal,

$$R_T = \frac{\chi_T}{\chi_L} = 1, \tag{4.12}$$

which can be seen in the left panel of Fig. 4.1. We note that to obtain Eq. (4.11) it is sufficient to assume that the distribution function of the Polyakov loop is center-symmetric and otherwise its form can be completely general.

The low-temperature behavior of the R_A ratio can be understood by assuming that deeply in the confined phase the probability distribution for the Polyakov loop is Gaussian, which is sufficient to provide accurate description of the susceptibilities (the behavior of the higher-order correlation functions depends on the higher-order, non-Gaussian, terms in the distribution function). Under this assumption, the partition function can be written

as

$$Z_{Gauss} = \int dx dy e^{-VT^3[\alpha(x^2+y^2)]}, \quad (4.13)$$

where $\alpha > 0$ and the expectation value is defined as

$$\langle O \rangle = \frac{1}{Z_{Gauss}} \int dx dy O(x, y) e^{-VT^3[\alpha(x^2+y^2)]}. \quad (4.14)$$

This form of the partition function will be motivated in Sec. 4.2.1. For the Gaussian distribution, the partition function and susceptibilities can be calculated explicitly. For the former, we find that

$$Z_{Gauss} = \frac{\pi}{\alpha VT^3}. \quad (4.15)$$

For the longitudinal and transverse susceptibilities, one finds

$$\chi_L = \chi_T = \frac{1}{2\alpha T^3} \quad (4.16)$$

which shows explicitly that in the Gaussian approximation $R_T = 1$. To calculate χ_A , defined by Eq. (4.7), the expectation value of Polyakov loop modulus is necessary. In the Gaussian approximation, one finds

$$\begin{aligned} \langle \sqrt{x^2 + y^2} \rangle &= \frac{1}{Z_{Gauss}} \int dx dy \sqrt{x^2 + y^2} e^{-VT^3[\alpha(x^2+y^2)]} \\ &= \frac{1}{Z_{Gauss}} \int_0^{2\pi} d\theta \int_0^\infty d\ell \ell^2 e^{-\alpha VT^3 \ell^2} \\ &= \frac{1}{Z_{Gauss}} \times \pi \times \frac{1}{2} \frac{\sqrt{\pi}}{(\alpha VT^3)^{3/2}} \\ &= \frac{\sqrt{\pi}}{2\sqrt{\alpha VT^3}}. \end{aligned} \quad (4.17)$$

Note that the expectation value of the Polyakov loop modulus is not 0 for finite volumes, even though the system is in the confined phase, $\langle x \rangle = \langle y \rangle = 0$. One can also explicitly see that $\langle |L| \rangle \neq \sqrt{\langle x^2 \rangle + \langle y^2 \rangle}$. The modulus susceptibility in the Gaussian approximation is

$$\chi_A = \frac{1}{2\alpha T^3} \left(2 - \frac{\pi}{2} \right). \quad (4.18)$$

Note that $\chi_A \neq \chi_L + \chi_T$ and $R_A \neq 1 + R_T$ which follows from a non-trivial expectation value of the Polyakov loop modulus. Instead,

$$R_A = 2 - \frac{\pi}{2} \approx 0.429, \quad (4.19)$$

which agrees with the pure gauge lattice result shown in the right panel of Fig. 4.1.

The $R_A \sim 1$ at high temperatures, $T \gg T_d$, which may be understood by expanding the real and imaginary parts of the Polyakov loop around their means,

$$\begin{aligned} x &= x_0 + \delta x, \\ y &= \delta y, \end{aligned} \tag{4.20}$$

where $x_0 = \langle \ell \rangle$ and shifted operators δx , δy describe fluctuations around the expectation value. By definition, $\langle \delta x \rangle = \langle \delta y \rangle = 0$. The longitudinal and transverse susceptibilities can be expressed in terms of the shifted operators as

$$\begin{aligned} \chi_L &= V \langle (\delta x)^2 \rangle_c, \\ \chi_T &= V \langle (\delta y)^2 \rangle_c. \end{aligned} \tag{4.21}$$

The modulus of the Polyakov loop expanded to the leading order in fluctuations is

$$\sqrt{x^2 + y^2} \approx x_0 + \delta x + \frac{1}{2x_0} (\delta y)^2 \tag{4.22}$$

and its expectation value reads

$$\langle \sqrt{x^2 + y^2} \rangle \approx x_0 + \frac{1}{2x_0} \langle (\delta y)^2 \rangle. \tag{4.23}$$

After squaring this expression and neglecting higher order terms one finds

$$\langle \sqrt{x^2 + y^2} \rangle^2 \approx (x_0)^2 + \langle (\delta y)^2 \rangle. \tag{4.24}$$

On the other hand, for the expectation value of the squared Polyakov loop modulus we find

$$\langle x^2 + y^2 \rangle \approx (x_0)^2 + \langle (\delta x)^2 \rangle + \langle (\delta y)^2 \rangle \tag{4.25}$$

and after combining this equation with Eq. (4.24) we arrive at

$$\chi_A \approx V \langle (\delta x)^2 \rangle. \tag{4.26}$$

Therefore, to the lowest order in fluctuations the modulus susceptibility is equal to the longitudinal one, and hence in deconfined phase $R_A \approx 1$, as can be seen in Fig. 4.1.

The value of the R_T ratio at high temperatures is not dictated by the center symmetry [77, 139]. However, it can be related to the color screening properties of the QCD medium. The key observation is that the real and the imaginary parts of the Polyakov loop have distinct transformation properties under the change $A_0 \rightarrow -A_0$ (related to the R-Parity [182]): the real part is even (color magnetic) while the imaginary part is odd

(color electric). In Ref. [183] it has been argued that the imaginary-imaginary correlation function can be used as a gauge invariant way to define a non-Abelian (color) electric screening mass. Polyakov loop susceptibilities can be computed by integrating of the connected correlation functions over volume [138, 184],

$$\chi_{L,T} = \int d^3r \langle l(\vec{r})l(0) \rangle_c \quad (4.27)$$

with $l(\vec{r}) \in \{Re \ell(\vec{r}), Im \ell(\vec{r})\}$, where $\ell(\vec{r})$ is the Polyakov loop field. Therefore, we expect longitudinal and transverse susceptibilities to be sensitive to the color screening properties of the medium (note also the difference between susceptibilities and screening masses, the latter are obtained from the long distance $|\vec{r}| \rightarrow \infty$ behavior of the correlators).

4.2 Modeling Polyakov loop fluctuations

4.2.1 Color group integration

To investigate Polyakov loop fluctuations in the effective model, we calculate the observables using the color group integration scheme [141, 185, 186]. The partition function in this approach is expressed as

$$Z = \int dx dy e^{-VT^3 U[x,y]}, \quad (4.28)$$

where V is the volume of the system, x and y are real and imaginary parts of the Polyakov loop, respectively, and U is the (dimensionless) effective Polyakov loop potential which incorporates effects of both gluon and quark degrees of freedom. This form of the partition is inspired by the Ginzburg-Landau approach for studying phase transitions [62, 132], where the partition function is expressed in terms of the (functional) integral over the order parameter field which is promoted to dynamical degree of freedom,

$$Z_{GL} \propto \int \mathcal{D}\varphi e^{-\beta \int d^3x \mathcal{H}(\varphi)}, \quad (4.29)$$

where the Hamiltonian \mathcal{H} contains, in general, the potential term $\mathcal{U}(\varphi)$ and gradient terms. If the spatial dependence of the order parameter field is weak, the gradient terms can be neglected and the functional integration over order parameter configurations can be replaced with the ordinary integral,

$$Z_{GL} \propto \int d\varphi e^{-\beta V \mathcal{U}(\varphi)}. \quad (4.30)$$

Putting $\mathcal{U}(\varphi) = T^4 U(\varphi)$ leads to the same form of the partition function as in Eq. (4.28).

The thermodynamics of the system in this approach is governed by the form of the effective potential U . In Sec. 4.2.2 we will examine the R_A ratio using the Gaussian potential with the linear $Z(3)$ breaking term (which extends the discussion presented in Sec. 4.1.2), while in Sec. 4.2.3 the physically relevant potential will be studied. In the color group integration approach, expectation values are calculated with the following prescription,

$$\langle \mathcal{O} \rangle = \frac{1}{Z} \int dx dy \mathcal{O}(x, y) e^{-VT^3 U[x, y]}, \quad (4.31)$$

for example, the Polyakov loop expectation value is

$$\langle \ell \rangle = \frac{1}{Z} \int dx dy (x + iy) e^{-VT^3 U[x, y]} \quad (4.32)$$

and its susceptibilities can be calculated following Eqs. (4.5), (4.6) and (4.7).

In the thermodynamic limit, $V \rightarrow \infty$, the exponential factor in the partition function (4.28) is dominated by the minima of the effective gluon potential $U(x, y)$. Therefore, the expectation values x_0 and y_0 can be obtained from the gap equations

$$\begin{aligned} \frac{\partial U(x, y)}{\partial x} &= 0, \\ \frac{\partial U(x, y)}{\partial y} &= 0, \end{aligned} \quad (4.33)$$

and hence in this limit the mean-field results are obtained. Especially, in this limit the longitudinal and transverse susceptibilities can be obtained from the inverse of the curvature matrix,

$$\begin{aligned} T^3 \chi_L &\rightarrow (\mathcal{C}^{-1})_{11} \\ T^3 \chi_T &\rightarrow (\mathcal{C}^{-1})_{22} \end{aligned} \quad (4.34)$$

where \mathcal{C} is the curvature matrix [141, 187], defined as

$$\mathcal{C} = \begin{pmatrix} \frac{\partial^2 U}{\partial x \partial x} & \frac{\partial^2 U}{\partial x \partial y} \\ \frac{\partial^2 U}{\partial y \partial x} & \frac{\partial^2 U}{\partial y \partial y} \end{pmatrix}. \quad (4.35)$$

The curvature matrix is evaluated at the values of x and y obtained from the gap equations (4.33). On the other hand, χ_A in Eq. (4.7) cannot be determined within a mean-field approach, due to the inability to calculate $O(1/V)$ corrections for the quantity $\langle \sqrt{x^2 + y^2} \rangle$ [139]. Nevertheless, the quantity can be readily computed in the current color group integration scheme.

4.2.2 Gaussian model with an explicit symmetry breaking field

In Sec. 4.1.2 we argued the R_A ratio in the confined phase can be understood within the framework of the color group integration with the Gaussian potential,

$$U_0(x, y) = \alpha(x^2 + y^2). \quad (4.36)$$

The Gaussian potential can be readily generalized to include an effect of dynamical quarks by adding an explicit center symmetry breaking term,

$$U_0 \rightarrow U_0 = \alpha(x^2 + y^2) - hx, \quad (4.37)$$

where $h > 0$ controls the strength of the breaking. Note that h can be seen as the external field coupled to the Polyakov loop, in analogy to the coupling observed in the Ising model. As a result, the expectation value of the real part of Polyakov loop becomes non-zero,

$$\langle x \rangle = \frac{h}{2\alpha}, \quad (4.38)$$

while the expectation value of the imaginary part remains 0 and hence the Polyakov loop expectation value is manifestly real. Moreover, the presence of the linear term does not modify the longitudinal and transverse susceptibilities, which have the same form as in Eq. (4.16),

$$\chi_L = \chi_T = \frac{1}{2\alpha T^3}. \quad (4.39)$$

On the other hand, the modulus susceptibility becomes modified in a non-trivial way, which results in the following form of the R_A ratio,

$$R_A = 2 + 2\xi^2 - \frac{\pi}{2} e^{-\xi^2} \times \mathcal{F}[\xi]^2, \quad (4.40)$$

with

$$\mathcal{F}[\xi] = (1 + \xi^2) \times I_0[\xi^2/2] + \xi^2 \times I_1[\xi^2/2], \quad (4.41)$$

where $I_n(x)$ is the modified Bessel function of the first kind. For the Gaussian potential, the R_A ratio is a function of a single effective variable ξ ,

$$\xi = h \times \frac{\sqrt{VT^3}}{2\sqrt{\alpha}}. \quad (4.42)$$

Especially, we find the following asymptotic behavior of R_A for small and large ξ ,

$$R_A = \begin{cases} (2 - \pi/2) \times (1 + \xi^2) & \xi \ll 1 \\ 1 - \frac{1}{4\xi^2} & \xi \gg 1 \end{cases}. \quad (4.43)$$

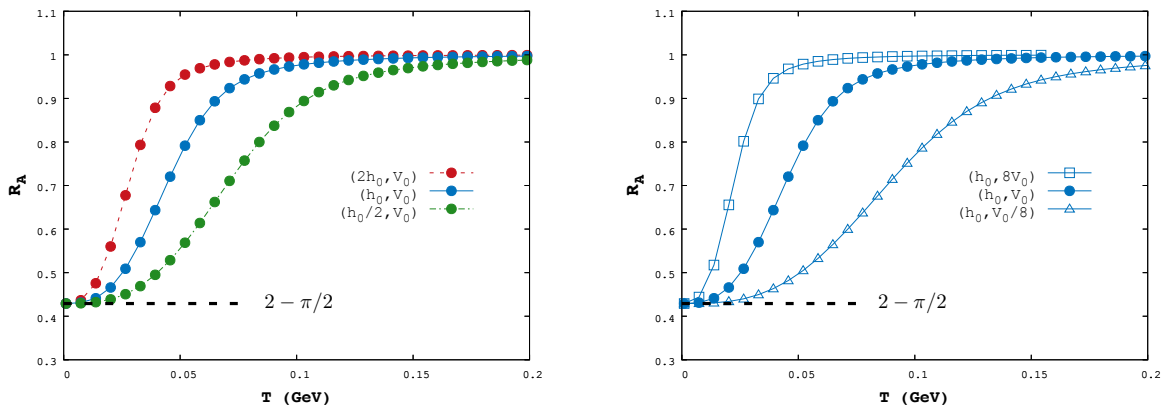


Figure 4.2: The ratio R_A in the Gaussian model as a function of temperature at fixed volume (left) and at fixed explicit symmetry breaking strength (right). We adopt the following scheme in presenting our results: different colors (and line types) correspond to different explicit breaking strengths, while different symbols denote different volumes. In this numerical study, we fix $\alpha = 1$, $h_0 = 1$, and $V_0 = (6.9 \text{ fm})^3$.

To gain some familiarity with the ratio R_A , we examine the quantity as a function of temperature: (1) at fixed volume but for different h , and (2) at fixed h but for different values of the volume. In this numerical study, we fix $\alpha = 1$, $h_0 = 1$, and $V_0 = (6.9 \text{ fm})^3$. The results are shown in Fig. 4.2. As expected, the R_A ratio interpolates between two known limits: from the $Z(3)$ -symmetric phase $R_A = 2 - \pi/2$ to the $Z(3)$ -broken phase $R_A = 1$. At a fixed volume, increasing the breaking strength h makes the ratio approach unity at lower temperature. The quantity also exhibits a strong volume dependence, as seen in the right panel of Fig. 4.2.

In fact, all the results presented in Fig. 4.2 originate from the single expression, Eq. (4.40). In the Gaussian model, the breaking field h always enters via a combination of the volume V and the parameter α dictated by Eq. (4.42). This leads to a difficult situation that as $V \rightarrow \infty$, $R_A \rightarrow 1$, regardless of the value of h and temperatures. To obtain useful information from this quantity, it is necessary to work in a finite volume setting. Alternatively, one can study R_A as function of the scaling variable ξ . We shall revisit some of these issues for the full effective model in the next section.

4.2.3 Polyakov loop potential

The Gaussian model discussed above, although generalized to include an explicit symmetry breaking field, does not describe the spontaneous center symmetry breaking (it gives $R_T = 1$ for all temperatures). To examine the susceptibility ratios in a setting that is relevant to QCD, a Polyakov loop potential [141], capable of handling the latter aspect

will be employed:

$$U_G(\ell, \bar{\ell}, T) = -\frac{A}{2} \times \ell \bar{\ell} + B \ln M_H(\ell, \bar{\ell}) + \frac{C}{2}(\ell^3 + \bar{\ell}^3) + D(\ell \bar{\ell})^2, \quad (4.44)$$

where $M_H(\ell, \bar{\ell})$ is the $SU(3)$ Haar measure,

$$M_H(\ell, \bar{\ell}) = 1 - 6\ell \bar{\ell} + 4(\ell^3 + \bar{\ell}^3) - 3(\ell \bar{\ell})^2, \quad (4.45)$$

and A, B, C and D are temperature-dependent model parameters which were determined from the lattice data on the pure gauge equation of state, renormalized Polyakov loop and its fluctuations [141]. The more detailed discussion of the potential, as well as its parameters, can be found in the Appendix A. To perform calculations within the color group integral scheme, we use

$$\begin{aligned} \ell &= x + iy, \\ \bar{\ell} &= x - iy. \end{aligned} \quad (4.46)$$

The potential U_G in Eq. (4.44) is particularly suited for the current study. Most importantly, the known susceptibilities at zero explicit breaking (i.e. in the pure gauge theory) are reproduced by construction. This is not the case for other commonly used Polyakov loop potentials [155–157]. For example, the polynomial potential introduced in Ref. [155] leads to the result $R_T > 1$ for $T > T_d$, which is the another manifestation of the “negative susceptibility” problem discussed in Refs. [158, 188]. Imposing the Haar measure to the potential [156, 157] effectively restricts the Polyakov loop to the target region and thus improves the theoretical description. In fact, the present model builds on this observation and further constrains the curvatures of the potential using the available LQCD results [139] on the susceptibilities in a pure gauge theory (see the black line in the left panel of Fig. 4.1 for the mean-field result on the R_T ratio).

Furthermore, to model the effect of dynamical quarks we consider a linear explicit breaking term, and thus the potential becomes $U = U_G - h \times x$. The functional form of the breaking field h can be obtained from a one-loop expansion of the fermionic determinant [187, 189]. The latter is given by

$$U_Q = -\frac{2}{T^3} \sum_{f=u,d,s} \int \frac{d^3p}{(2\pi)^3} [\ln g_f^+ + \ln g_f^-] \quad (4.47)$$

with

$$\begin{aligned} g_f^+ &= (1 + 3\ell e^{-\beta E_f} + 3\bar{\ell} e^{-2\beta E_f} + e^{-3\beta E_f}), \\ g_f^- &= (1 + 3\bar{\ell} e^{-\beta E_f} + 3\ell e^{-2\beta E_f} + e^{-3\beta E_f}), \end{aligned} \quad (4.48)$$

where the sum runs over different flavors (up, down and strange) and $E_f = \sqrt{\vec{p}^2 + m_f^2}$. By expanding the full one-loop expression up to a leading order in the Polyakov loop,

one obtains the linear approximation,

$$\begin{aligned}
 U_Q &\approx U_F - \left. \frac{\partial U_Q}{\partial \ell} \right|_{\ell=\bar{\ell}=0} \ell - \left. \frac{\partial U_Q}{\partial \bar{\ell}} \right|_{\ell=\bar{\ell}=0} \bar{\ell} \\
 &\equiv U_F - h \times \frac{\ell + \bar{\ell}}{2},
 \end{aligned} \tag{4.49}$$

where

$$U_F = - \sum_{f=u,d,s} \frac{4}{T^3} \int \frac{d^3p}{(2\pi)^3} \ln(1 + e^{-3\beta E_f}) \tag{4.50}$$

is the leading term, independent of Polyakov loop. Therefore, this term is not relevant for the discussion of the order parameter and its fluctuations and can be omitted (it is important, however, for the proper description of pressure and other thermodynamic quantities). The next term is the linear breaking term $h \times x$, with

$$\begin{aligned}
 h &= \sum_{f=u,d,s} h_Q(m_f, T), \\
 h_Q(T, m) &= \frac{6}{\pi^2 T^3} \int_0^\infty dp p^2 \left(\frac{e^{-E/T} + e^{-2E/T}}{1 + e^{-3E/T}} \right),
 \end{aligned} \tag{4.51}$$

As we aim at understanding the ratios on the qualitative level, we shall allow for an arbitrary prefactor c to manipulate the strength of h . Therefore, the final form of the breaking field (assuming degenerate mass of up and down quarks) is

$$\begin{aligned}
 h &= c \times h_0, \\
 h_0 &= 2 h_Q(T, m_l) + h_Q(T, m_s),
 \end{aligned} \tag{4.52}$$

For quark masses we choose $m_l = 5 \text{ MeV}$ for up and down quarks and $m_s = 100 \text{ MeV}$ for the strange quark. Here the quark masses are constant and the case of the 2+1 flavor PNJL model [155, 157, 158], for which quark masses become medium-dependent, is addressed in Sec. 4.2.5. We stress that our goal is not to model the $Z(3)$ breaking strength with a PNJL-type model. The h_0 introduced here only serves as a reference scale from which we measure the $Z(3)$ breaking strengths of other approaches. We use an arbitrary prefactor c to manipulate the strength of h given by Eq. (4.52). In fact, an attempt will be made to infer the magnitude of this prefactor from the LQCD results on the ratio observables.

In Ref. [187] the critical strength of the breaking field, h_c , for which the phase transition turns from the first-order to the second-order has been calculated. This defines the critical end point (CEP) for the $Z(3)$ transition,

$$h_c = 0.144. \tag{4.53}$$

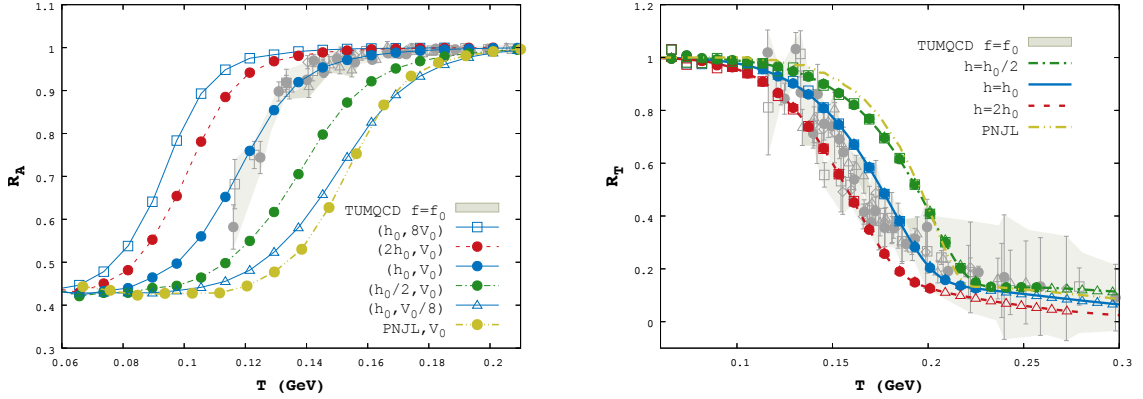


Figure 4.3: The Polyakov loop susceptibility ratio R_A (left) and R_T (right) for the full model Eq. (4.44). We adopt the same presentation scheme as in Fig. 4.2 for the results. The volume independence of R_T is evident: results with different symbols (but the same color) fall on the same line. In this study, h_0 is given in Eq. (4.52), and $V_0 = (6.9 \text{ fm})^3$. The “PNJL” line denotes the result of a PNJL model for $2 + 1$ light flavors described in Sec. 4.2.5. Also shown are the LQCD results at flow time f_0 extracted from Ref. [140].

The breaking field h_0 in Eq. (4.52) exceeds this value for all temperatures of interest, meaning that a crossover transition is expected. This is evident in the ratio observables computed in the full model, as shown in Fig. 4.3. Starting with the R_A ratio, shown in the left panel of Fig. 4.3, we first notice the similarity between the full model results and those from the Gaussian model. Indeed, the R_A ratio interpolates between the two known theoretical limits: $2 - \pi/2 \approx 0.43$ and 1. The expected behaviors from varying the breaking strength and the volume are also verified. Turning now to the R_T ratio, shown in the right panel of Fig. 4.3, the immediate observation is the volume independence of the quantity. This is evident from the fact that results with different symbols (but the same color) all fall on the same line. This suggests that the finite volume $V_0 = (6.9 \text{ fm})^3$ that we selected is sufficiently large. Indeed, we have checked that the ratio R_T approaches the mean-field value, dependent only on the intensive variables T and h . Increasing the breaking strength h makes the ratio deviate from the known $Z(3)$ -symmetric limit $R_T = 1$ at lower temperature. Before proceeding to compare the effective model calculations with LQCD (see Sec. 4.2.5), we first discuss an interesting observation of R_A ratio, namely, a scaling relation inspired by the Gaussian model.

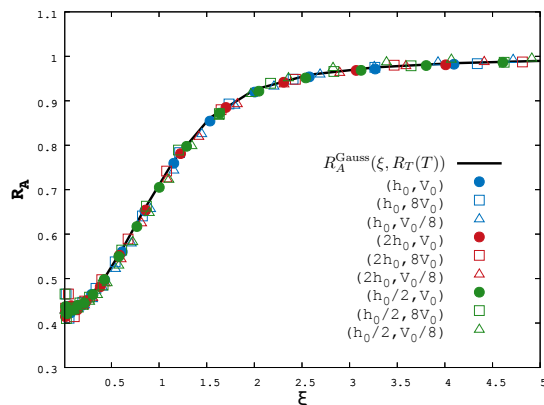


Figure 4.4: The R_A ratio for the full model plotted as a function of the scaling variable ξ (Eq. (4.59)). Model results at various h, V collapse into a single line determined by the generalized Gaussian formula in Eq. (4.57).

4.2.4 Scaling of the R_A ratio

The Polyakov loop potential U_G employed in Eq. (4.44) is clearly non-Gaussian. Nevertheless, we can consider a generalized double-Gaussian approximation to the potential:

$$U_1 = \alpha_1 x^2 + \alpha_2 y^2 - \tilde{h}x, \quad (4.54)$$

where the model parameters α_1 , α_2 , and \tilde{h} are constructed to match

$$\begin{aligned} \alpha_1 &= \frac{1}{2T^3 \chi_L^{(0)}}, \\ \alpha_2 &= \frac{1}{2T^3 \chi_T^{(0)}}, \\ \tilde{h} &= h + \frac{\langle \ell \rangle^{(0)}}{T^3 \chi_L^{(0)}}, \end{aligned} \quad (4.55)$$

with

$$\begin{aligned} T^3 \chi_L^{(0)} &= T^3 \chi_L(T, h = 0, V \rightarrow \infty) \\ T^3 \chi_T^{(0)} &= T^3 \chi_T(T, h = 0, V \rightarrow \infty) \\ \langle \ell \rangle^{(0)} &= \langle \ell \rangle(T, h = 0, V \rightarrow \infty). \end{aligned} \quad (4.56)$$

These coefficients can also be expressed in terms of the parameters of U_G (see Eqs. (A.22) and (A.23)).

It is clear that this approximation scheme operates by constructing a local double-Gaussian potential along the line of minima of U_G . Although this technique is quite

general and can be applied to any potential, it does not replace the real work of constructing a physical potential, since the parameters of the corresponding Gaussian model need to be extracted from the full one. Unlike the full potential, information about the symmetry is lost. Lastly, higher order Polyakov loop correlations are not expected to be well-captured within this approximation. The advantage of performing such an expansion is that it allows for a direct computation of the ratio R_A with an equation analogous to the single Gaussian limit studied previously in Eq. (4.40). The generalized equation reads

$$R_A(\xi, R_T) = 1 + R_T + 2\xi^2 - \frac{2}{\pi} R_T e^{-2\xi^2} [\mathcal{F}(\xi, R_T)]^2, \quad (4.57)$$

where $\mathcal{F}(\xi, R_T)$ can be obtained with an integral involving the modified Bessel function,

$$\mathcal{F}(\xi, R_T) = \frac{1}{\sqrt{\pi}} \int_{-\infty}^{\infty} dx e^{-x^2+2\xi x} \times \frac{x^2}{2R_T} \times e^{\frac{x^2}{2R_T}} \times \left(K_0\left[\frac{x^2}{2R_T}\right] + K_1\left[\frac{x^2}{2R_T}\right] \right), \quad (4.58)$$

where K_n is the modified Bessel function of the second kind of the n th order (for the discussion of $\mathcal{F}(\xi, R_T)$ we refer to the Appendix B of Ref. [77]). According to this equation, the functional dependence in (T, h, V) of the R_A ratio can be uniquely determined by the scaling variable $\xi(T, h, V)$ and $R_T(T, h)$, via

$$\begin{aligned} \xi &= \tilde{h} \times \frac{\sqrt{VT^3}}{2\sqrt{\alpha_1}} \\ R_T &= \frac{\alpha_1}{\alpha_2}. \end{aligned} \quad (4.59)$$

This translates to the following: provided that the generalized Gaussian approximation is valid, all the data points of $R_A(T, h, V)$ will collapse to a single universal line when plotted against ξ , with the choice of a ‘‘physical’’ $R_T = R_T(T, h)$. A direct numerical computation confirms that it is indeed the case, and the result is shown in Fig. 4.4.

While the observation is theoretically interesting, it also indicates a rather limited information contained in this observable. For example, the key information about the magnitude of the explicit breaking field can be as well extracted from the R_T ratio. Nevertheless, Eq. (4.57) may serve as a useful diagnostic tool for analyzing the ratio R_A .

4.2.5 Comparison with LQCD and PNJL model results

As discussed in Sec. 4.1.1, the renormalized Polyakov loop computed by LQCD is a renormalization scheme dependent quantity. This obscures the physical relevance of the derived deconfinement features, e.g., the deconfinement temperature extracted from the

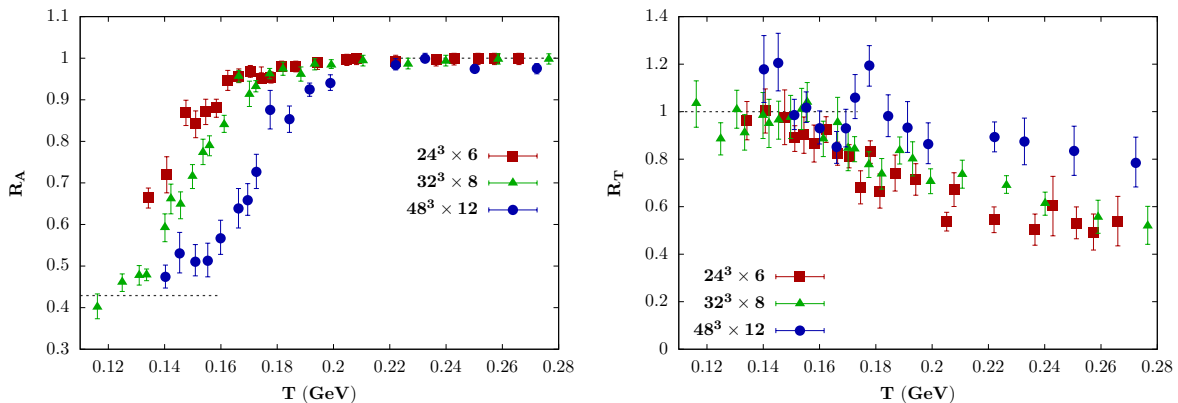


Figure 4.5: The bare LQCD data on Polyakov loop susceptibility ratios R_A (the left panel) and R_T (the right panel) extracted from Ref. [140]. Different symbols correspond to different lattice sizes, $(N_\sigma)^3 \times N_\tau$. The substantial cutoff dependence can be seen for both quantities.

inflection point, and complicates the comparison of LQCD results with those obtained in an effective approach.

One of the original motivations for introducing the susceptibility ratios as probe of deconfinement is the removal of both the cutoff and the scheme dependence. The assumption is that if the Polyakov loop susceptibilities are renormalized in the same way as the Polyakov loop, the multiplicative renormalization factors will be canceled against each other. Contrary to this expectation, recent study [140] reported a substantial cutoff dependence in these ratios in QCD with $2 + 1$ light flavors. This is evident from the N_τ -dependence observed in the “bare data” of R_A and R_T in Ref. [140], which is shown in Fig. 4.5. This seems to suggest that renormalizing the Polyakov loop alone does not guarantee the renormalization of the susceptibilities. In the effective model, the behavior of R_T is largely determined by the explicit breaking field h . It is possible, therefore, that the cutoff dependence observed in R_T can be associated with the cutoff dependence of h . In fact, it is non-trivial to obtain a continuum extrapolation of the explicit breaking strength h from LQCD that is suitable for comparison with effective models [187, 190–193]. Furthermore, if we mimic the N_τ -dependence of the ratio observables as a change of the prefactor in h in the effective model, we can reproduce the same trend in the ordering of curves of R_T and R_A , namely, from top to bottom for R_A in increasing N_τ and the reverse order for R_T (see Fig. 4.5). This suggests that the two sets of “bare” data are connected, and the connection may be due to h .

Using the gradient flow method [140, 179], it is possible to renormalize the susceptibilities and the ratio observables. We have selected LQCD results with the $f = f_0$ flow time to compare with our effective model calculations. They are represented by gray bands in Figs. 4.1 and 4.3. We note that a reasonable agreement between model results and lattice

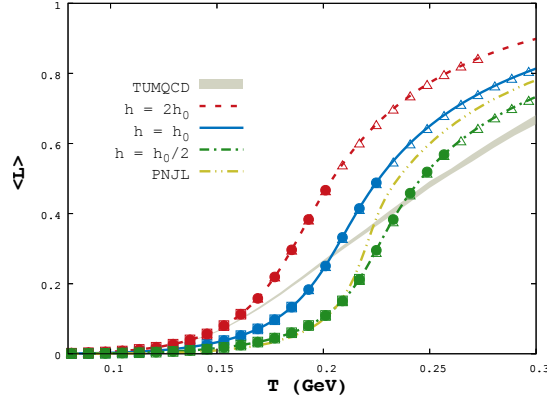


Figure 4.6: Results of the Polyakov loop computed in the model and the LQCD results from Ref. [140]. The “PNJL” line denotes the result of a PNJL model for 2 + 1 light flavors described in Sec. 4.2.5.

data can be attained if we choose an explicit breaking field of strength $\approx (1 - 2) \times h_0$ and a physical volume of $V_0 = (6.9 \text{ fm})^3$, as can be seen in Fig. 4.3.

It is straightforward to extend our study to incorporate effects from the spontaneous chiral symmetry breaking. For this purpose, we study a (2 + 1)-PNJL model, combining the NJL model in Refs. [50, 195] and the Polyakov loop potential U_G in Eq. (4.44). The corresponding effective potential reads

$$U_{PNJL}[\sigma_u, \sigma_d, \sigma_s, x, y] = U_{NJL}[\sigma_u, \sigma_d, \sigma_s] + U_G[x, y] + U_Q[\sigma_u, \sigma_d, \sigma_s, x, y], \quad (4.60)$$

where $\sigma_f \equiv \langle \bar{q}_f q_f \rangle$ is quark condensate for flavor f , U_Q the quark contribution (4.47) and U_{NJL} is the NJL part taken from Refs. [50, 194] given by

$$T^4 U_{NJL}[\sigma_u, \sigma_d, \sigma_s] = 2G(\sigma_u^2 + \sigma_d^2 + \sigma_s^2) - 4K\sigma_u\sigma_d\sigma_s - 6 \sum_{f=u,d,s} \int_{|\vec{p}| < \Lambda} \frac{d^3p}{(2\pi)^3} \sqrt{\vec{p}^2 + M_f^2}. \quad (4.61)$$

In this model, constituent quark masses M_f are linked to current quark masses and

$G\Lambda^2$	$K\Lambda^5$	Λ (GeV)	m_l (GeV)	m_s (GeV)
1.835	12.36	0.6023	0.0055	0.1407

Table 4.1: NJL model parameters used to obtain result seen in Figs. 4.3, 4.6, 4.8 and 4.7 (adopted from Refs. [50, 194]).

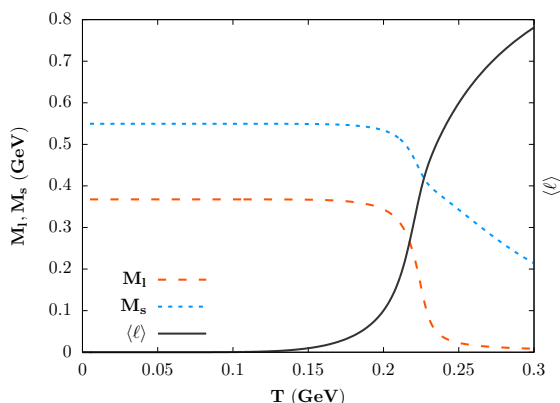


Figure 4.7: Mean-field results on the constituent quark masses and the Polyakov loop obtained with the 2+1 PNJL model (see text for details).

condensates via [195]

$$\begin{aligned}
 M_u &= m_u - 4G\sigma_u + 2K\sigma_d\sigma_s, \\
 M_d &= m_d - 4G\sigma_d + 2K\sigma_u\sigma_s, \\
 M_s &= m_s - 4G\sigma_s + 2K\sigma_u\sigma_d.
 \end{aligned}
 \tag{4.62}$$

Under the mean-field approximation, the expectation values of observables are obtained from the gap equations

$$\frac{\partial U}{\partial \phi} = 0,
 \tag{4.63}$$

with $\phi \in \{\sigma_u, \sigma_d, \sigma_s, x, y\}$. The model parameters are listed in Tab. 4.1. Assuming degenerate light quark masses, $m_u = m_d = m_l$, constituent masses of up and down quarks will be equal. The vacuum values of the light and strange quark masses for the considered set of parameters are

$$\begin{aligned}
 M_l &= 0.37 \text{ GeV} \\
 M_s &= 0.55 \text{ GeV}
 \end{aligned}
 \tag{4.64}$$

and their temperature dependence, together with the Polyakov loop expectation value, can be seen in Fig. 4.7. The computation with the color group integral scheme is similar to the one presented in Sec. 4.2.1, and we simply show the major results in Figs. 4.3 and 4.6 (the yellow double dot-dashed lines). These results can be readily understood by studying an effective $Z(3)$ breaking strength for the PNJL model. It can be computed via Eq. (4.52), except for using the constituent quark masses in place of the current ones. The behavior of such an effective breaking strength compared to h_0 , i.e., the prefactor $c_{PNJL}(T)$ for the PNJL model, is shown in Fig. 4.8. It is evident that the PNJL model leads to a substantially smaller explicit center symmetry breaking, and the observables

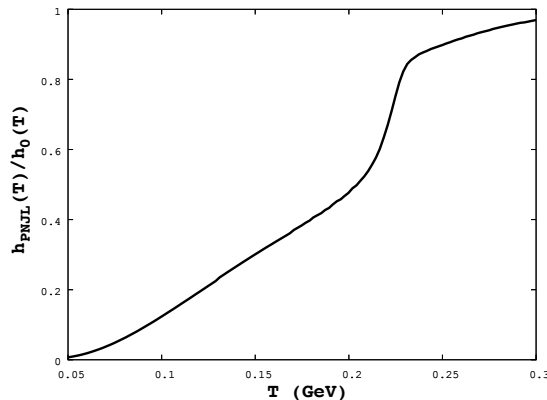


Figure 4.8: The ratio of the effective breaking field, Eq. (4.51), computed using the constituent quark masses obtained in a $(2 + 1)$ -PNJL model to the same quantity computed with the current quark masses. This “prefactor” summarizes the effects of chiral symmetry (within the model) on the explicit $Z(3)$ breaking strength.

R_T and R_A behave accordingly. However, the LQCD results of ratio observables seem to indicate a stronger breaking strength $\approx (1 - 2) \times h_0$. This suggests that a naive implementation of the coupling between quarks and the Polyakov loop, as in the PNJL model, may be inadequate and a more sophisticated treatment including the backreaction of dynamical quarks on the gauge sector, which could modify the Polyakov loop potential U_G , may be necessary.

Furthermore, there is still the substantial “flow time” dependence in ratio observables, reflecting a further renormalization prescription dependence (however, it was observed [140] that the ratio observables exhibit a milder flow time dependence than the susceptibilities). In particular, the large flow time ($f = 3f_0$) result of R_T shows a relatively low value ≈ 0.7 at low temperatures, instead of the expected center-symmetric limit of unity. It is still possible to describe such R_T within our effective model, though it requires a rather large h . This also naturally explains the observation that $R_A \rightarrow 1$ at large flow times. We, however, find this situation unsatisfactory, since it is more natural to expect the physical breaking field h to be free of the renormalization scheme dependence. And it is this quantity that we hope to extract from the LQCD.

For reference, we also computed the Polyakov loop in the effective model and compared with the LQCD result. This is shown in Fig. 4.6. Unlike the case of the ratio observables, we see that the effective model essentially fails to describe the LQCD result. Similar discrepancy has been reported by the matrix model [196]. This may again be due to the scheme dependence of the Polyakov loop.

Chapter 5

Polyakov loop fluctuations in a strong magnetic field and finite chemical potential

In this chapter, we study various aspects of deconfinement in strong magnetic field. Following Ref. [78], we extend the model discussed in the previous chapter to finite magnetic field and explore in details how this parameter enhances the explicit $Z(3)$ symmetry breaking and study its effects on deconfinement in a system with heavy quarks. This leads to a decrease in the (pseudo) critical temperatures and a shrinking first-order region in the phase diagram. We explore the case of dynamical light quarks within the PNJL model and show how the well-known problem of an increasing deconfinement transition temperature can be understood with the current model. We also demonstrate, how the use of a lattice-matched constituent quark mass function can produce instead the trend of a decreasing deconfinement transition temperature with B . Then we show how the lattice trends on deconfinement and chiral transition temperatures can be reproduced in the chiral model with interactions screened by polarization [79, 80]. Finally, we discuss the simultaneous effect of the strong magnetic field and finite chemical potential on deconfinement of heavy quarks, following Ref. [81]. We find that magnetic field and chemical potential have similar effect on Polyakov loop and its fluctuations, the latter, however, leads to splitting between Polyakov loop and its conjugate.

5.1 LQCD results on magnetized QCD

As we argued in the Introduction, studying the interplay between strong interactions and magnetic field may be important for the phenomenology of heavy-ion collisions and neutron stars, and possibly also for understanding the Early Universe. Additional moti-

vation for studying this subject comes from lattice methods. In contrast to the baryon chemical potential, the fermion determinant remains real for finite magnetic field (as long as $\mu_B = 0$) which makes lattice simulations possible even at larger fields [48, 49]. This provides an opportunity to obtain additional information about the non-perturbative dynamics of QCD which may be used, for example, to test the effective model predictions.

Lattice simulations showed that magnetic field influences chiral physics and deconfinement in a non-trivial way. Here, we briefly discuss some of these findings. At low temperature, the magnitude of chiral condensate increases with the magnetic field. Hence, magnetic field enhances the spontaneous chiral symmetry breaking. This effect is known as the magnetic catalysis (MC) [197–200]. Since at low temperatures the magnitude of the chiral condensate increases, one could think that the pseudo-critical temperature of chiral transition would also increase, as the larger temperature would be necessary to melt the condensate. Contrary to this expectation, the opposite trend has been observed on the lattice – magnetic field increases the melting rate of the condensate and, as a result, the pseudo-critical temperature decreases. This effect is known as the inverse magnetic catalysis (IMC) [198, 200–204]. This information is summarized in Fig. 5.1 which shows the schematic behavior of the chiral condensate for the vanishing (blue solid line) and finite (red dashed line) magnetic fields. In fact, it has been argued that the inverse magnetic catalysis may be caused by the competition between the so-called sea and valence contributions [199]. While the valence quarks always enhance the chiral condensate as B increases, the sea quarks are found to reduce it in temperatures near the chiral transition. This reducing effect overtakes the enhancement due to valence quarks, which leads to IMC. It was also observed that IMC is sensitive to the pion mass (or, equivalently, to the quark mass) and vanishes when m_π is large enough [203, 204] which suggests a delicate interplay between magnetic field and strong interactions. Finally, we turn to deconfinement. The pseudocritical temperature of deconfinement decreases with the magnetic field [202–204], which is observed for both light and heavy pions [203, 204].

These findings provided additional tests for effective models. While most effective chiral models (for example the NJL model) can capture the effect of magnetic catalysis, they tend to predict the opposite trend in the magnetic field dependence of the chiral transition temperature [205, 206]. To obtain such effect in model calculations, one usually needs to introduce additional parameter dependence in the effective potentials, e.g., a B -dependent coupling [207, 208], and imposing a specific treatment of the vacuum (and thermal) fluctuations. Another possibility is to consider nonlocal extensions of the PNJL model [209–211]. This is far from ideal as it points to missing interactions (e.g., backreactions, higher-order terms, etc.) that are not captured in the original model, demanding a more careful explicit treatment [154, 212–216]. In fact, even at $B = 0$ a simple implementation of the PNJL model already leads to a substantially higher transition temperature than LQCD. When a running T_d is implemented, the situation improves [206, 212], but the curvatures of the potential and various fluctuations remain to be tested.

An important diagnostic test for the correct form of the potential (rather than a pa-

parameter change) is to examine higher order fluctuations. This allows to investigate not only the B -dependence of the position of the minimum of the potential, but also how the curvature of the potential is affected by the magnetic field. One of the goals of this chapter is to study how magnetic field influences Polyakov loop and its susceptibilities in the effective model. Lattice calculations show that the Polyakov loop generally increases with the magnetic field strength [199–204]. On the other hand, the response of the fluctuations to an external magnetic field has not yet been studied, and one of our goals was to fill this gap.

As the first step, we study Polyakov loop and its fluctuations in the limit of heavy quarks (i.e. the artificial limit where quark masses are large, not to be confused with heavy quarks in the QCD Lagrangian, i.e. c , t , b). To this end, we extended the model discussed in Chapter 4 to a finite magnetic field. The study of deconfinement of heavy quarks is interesting in its own right as it relates to other issues such as the modification of the heavy quark potentials in strong fields [217] and color screening [218]. In addition, restricting to the heavy quarks allows us to avoid the complications from the chiral transitions. This serves as a foundation for setting up a reliable effective gluon potential to further assess the delicate interplay between light quarks and gluons at finite magnetic field.

Next, we explore the case of dynamical light quarks within the PNJL model. The well-known problem of an increasing deconfinement transition temperature with B can easily be understood in our model. We shall also demonstrate how the use of an improved constituent quark mass function, obtained from LQCD data on the chiral condensate, can produce instead the trend of a decreasing deconfinement transition temperature with B . To understand the microscopic origin of IMC, the field-theoretical model which takes into account effects beyond mean-field should be eventually employed. As an example, we discuss the effective model in which four-quark coupling is screened by polarization insertions. Incorporation of such in-medium screening effects leads to T and B dependent coupling. This naturally reduces the chiral transition temperature in PNJL type of models and generates the inverse magnetic catalysis at finite temperatures and magnetic fields. Finally, in the last section of this chapter, we explore the simultaneous effect of finite quark chemical potential and magnetic field on deconfinement in the heavy quark approximation.

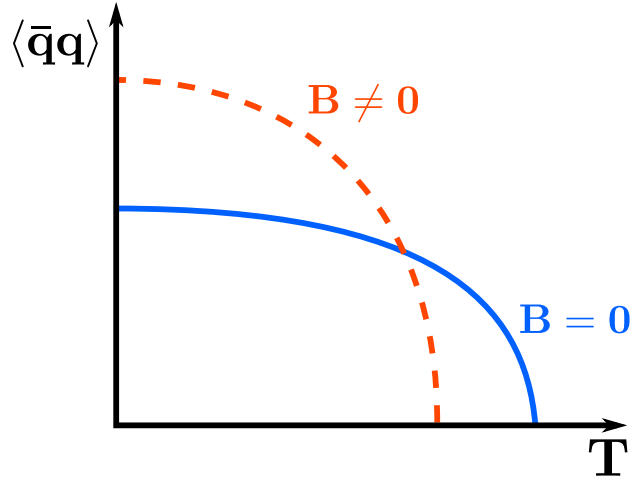


Figure 5.1: The schematic behavior of the chiral condensate for the vanishing magnetic field (the blue solid line) and its non-vanishing value (the red dashed line). At low temperatures the condensate increases with magnetic field which is known as the magnetic catalysis. For larger temperatures the condensate decreases faster for $B > 0$ than for $B = 0$ which is known as the inverse magnetic catalysis.

5.2 Polyakov loop potential at finite magnetic field

5.2.1 Explicit breaking strength in the external magnetic field

To study deconfinement in the strong magnetic field, we model the effective Polyakov loop potential as follows,

$$U = U_G + U_Q, \quad (5.1)$$

where U_G is the pure gauge potential, given by Eq. (4.44), and U_Q describes the explicit center symmetry breaking due to dynamical quarks, given by the one-loop expression (4.47). In the previous chapter, the full one-loop expression was approximated by the linear term $-h \times x$, with h given by Eq. (4.51). In the heavy-quark limit, the higher-order Boltzmann factors can be neglected and the breaking term becomes

$$h_Q(m, T) = \frac{12}{T^3} \int \frac{d^3 p}{(2\pi)^3} e^{-E/T}. \quad (5.2)$$

In this case, the explicit form of the integral can be given,

$$h_Q(m, T) = \frac{6}{\pi^2} \left(\frac{m}{T}\right)^2 K_2(m/T), \quad (5.3)$$

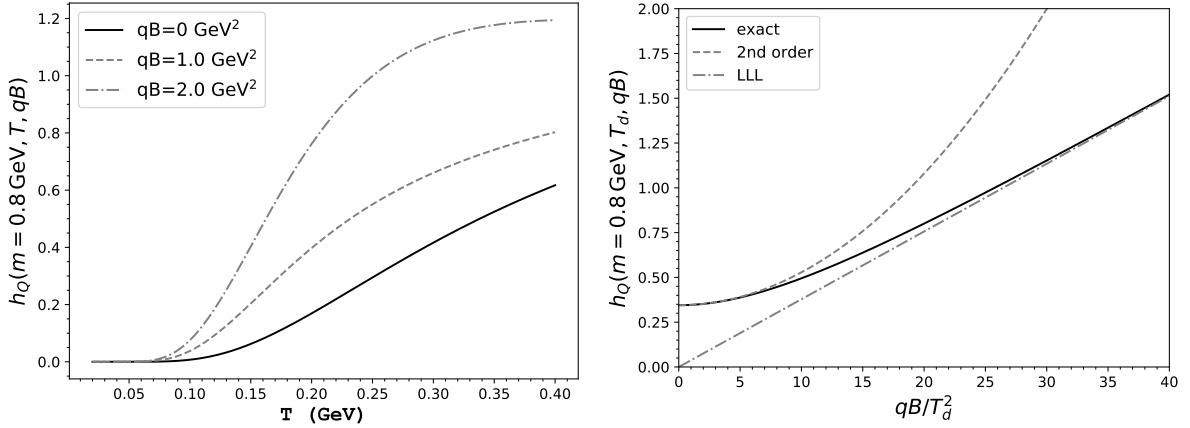


Figure 5.2: Left: the explicit center symmetry breaking field h_Q^B (5.8) in function of temperature at various magnetic field strengths. Right: the magnetic field dependence of h_Q^B at fixed $T_d = 0.27 \text{ GeV}$. The exact numerical result (the solid line) smoothly interpolates between the weak ($O(B^2)$, Eq. (5.10), shown by the dashed line) and strong (LLL, Eq. (5.11), shown by the dot-dashed line) field limits.

where $K_2(x)$ is the modified Bessel function of the second kind. When $m \rightarrow \infty$, the breaking strength vanishes and thus the pure gauge limit is recovered. In the opposite limit, $m \rightarrow 0$, for which one expects the largest breaking strength, $h_{HQ} \rightarrow 12/\pi^2$. This indicates that while the explicit center symmetry breaking strength increases as the quark mass decreases, it does not rise indefinitely, but rather saturates at the maximal value (the same holds for Eq. (4.51), although the limit is slightly different). This should be contrasted with the case of the chiral symmetry breaking, where quark mass serves as the linear breaking field and can be arbitrarily large.

In a constant and homogeneous magnetic field background, the motion of charged particles undergoes the Landau quantization in the transverse plane. Consequently, the dispersion relation becomes modified and takes the following form for spin 1/2 particles [24],

$$E_{f,k,\sigma}^2 = m_f^2 + p_z^2 + (2k + 1 - \sigma)|q_f B|, \quad (5.4)$$

where the subsequent Landau levels are quantified by $k = 0, 1, 2 \dots$ and $\sigma = \pm 1$ (the spin projection on the \vec{B} axis, here: z). In consequence, the sum over states becomes modified as follows [24]

$$2 \int \frac{d^3 p}{(2\pi)^3} \rightarrow \frac{|qB|}{2\pi} \sum_{\sigma=\pm 1} \sum_{k=0}^{\infty} \int \frac{dp_z}{2\pi}, \quad (5.5)$$

where the summation runs over Landau levels and the factor $|qB|/(2\pi)$ accounts for the planar density of each Landau level. As a result, the explicit breaking strength becomes

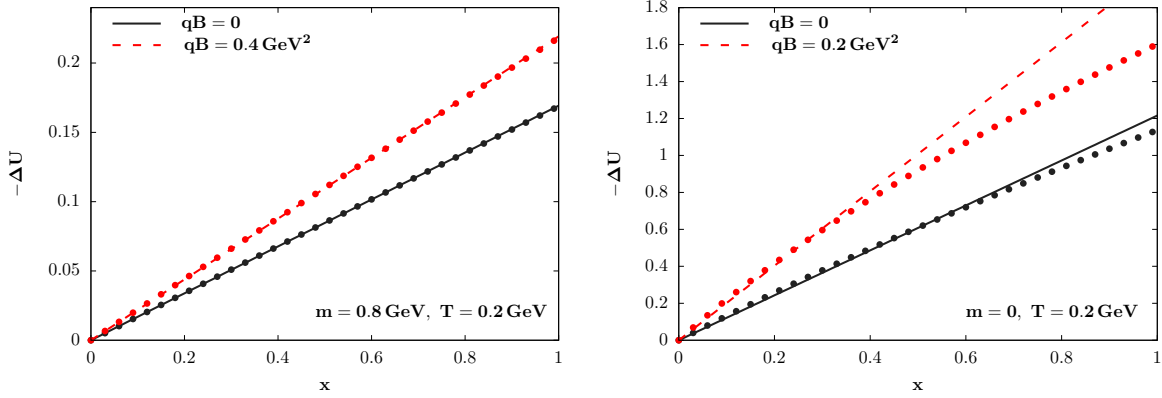


Figure 5.3: Comparison between the full quark potential, (4.47), and its linear approximations with the subtracted purely fermionic contribution U_F , plotted against the expectation value of the Polyakov loop for various values of the magnetic field (see the main text for details). The left panel – heavy quark case with $T = 0.2$ GeV and $m_q = 0.8$ GeV. The right panel – massless quark case with $T = 0.2$ GeV.

a function of the magnetic field,

$$h_{tot.} = \sum_{f=u,d,s} h_Q^B(m_f, T, q_f B), \quad (5.6)$$

where $h_Q^B(m_f, T, q_f B)$ is obtained by applying the prescription (5.5) to Eq. (5.3),

$$h_Q^B(T, qB, m) = \frac{3|qB|}{2\pi^2 T^3} \sum_{\sigma=\pm 1} \sum_{k=0}^{\infty} \int_{-\infty}^{\infty} dp_z e^{-E_{f,k,\sigma}/T}. \quad (5.7)$$

In this approximation, the integration over p_z can be performed analytically, which leads to

$$h_Q^B(T, qB, m) = \frac{3|qB|}{\pi^2 T^3} \sum_{\sigma=\pm 1} \sum_{k=0}^{\infty} M_{k,\sigma} K_1(M_{k,\sigma}/T), \quad (5.8)$$

where

$$M_{k,\sigma}^2 = m^2 + (2k + 1 - \sigma)|qB|. \quad (5.9)$$

The main effect of a finite magnetic field is to increase the strength of explicit center symmetry breaking. This can be seen in the left panel of Fig. 5.2 which shows the typical behavior of the $Z(3)$ breaking field at finite magnetic field for a fixed quark mass $m_q = 0.8$ GeV. For a given B , the increase is more rapid for lower values of m/T .

The numerical computation of Eq. (5.8), or even the full one-loop potential, Eq. (4.47), using the prescription (5.5), is straightforward and has been explored in previous works (see for example Refs. [24, 205]). On the other hand, for an intuitive understanding of

the magnetic field dependence it is instructive to discuss both the weak and strong field limits of the linear breaking term, for massive and massless quarks.

We start with the case of massive quarks. Since h_Q^B is dimensionless, it can be expressed in terms of the dimensionless combinations of m/T and $|qB|/T^2$. The weak field limit ($|qB| \ll m^2, T^2$) is

$$h_Q^B(m, T, qB) \approx \frac{6}{\pi^2} (m/T)^2 K_2(m/T) + \frac{1}{2\pi^2} K_0(m/T) \left(\frac{|qB|}{T^2} \right)^2, \quad (5.10)$$

and strong field limit ($|qB| \gg m^2, T^2$) reads

$$h_Q^B(m, T, qB) \approx \frac{3m|qB|}{\pi^2 T^3} K_1(m/T). \quad (5.11)$$

The weak field limit was obtained by the asymptotic series expansion of the sum, based on the Euler-Maclaurin formula (details as well as higher-order terms can be found in the appendix of Ref. [78]). The leading term corresponds to Eq. (5.3) and the first correction term is quadratic in magnetic field. We note that for a fixed magnetic field, the breaking strength $h_Q^B(m, T, qB)$ for sufficiently large temperatures approaches $h_Q(m, T)$. It can also be seen that the $K_0(m/T)$ factor makes the correction more suppressed for larger quark masses. In the strong field limit, the sum is dominated by the lowest Landau level (LLL), while higher-order terms are exponentially suppressed. Hence, the magnetic field dependence is linear in this limit. The full result obtained by numerical summation interpolates between two asymptotic limits, as can be seen in the right panel of Fig. 5.2.

The explicit breaking field given by Eq. (5.8) is well-defined even in $m \rightarrow 0$ limit. However, its small magnetic field limit cannot be obtained directly from Eq. (5.10) by setting $m \rightarrow 0$, because of the divergence of the K_0 function. For the weak field limit, we find the following result,

$$h_Q^B(m=0, T, qB) \approx \frac{12}{\pi^2} + \frac{1 - 2\gamma_E + 2\ln 2 - 12\zeta'(-1)}{4\pi^2} \left(\frac{|qB|}{T^2} \right)^2 - \frac{1}{4\pi^2} \left(\frac{|qB|}{T^2} \right)^2 \ln \left(\frac{2|qB|}{T^2} \right) - \frac{3\zeta'(-2)}{4\pi^2} \left(\frac{|qB|}{T^2} \right)^3, \quad (5.12)$$

and for the strong field limit we find

$$h_Q^B(m=0, T, qB) \approx \frac{3}{\pi^2} \frac{|qB|}{T^2}. \quad (5.13)$$

Notable are the logarithmic as well as odd-power terms which are found beyond the leading quadratic correction, indicating non-analyticity in $m \rightarrow 0$ limit for the weak-field expansion. In case of the strong magnetic field limit, the dependence is again linear, originating from the LLL (note that this expression can be obtained from Eq. (5.11)

without difficulties). As in $m \neq 0$ case, we refer to the appendix of Ref. [78] for details of the calculation.

To summarize the effects of a finite magnetic field to the center symmetry breaking field: first, it tends to increase the explicit breaking strength. Second, the corrections start with quadratic order in qB for weak fields, and are dominated by the LLL at strong fields. The latter gives a linear dependence. Lastly, the increase is more rapid for light than heavy quarks.

5.2.2 Robustness of the linear approximation

Before proceeding to the results for the order parameter and its fluctuations, we discuss the robustness of the linear approximation. In Chapter 4 the linear breaking strength h_0 served as a reference scale to estimate the LQCD and PNJL breaking strengths, and we did not discuss how well it approximates the full one-loop potential. In this chapter, we intend to study the phase structure of a system with heavy quarks and it is important to check the quality of the linear approximations, Eqs. (5.3) and (5.8). It is expected that they will work for heavy quarks. To examine the efficacy of the approximation, we consider the following quantity,

$$\Delta U(x) = -U_{\text{Breaking}}(x) + U_F, \quad (5.14)$$

which is the difference between the quark contribution, $-U_{\text{Breaking}}$ and the Polyakov loop independent part U_F . For $U_{\text{Breaking}}(x)$ we choose either the full one-loop potential (Eq. (4.47), where the magnetic field dependence can be easily introduced by prescription (5.5)) or the linear approximation (Eqs. (5.3) or (5.8)).

This quantity is shown in Fig. 5.3, where the left panel corresponds to the heavy quark case, $m_q = 0.8 \text{ GeV}$, and the right panel to the case of massless quark. Lines correspond to the linear approximation, and points are the corresponding full one-loop potential results. The temperature is set to $T = 0.2 \text{ GeV}$. For the heavy quark, the linear approximation is robust both for the vanishing magnetic field (the black dots and solid line) and its moderate values ($qB = 0.4 \text{ GeV}^2$, the red dashed line and triangles). In fact, for the range of parameters explored in this chapter, the difference between the full potential and its linear approximation is negligible.

Interestingly, the linear approximation (5.3) is well-describing the full one-loop potential even in the extreme case of massless quark, up to Polyakov loop values $x \lesssim 0.7$ (the solid black line on the right panel of Fig. 5.3). The approximation, however, becomes worse for increasing magnetic fields. For example, we see the substantial deviation of the linear approximation from the full one-loop potential at $qB = 0.2 \text{ GeV}^2$ (the red dashed line), which is a typical field strength when studying chiral transitions [24]. Nevertheless, it is important to remember that the linear approximation is useful in providing the

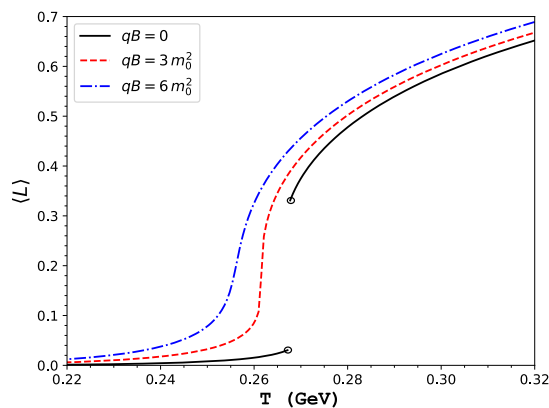


Figure 5.4: Polyakov loop expectation values for $qB/(m_0)^2 = 0, 3$ and 6 (solid black, dashed red and dot-dashed blue lines, respectively) and fixed quark mass $m_q = 1.4m_0$, where $m_0 = 1.1$ GeV. Black circles correspond to the first-order transition.

intuitive understanding of deconfinement physics, which will be evident in the further discussion. In any case, a direct numerical computation of the full one-loop potential is rather straightforward and is always an option for quantitative study. In the next sections, we discuss the effect of the magnetic field on the fluctuation observables.

5.3 Numerical results for heavy quarks at finite magnetic field

5.3.1 Polyakov loop and its fluctuations

As we already mentioned in Sec. 3.1.4, first-order transitions are stable under small perturbations. The center symmetry is explicitly broken by dynamical quarks, but the transition remains discontinuous if quark masses are sufficiently large. For the gluon potential under consideration, the critical quark mass for which deconfinement becomes continuous (i.e. the deconfinement critical point) was studied in Ref. [187]. The breaking strength depends on the number of flavors and the critical mass increases with N_f , since each flavor contributes to the breaking field separately. To study the impact of the strong magnetic field on Polyakov loop and its fluctuations, we consider the single-flavor system (strange quark), since the results obtained for higher number of flavors show, qualitatively, the same behavior. For the single flavor system, the critical quark mass is

$$m_0 = 1.1 \text{ GeV} \quad (5.15)$$

in the absence of other parameters. As we discussed in Sec. 5.2.1, magnetic field enhances the explicit breaking strength and hence it is possible to reach the deconfinement critical

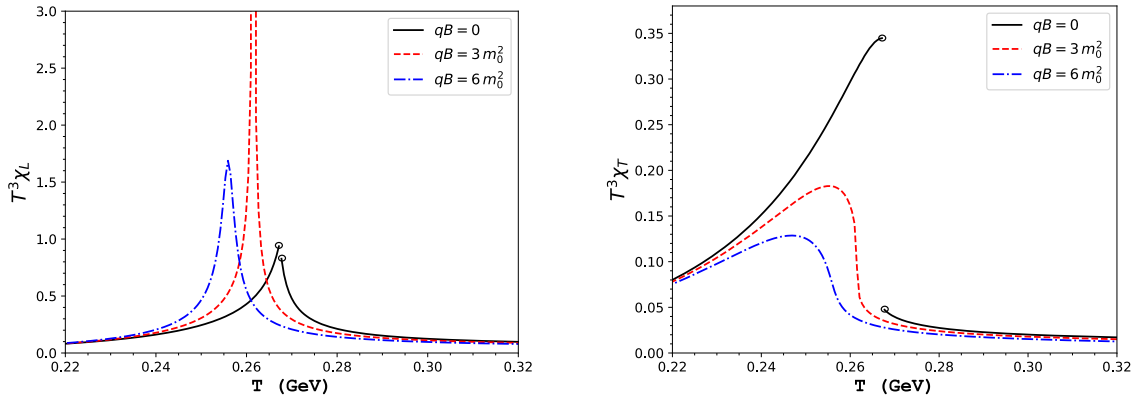


Figure 5.5: The longitudinal (left panel) and transverse (right panel) susceptibilities calculated for $qB/(m_0)^2 = 0, 3$ and 6 (solid black, dashed red and dot-dashed blue lines, respectively) and fixed quark mass $m_q = 1.4m_0$, where $m_0 = 1.1$ GeV. Black circles correspond the first-order transition.

point for masses larger than the critical value, m_0 . To demonstrate it, we show the results for the quark mass $m = 1.4m_0 = 1.54$ GeV and three values of magnetic field, $qB = 0, 3(m_0)^2$ and $6(m_0)^2$.

The Polyakov loop expectation value, obtained by solving the corresponding gap equations, is shown in Fig. 5.4. For the vanishing magnetic field (the black solid line) the transition is discontinuous (since $m_q > m_0$) and hence the system undergoes a first-order transition. For the magnetic field $qB = 3(m_0)^2$, the Polyakov loop becomes continuous (the dashed red line), which indicates the deconfinement critical point. For even larger magnetic fields, deconfinement becomes crossover (the blue dot-dashed line).

Polyakov loop susceptibilities, obtained by inverting the curvature matrix, are shown in Fig. 5.5. The longitudinal susceptibility (the left panel) is discontinuous at the first-order transition (the black solid line), diverges at the critical point (the red dashed line) and has a sharp but finite peak in case of crossover (the blue dot-dashed line). These properties make this observable an excellent tool to investigate deconfinement. A key feature of $T^3\chi_L$ is that it diverges at the critical endpoint – thus, by studying how the magnitude of the peak changes, the critical value of magnetic field can be identified for a given quark mass. Moreover, the position of its peak can be used to define the (pseudo) critical temperature of deconfinement in case of crossover. The transverse susceptibility $T^3\chi_T$ (the right panel of Fig. 5.5) is discontinuous at first-order transition as well (the solid black line). In contrast to χ_L , χ_T does not diverge at a critical point but becomes smooth (the red dashed line). In this model, it decreases gradually with the magnetic field..

Another observable relevant for studying deconfinement is the static quark entropy [140,

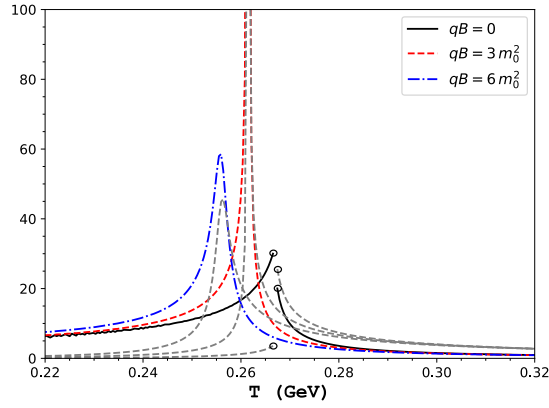


Figure 5.6: The static quark entropy calculated for $qB/(m_0)^2 = 0, 3$ and 6 (solid black, dashed red and dot-dashed blue lines, respectively) and fixed quark mass $m_q = 1.4m_0$, where $m_0 = 1.1$ GeV. Black circles correspond to the first-order transition, and gray dashed lines show the results for $\partial\langle L\rangle/\partial T$.

219], defined as the temperature derivative of the static quark free energy,

$$S_Q = \frac{\partial F_Q}{\partial T}. \quad (5.16)$$

In terms of the Polyakov loop, this quantity reads

$$S_Q = \frac{\partial}{\partial T} T \ln \langle \ell \rangle. \quad (5.17)$$

Static quark entropy was argued to provide a scheme-independent way of defining the critical temperature of deconfinement from tracking its peak [140, 179]. For the current model, the static quark entropy can be seen in Fig. 5.6. We find that the behavior of this quantity is similar to the behavior of the longitudinal susceptibility: it is discontinuous at first-order transition (the black solid line), diverges at the critical point (the red dashed line) and has a sharp but finite peak at the crossover. The similar behavior is observed for the temperature derivative of the Polyakov loop, $\partial\ell/\partial T$ (shown as gray lines in Fig. 5.6). Thus, not only the peak position of $T^3\chi_L$ can be used to define the pseudo-critical temperature, but also maxima of S_Q and $\partial\ell/\partial T$. In particular, T_d extracted from the static quark entropy in 2+1)-QCD was found to be lower than the one extracted from the inflection point of the Polyakov loop. This trend is also observed in the current model, as can be seen in Fig. 5.6. In Tab. 5.1 we show the deconfinement temperatures obtained from peaks of different observables, χ_L , χ_T , S_Q and $d\ell/dT$ for $qB = 0, 3m_0^2$ and $6m_0^2$. We also check what happens in the case of a larger center symmetry breaking: e.g. for light quarks and/or larger B , and generally find the pattern: $T_{\chi_T} < T_{S_Q} \lesssim T_{\chi_L} < T_{inflex.}$. Differences between characteristic temperatures become substantial in this case.

Furthermore, we investigate the impact of the magnetic field on ratios of Polyakov loop susceptibilities. The ratio R_T is obtained from the mean-field susceptibilities $T^3\chi_L$ and

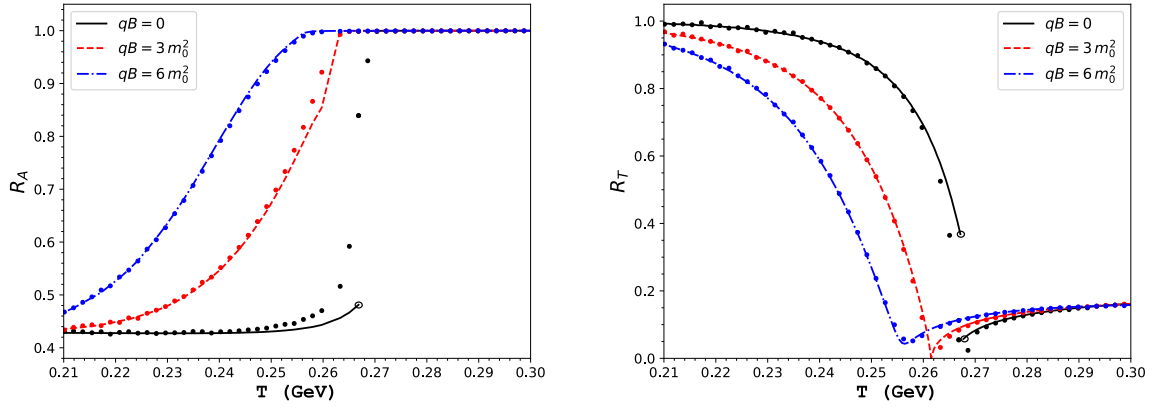


Figure 5.7: R_A (left panel) and R_T (right panel) ratios of Polyakov loop susceptibilities. The points are the results obtained using a color group integration approach (see Chapter 4) at $V = (6.4 \text{ fm})^3$. For R_A , the lines are obtained from the Gaussian scaling formula in Eq. (4.57). For R_T , the lines are obtained from the mean-field calculations.

$T^3 \chi_T$. The R_A ratio cannot be obtained simply within a mean-field approach. One way to compute this observable is by setting up a color group integration, which was the main tool to investigate this observable in Chapter 4. Another, approximate way to determine R_A is to use the scaling relation discussed in Section 4.2.4. In this chapter we use the alternative scheme: instead of fitting the pure gauge potential, Eq. (4.54), we fit the full potential with the following Gaussian model,

$$U_1 = \alpha_1 (x - \ell_0)^2 + \alpha_2 y^2, \quad (5.18)$$

where ℓ_0 is the mean-field result for the Polyakov loop expectation value and

$$\alpha_1 = \frac{1}{2T^3 \chi_L} \quad (5.19)$$

$$\alpha_2 = \frac{1}{2T^3 \chi_T}$$

with χ_L and χ_T being the corresponding mean-field results for susceptibilities. The

	T_{χ_T} (GeV)	T_{χ_L} (GeV)	T_{S_Q} (GeV)	$T_{\text{inflex.}}$ (GeV)
$qB = 0$	0.26702	0.26737	0.26702	0.26737
$qB = 3m_0^2$	0.25544	0.26140	0.26140	0.26175
$qB = 6m_0^2$	0.24702	0.25579	0.25579	0.25614

Table 5.1: Characteristic temperatures extracted from the peak positions of various observables: χ_T , χ_L , S_Q and $\frac{\partial \ell}{\partial T}$.

scaling variable is constructed as

$$\begin{aligned}\xi &= \tilde{h} \times \frac{\sqrt{VT^3}}{2\sqrt{\alpha_1}}, \\ \tilde{h} &= \frac{\ell_0}{T^3 \chi_L}.\end{aligned}\tag{5.20}$$

When ξ and $R_T = \chi_L/\chi_T$ are substituted into Eq. (4.57), the Gaussian approximation of the R_A ratio can be obtained. Note, that $R_A(T, V)$ should be computed at a finite volume to be meaningful. Otherwise, $R_A \rightarrow 1$ as $V \rightarrow \infty$.

Numerical results on ratios of Polyakov loop susceptibilities are shown in Fig. 5.7. Lines correspond to the mean-field result for R_T and the Gaussian scaling formula for R_A . Points are the results obtained with the color group integration scheme at $V = (6.4 \text{ fm})^3$ (this volume is sufficiently large to reproduce the mean-field values of the Polyakov loop and the R_T ratio). Ratio observables behave as expected. The R_A ratio (the left panel) interpolates between two known limits, $2 - \pi/2$ at low temperatures and 1. The latter limit is reached more rapidly for larger breaking strength (i.e. for larger magnetic fields). We also find that the Gaussian scaling formula is robust unless very close to the phase transition, where the finite volume effects substantially smoothen this ratio observable. The R_T ratio is shown in the right panel of Fig. 5.7. As we already argued in the previous chapter, its low-temperature limit, 1, is dictated by the center symmetry, while the high-temperature behavior depends on the model used. Implementing the $SU(3)$ Haar measure in the effective gluon potential is crucial for obtaining $R_T \ll 1$ at large temperatures, which is also the trend suggested by LQCD studies. The R_T ratio is discontinuous at the first-order transition (the solid black line), becomes 0 at the critical point (the dashed red line), which follows from the divergent χ_L , and becomes smoothened in case of the crossover (the latter was already observed in Chapter 4). In all cases, the $R_T \approx 1$ at low temperatures. Note that the trend observed in the previous chapter, i.e. the ratio observables deviate from their center symmetric limits at lower temperatures for the increasing center symmetry breaking strength, can also be observed in these results.

5.3.2 Deconfinement phase diagram

To further analyze the impact of magnetic field on deconfinement, we calculate the transition temperature at different values of the magnetic field by tracking the peak of the longitudinal susceptibility. This is shown in Fig. 5.8 for a single flavor system with the quark mass $m_q/m_0 = 0.8, 1, 1.2$ and 1.4 . Solid lines correspond to the first-order transitions, and dots to critical points. We find that the deconfinement temperature in this model decreases with magnetic field for all quark masses. For heavier quarks, the magnetic field needed to reach the certain value of T_d is larger than that for lighter ones.

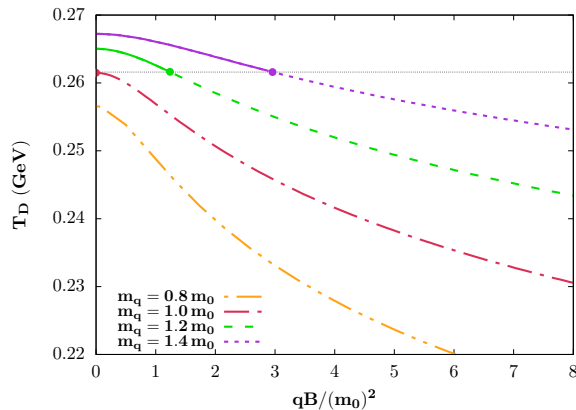


Figure 5.8: Deconfinement temperature in function of magnetic field for quark masses equal $0.84 m_0$ (orange double-dot-dashed line), m_0 (red dot-dashed line), $1.18 m_0$ (green dashed line), and $1.35 m_0$ (purple dotted line), where $m_0 = 1.1 \text{ GeV}$. Solid lines – 1st order phase transition, dots – deconfinement critical points. Thin dotted line - universal critical point temperature found in the linear approximation [187].

The second property can be easily understood by noticing that in this model, the impact of dynamical quarks on deconfinement is only through h and the deconfinement temperature decreases when h increases. Therefore, to reach the certain value of the breaking strength, lighter quarks need smaller magnetic field than heavier ones. This observation explains many features seen in Fig. 5.8.

We also note that for the class of models where the effect of dynamical quarks enters via the linear breaking term, the temperature corresponding to the deconfinement critical point is constant [187]. This can be understood following the argument from Ref. [187]: the critical point conditions for the potential of the form $U = U_G - hx$ read

$$\begin{aligned} \frac{\partial U_G}{\partial x} &= h, \\ \frac{\partial^2 U_G}{\partial x^2} &= 0, \\ \frac{\partial^3 U_G}{\partial x^3} &= 0. \end{aligned} \tag{5.21}$$

The first condition is the gap equation. At the critical point, the three extrema of the effective potential merge, which is reflected in the second and third conditions. Solutions of this set of equations determine values of the Polyakov loop, x_c , the temperature, T_{CEP} , and the breaking strength, h_c , at the critical point. If the gluon potential is independent of h , then the last two equations are sufficient to determine uniquely x_c and T_{CEP} . For the pure gluon potential used here, $T_{CEP} \approx 0.261 \text{ GeV}$, which can be observed in the current calculation.

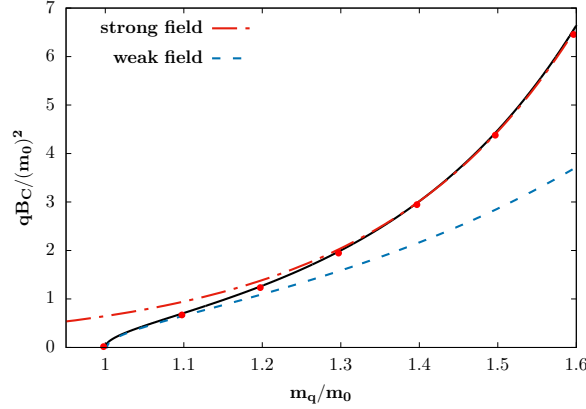


Figure 5.9: Critical magnetic field in function of the quark mass (black solid line) with its strong (red dotted line) and weak (blue dashed line) magnetic field approximations, where $m_0 = 1.1$ GeV.

The first equation of (5.21) fixes h_c which for the potential used in this study reads $h_c \approx 0.144$. This allows to determine the critical surface simply by solving the equation

$$\sum_f h_B^Q(m_f, q_f B, T) = h_c \quad (5.22)$$

To demonstrate the robustness of this condition, we first show the critical magnetic field needed to reach the deconfinement critical point for masses larger than m_0 in a single flavor system. This is shown in Fig. 5.9, where the solid black line is obtained from Eq. (5.22) and the red dots are obtained by tracking the divergent peak of χ_L . Both results agree, which confirms the validity of Eq. (5.22). The red dash-dotted line corresponds to the strong field limit which can be obtained from the LLL approximation (5.11),

$$eB_C(m) \approx \frac{\pi^2}{4} \frac{h_c (T_{CP})^3}{m K_1(m/T_{CP})}. \quad (5.23)$$

This approximation provides an accurate description of the full result for quark masses above $\sim 1.3m_0$. The blue dashed line corresponds to the weak field limit,

$$[eB_C(m)]^2 \approx \frac{h_c (T_{CP})^4 - \frac{18}{\pi^2} (m T_{CP})^2 K_2(m/T_{CP})}{\frac{1}{3\pi^2} K_0(m/T_{CP})}. \quad (5.24)$$

obtained by keeping only the quadratic correction in Eq. (5.10). This approximation is accurate up to $m_q \sim 1.1m_0$. For quark masses smaller than m_0 , deconfinement becomes a crossover, which is reflected by the fact that Eq. (5.22) has no real solutions.

As the another application of Eq. (5.22) we consider three flavor system where quark masses $m_u = m_d \equiv m_l$ and m_s are treated as independent variables. This allows to study

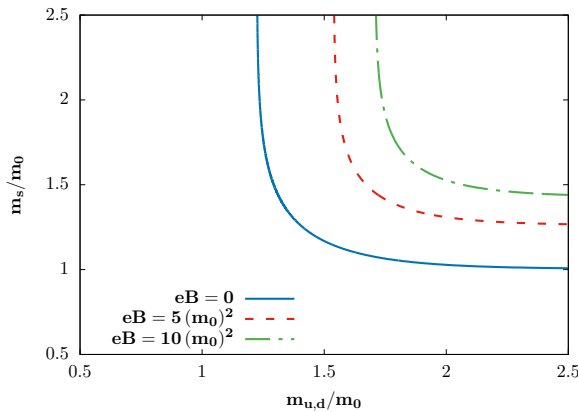


Figure 5.10: Lines of second order phase transitions in the (m_l, m_s) plane for $eB = 0$, $5(m_0)^2$ and $10(m_0)^2$ (blue solid, red dashed and green dot-dashed lines, respectively), where $m_0 = 1.1$ GeV.

the impact of a strong magnetic field on the critical surface in the (m_l, m_s) plane (i.e. the upper-right corner of the Columbia plot). Such a phase diagram was also studied using other effective models [189, 220] and using lattice methods. The LQCD determination of this graph (for the vanishing magnetic field) can be found in Refs. [221–223] (the continuum extrapolation, however, remains elusive). For a rough comparison to a recent work [223], the study reported $m_{PS}/T_{CEP} = (15.73; 11.15)$ for $N_\tau = (4; 6)$ in the two-flavor QCD system (NLO). In our case, for 2-flavor model, we take the pseudoscalar mass $m_{PS} \approx 2m_{crit.}$, with $m_{crit.} \approx 1.353$ GeV and $T_{CEP} \approx 0.261$ GeV, and find that the ratio m_{PS}/T_{CEP} is approximately 10.37. The matrix model [220] gives a comparable value of 11.8. This encourages a closer comparative study of effective models and LQCD calculations. The effect of external magnetic field on the phase diagram is shown in Fig. 5.10. The increasing magnetic field shrinks the region of first-order transition (the similar trend has been observed for the quark chemical potential [187]).

5.4 Studying the interplay between deconfinement and chiral dynamics

As the another application of the model considered in the previous section, we investigate the interplay between deconfinement and chiral dynamics. It is known that a naive implementation of the PNJL model leads to the deconfinement temperature that increases with magnetic field [24]. Such a feature of the PNJL model can be easily understood with the linear breaking strength. To this end, we consider the effective breaking strength $h[M(T, B), T, B]$ (similarly to Sec. 4.2.5 where we discussed the effective breaking strength of the PNJL model without the magnetic field) where $M(T, B)$ is

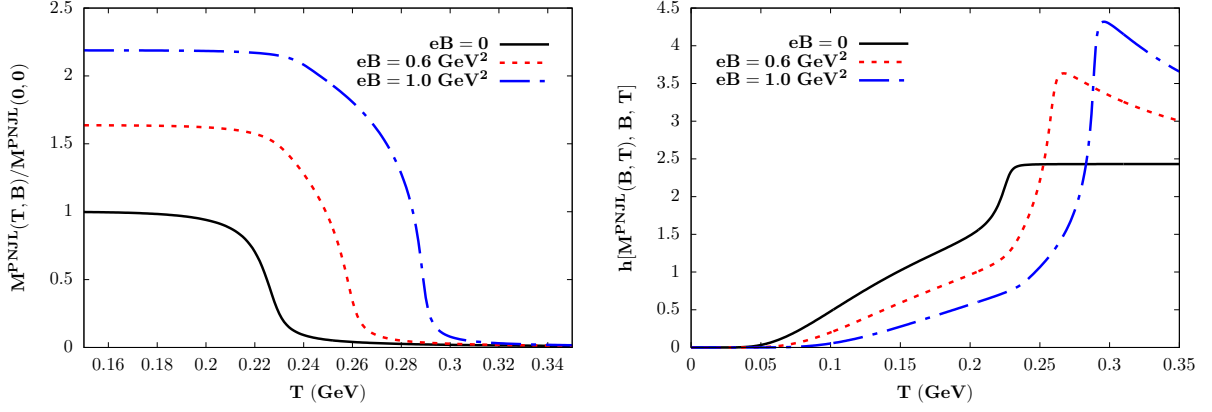


Figure 5.11: Temperature dependence of light quark masses normalized to the vacuum value (the left panel) and the corresponding effective breaking fields h (the right panel) obtained with the PNJL model. The solid black line: $eB = 0.0 \text{ GeV}^2$, dashed red line: $eB = 0.6 \text{ GeV}^2$, dash-dotted blue line: $eB = 1.0 \text{ GeV}^2$.

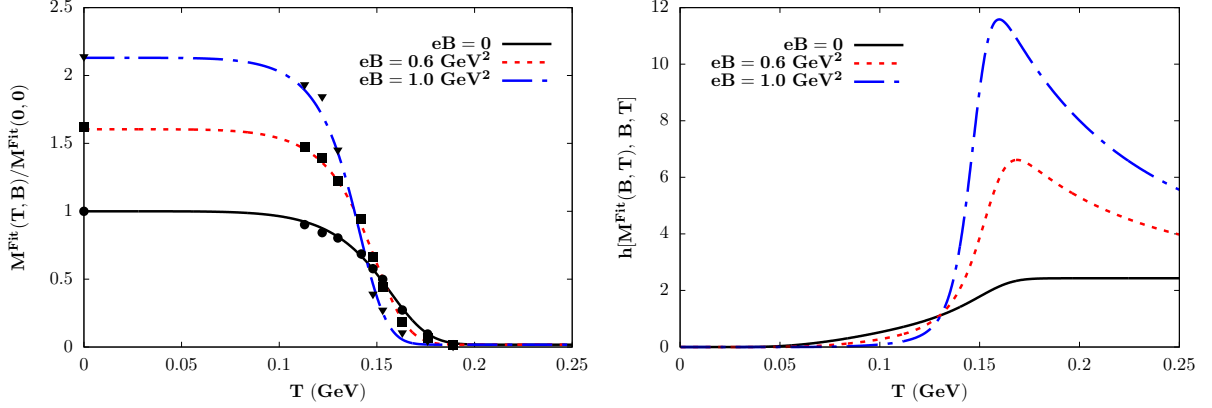


Figure 5.12: Temperature dependence of light quark masses normalized to the vacuum value (the left panel) and the corresponding effective breaking fields h (the right panel) obtained with the fit to LQCD data on quark condensate (based on Eq. (5.34), lattice data from [198]). The solid black line: $eB = 0.0 \text{ GeV}^2$, dashed red line: $eB = 0.6 \text{ GeV}^2$, dash-dotted blue line: $eB = 1.0 \text{ GeV}^2$.

the dressed quark mass obtained by solving the PNJL model gap equations. This brings up the additional, implicit B -dependence on top of the explicit B -dependence seen in Eq. (5.8).

Most of NJL models can capture the magnetic catalysis, i.e. the quark condensate obtained in the model increases with magnetic field at low temperatures. Since the explicit breaking strength (5.8) decreases with increasing quark mass, the enhancing effect of magnetic field may be weakened by the presence of the dressed quark mass. This may lead to increase of T_d in the PNJL model. To show this explicitly, we performed

a 2 flavor PNJL model calculation based on the NJL model from Ref. [224] with the degenerate quark masses. The corresponding effective potential reads

$$U_{PNJL}[\sigma, x, y] = U_{NJL}[\sigma] + U_B[\sigma] + U_G[x, y] + U_Q[\sigma, x, y], \quad (5.25)$$

where $\sigma \equiv \langle \bar{\psi}\psi \rangle$ (with $\psi = (u, d)^T$) is the light quark condensate,

$$T^4 U_{NJL}[\sigma] = G\sigma - 6 \times 2 \int_{|\vec{p}| < \Lambda} \frac{d^3 p}{(2\pi)^3} \sqrt{\vec{p}^2 + M^2} \quad (5.26)$$

is the NJL part,

$$T^4 U_B[M] = -\frac{3}{2\pi^2} \sum_{f=u,d} (q_f B)^2 \times \left(\zeta'(-1, x_f) - \frac{1}{2}(x_f^2 - x_f) \ln x_f + \frac{x_f^2}{4} \right) \quad (5.27)$$

is the $T = 0$ magnetic field contribution, where

$$x_f = \frac{M^2}{2|q_f B|} \quad (5.28)$$

and

$$\zeta'(-1, x) = \left. \frac{\partial}{\partial s} \zeta(s, x) \right|_{s=-1} \quad (5.29)$$

with $\zeta(s, x)$ the Hurwitz zeta function. $U_G[x, y]$ is the pure gluon potential (4.44) and the $U_Q[\sigma, x, y]$ the quark contribution given by Eq. (4.47) (with the sum over up and down flavors only). For finite B , the prescription (5.5) is used for U_Q . The constituent quark mass in this model is given by

$$M = m_0 - 2G\langle \bar{\psi}\psi \rangle, \quad (5.30)$$

where m_0 is the current quark mass. We tuned the model parameters such that the $T = 0$, $B \neq 0$ LQCD results of Ref. [198] are reproduced ($\Lambda = 515.07$ MeV, $G\Lambda^2 = 2.435$ and $m_0 = 6$ MeV which gives $\langle \bar{\psi}\psi \rangle = -2 \times (211 \text{ MeV})^3$). Expectation values are obtained by solving the gap equations

$$\frac{\partial U}{\partial \phi} = 0, \quad (5.31)$$

with $\phi \in \{\sigma, x, y\}$. The resulting constituent quark mass profiles are shown in the left panel of Fig. 5.11 and the corresponding effective breaking strength can be seen in the right panel. Indeed, as the magnetic field increases, the quark mass increases and its diminishing effect on h exceeds the enhancement due to explicit dependence on the magnetic field. Hence, h in the PNJL model decreases with the magnetic field in the

temperature ranges relevant for the phase transition. In the model described by Eq. (5.1) this leads to deconfinement temperature, which decreases with magnetic field. This is further confirmed in the fully self-consistent PNJL model calculation (see the black dashed line in Fig. 5.13).

We now explore, under the same mechanism, whether an improved quark mass function $M_Q(T, B)$ would lead to the correct trend of a decreasing T_d with B , as observed in LQCD calculations, e.g. Ref. [204]. To this end, we employ the following parametrization of $M_Q(T, B)$ inspired by the constituent quark mass form obtained in the NJL model (Eq. (5.30)),

$$M_Q(T, B) = m_0 - 2G \langle \bar{\psi}\psi \rangle_0 \mathcal{F}(T, B), \quad (5.32)$$

where $\langle \bar{\psi}\psi \rangle_0$ is the vacuum value of the quark condensate in the PNJL model and

$$\mathcal{F}(T, B) = \frac{\langle \bar{\psi}\psi \rangle^{\text{LQCD}}(T, B)}{\langle \bar{\psi}\psi \rangle_0^{\text{LQCD}}}. \quad (5.33)$$

is the ratio of chiral condensates obtained from LQCD. Using the lattice results of the $T = 0$ quark condensate [198] ($\mathcal{F}_0(B) \equiv \mathcal{F}(T = 0, B)$) and the chiral transition temperature at finite magnetic field ($T_\chi(B)$) [201], it was possible to construct a robust parametrization of the function $\mathcal{F}(T, B)$:

$$\begin{aligned} \mathcal{F}(T, B) &= \frac{\mathcal{F}_0(B)}{\mathcal{F}_1(T, B)} \\ \mathcal{F}_0(B) &= 1 + \frac{1}{2} \sum_{f=u,d} a_1 (\sqrt{1 + a_2 (q_f B)^2} - 1) \\ \mathcal{F}_1(T, B) &= \frac{\alpha(B) + e^{2(T/T_\chi(B))^6}}{1 + \alpha(B)}, \end{aligned} \quad (5.34)$$

with

$$\begin{aligned} a_1 &= 0.257 \\ a_2 &= 115.5 \\ \alpha(B) &= 2.47 + 4(eB)^2 \\ T_\chi(B) &= 0.159 - \frac{0.0326 (eB)^2}{1 + 0.4 (eB)^6}, \end{aligned} \quad (5.35)$$

where all quantities are in appropriate units of GeV. The parametrization is restricted to $eB \lesssim 1 \text{ GeV}^2$. When $T = 0$, $\mathcal{F}(T = 0, B) \rightarrow \mathcal{F}_0(B)$, which describes the rising of chiral condensate with magnetic field at $T = 0$.

The resulting quark mass profiles for $eB = 0$ (the solid black line), 0.6 GeV^2 (the red dashed line) and 1.0 GeV^2 (the blue dotted line) are shown in the left panel of Fig. 5.12 (the points correspond to quark mass formula (5.32) applied to LQCD data on the condensate [198]). Similarly to the PNJL model, the LQCD-improved quark mass increases

with the magnetic field at low temperatures. The key feature is that the improved quark mass drops faster with temperature with increasing B . In the right panel we show the corresponding effective breaking strength – in contrast to the PNJL model calculation (the right panel of Fig. 5.11), the breaking strength obtained with the improved quark mass profile strongly increases with the magnetic field in the temperature ranges relevant for the phase transition which suggest T_d that decreases with the magnetic field. This is confirmed by effective model calculation, shown in Fig. 5.13 (the black solid line).

Finally, we discuss the dependence of deconfinement temperature on the Polyakov loop potential. To this end, we performed an additional analysis using the polynomial parametrization of Polyakov loop potential introduced in Ref. [155]. The corresponding results are shown as red lines in Fig. 5.13. In case of the full PNJL model (the red dashed line) the deconfinement temperature rises stronger with the magnetic field than in case of the potential given by Eq. (4.44). In case of the improved quark mass function, the deconfinement temperature decreases slowly up $eB \lesssim 0.5 \text{ GeV}^2$ and rises for stronger fields. This clearly demonstrates the merit of using an improved Polyakov loop potential, where the locations and the curvatures around minima are properly adjusted.

With the general argument via $h[M(T, B), B, T]$, we have demonstrated the delicate interplay between chiral dynamics (for the correct $M_Q(T, B)$) and deconfinement. This could help in constraining the missing interactions in effective chiral models. We also note that if the full one-loop fermion potential would be used to study the deconfinement temperature instead of its linear approximation, the enhancing effect of the improved quark mass profile on the center symmetry breaking would be reduced, countering the effect of the improved quark mass profile. This is the another hint that the one-loop fermion potential provides insufficient enhancement of the center symmetry breaking, and further modifications should be pursued to capture these effects correctly. In the next section, we show how the dressing of the four-fermion interaction leads to the correct trend of the deconfinement temperature and inverse magnetic catalysis.

5.5 Driving the inverse magnetic catalysis with the ring diagram

5.5.1 Chiral quark model with dressed interaction

As we already discussed, qualitative predictions on the magnetic field dependence of deconfinement and chiral crossover temperatures at finite B , obtained with PNJL-type models in general do not agree with the trend observed in LQCD which suggests missing interactions between quarks and gluons in the model. One of possibility to improve the situation is to consider in-medium effects which could account for the "sea" quark contribution.

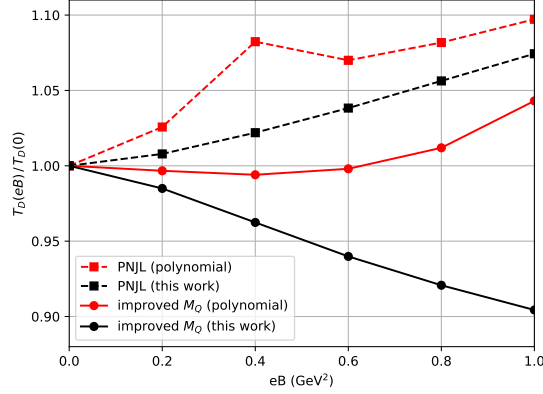


Figure 5.13: Deconfinement temperature in function of magnetic field (normalized to the value at $B = 0$ in the corresponding model). Dashed lines and squares – the full PNJL model calculation with the pure gauge potential (4.44) (black) and the polynomial potential [155] (red). Solid lines and dots – effective model (5.1) calculation with the LQCD-improved quark mass profile (Eq. (5.32)) for the potential (4.44) (black) and the polynomial potential [155] (red). The difference in quark mass functions implies essential differences in the $Z(3)$ breaking strength $h_B^Q[M_Q(T, B), T, B]$, which consequently result in the opposite trends in T_d dependence on B .

In this section, we discuss the in-medium dressing of the four-quark coupling by the polarization diagram within an effective chiral quark model, following Refs. [79, 80]. Screening of the potential by the ring diagram finds the most famous application in regulating the long-range Coulomb forces in an electron gas [225, 226]. When applied to the study of the QCD phase diagram, we shall show that it provides a natural mechanism of reducing the chiral transition temperature in a class of models, and is capable of generating an inverse magnetic catalysis at finite temperature.

Our starting point is an effective chiral quark model motivated by the Coulomb Gauge QCD [227–234]. The Lagrangian density reads

$$\mathcal{L}(x) = \bar{\psi}(x) (i\cancel{\partial}_x - m) \psi(x) - \frac{1}{2} \int d^4y \rho^a(x) V^{ab}(x, y) \rho^b(y), \quad (5.36)$$

where m is the current quark mass, $\rho^a(x) = \bar{\psi}(x) \gamma^0 t^a \psi(x)$ is the color quark current, and t^a is a generator of the $SU(N_c)$ symmetry group, with $a = 1, 2, \dots, N_c^2 - 1$.

Details of the model depend on the interaction potential V , through which the gluon dynamics is incorporated. For the class of models, where the potential is instantaneous and color-diagonal, i.e. has the following form,

$$V^{ab}(x, y) \rightarrow \delta^{ab} \times \delta(x^0 - y^0) V(\vec{x} - \vec{y}), \quad (5.37)$$

the following gap equation for the dynamical quarks has been derived [234],

$$S^{-1}(p) = \not{p} - m - \Sigma(p) \quad (5.38)$$

where

$$\Sigma(p) = C_F \int \frac{d^4 q}{(2\pi)^4} V(\vec{p} - \vec{q}) i \gamma^0 S(q) \gamma^0. \quad (5.39)$$

The constant $C_F = \frac{N_c^2 - 1}{2N_c}$ is introduced via the quadratic Casimir operator,

$$\sum_{a=1}^{N_c^2 - 1} t^a t^a = C_F I_{N_c \times N_c} \quad (5.40)$$

The gap equation (5.38) has to be solved self-consistently, since the self energy (5.39) depends on the dressed quark propagator $S(q)$. The outcome of the gap equation depends on the details of the interaction potential. A particularly transparent case is a contact interaction, where we replace

$$V(\vec{p} - \vec{q}) \rightarrow V_0. \quad (5.41)$$

In this case, the solution to the gap equation (5.38) becomes

$$\begin{aligned} M &= m + \text{Tr}(\Sigma) / \text{Tr}(I) \\ &= m + C_F V_0 \int \frac{d^3 q}{(2\pi)^3} \frac{M}{2E} \times (1 - 2 N_{\text{th}}(E)), \end{aligned} \quad (5.42)$$

where $E = \sqrt{\vec{q}^2 + M^2}$ and $N_{\text{th}}(E) = (e^{\beta E} + 1)^{-1}$ is the Fermi-Dirac distribution, with temperature $T = 1/\beta$. Equation (5.42) is of the same form as the familiar result for the quark mass in the NJL model [50] and the gap equations, to leading-order, would agree if we identify

$$C_F V_0 \leftrightarrow 4 N_c N_f (2 G_{\text{NJL}}). \quad (5.43)$$

Despite the equivalence of the gap equations, the present model in fact provides a more natural starting point as an effective model of QCD. It closely mimics the quark-gluon interactions of QCD by implementing a vector nature of the four-quark interactions originated from a gluon exchange, both in the color and the Dirac space. This allows us to formally identify V_0 with the longitudinal gluon propagator and select the relevant Dirac structure of the polarization tensor when dressing the potential. Moreover, it gives the opportunity to systematically improve the quark potential by considering features of gluon propagators, e.g. momentum dependence. We note that an effective interaction in the scalar-scalar channel, which gives rise to the spontaneous chiral symmetry breaking, can be generated from a vector-vector interaction which may be understood by considering a Fierz transformation [18] of the original Lagrangian in Eq. (5.36).

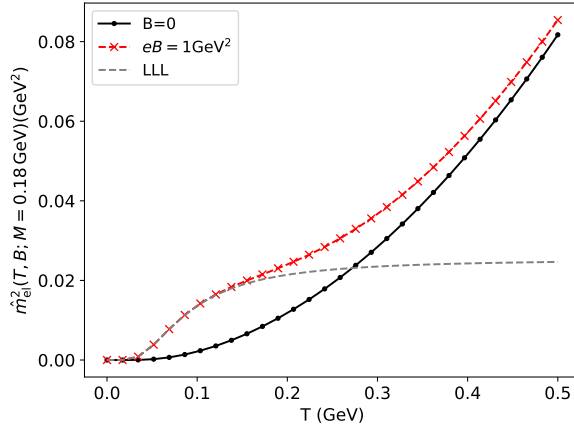


Figure 5.14: The electric mass squared (Eq. (5.46)) for the 2-flavor case at fixed quark mass $M = 0.18$ GeV, as a function of temperature. The results in a finite magnetic field are calculated using Eq. (5.49) with physical electric charges of (u, d) quarks.

Following Ref. [234], we implement the in-medium dressing of the interaction potential V_0 by the polarization tensor Π_{00} via

$$\tilde{V}_0^{-1} = V_0^{-1} - \frac{1}{2} N_f \Pi_{00} \quad (5.44)$$

where the polarization is further approximated by the ring diagram

$$\Pi_{00}(p^0, \vec{p}) = \frac{1}{\beta} \not{\sum} \text{Tr} (\gamma^0 S(q) \gamma^0 S(q + p)). \quad (5.45)$$

Here $\not{\sum}$ denotes the Matsubara sum over the fermionic frequencies ($\omega_n = (2n + 1) \pi / \beta$), and an integral over the momenta d^3q . Equation (5.44) describes the screening of the gluon propagator by the Debye mass. The factor of $\frac{1}{2}$ in Eq. (5.44) comes from the color structure, i.e. $\text{Tr} T^a T^b = \frac{1}{2} \delta^{ab}$, and is essential to reproduce the known result [129] of the perturbative Debye mass for QCD, rather than for QED.

In many studies, polarization tensors are computed with the fermion propagator determined from a leading order mean-field gap equation such as Eq. (5.42). The use of \tilde{V}_0 , in place of V_0 , results in implementing a back-reaction of the fermion loops to the fermionic gap equation. In the language of condensed matter theory, the scheme is similar to an iteration of the GW-scheme [235, 236] with polarization insertions but without vertex corrections. This effectively dresses the four-quark interaction and can substantially modify aspects of chiral phase transition, such as driving the phenomenon of inverse magnetic catalysis.

Here, we consider only the screening by the static, finite temperature part of Π_{00} (the

static, vacuum part of Π_{00} naturally vanishes) which can be related to the electric mass,

$$\begin{aligned}\hat{m}_{el}^2 &= -\frac{1}{2} N_f \Pi_{00}(p^0 = 0, \vec{p} \rightarrow \vec{0}) \\ &= \frac{1}{2} N_f \times \int \frac{d^3q}{(2\pi)^3} 4\beta N_{\text{th}}(1 - N_{\text{th}}).\end{aligned}\tag{5.46}$$

At $M \rightarrow 0$ (or large T) this formula approaches the known result (we note that in perturbative setting the electric mass is multiplied by coupling g),

$$\hat{m}_{el}^2 \approx \frac{1}{2} N_f \times \frac{T^2}{3}, \quad M/T \ll 1.\tag{5.47}$$

At large M (or small T), where the Boltzmann approximation is valid, the electric mass squared is

$$\hat{m}_{el}^2 \approx \frac{1}{2} N_f \times \frac{2}{\pi^2} M^2 (K_2(M/T) - K_2(2M/T)),\tag{5.48}$$

where K_2 is the modified Bessel function of the second kind. In Fig. 5.14 (the solid black line and dots) we demonstrate a numerical calculation of the electric mass (5.46) at the fixed value of $M = 0.18$ GeV (a typical value near the transition), and $N_f = 2$ flavors. The analytic limits in Eqs. (5.47) and (5.48) can be readily verified.

Formulas for the electric mass shown above can be easily extended to finite magnetic field, following prescription (5.5). Thus, the electric mass (per flavor) for $B \neq 0$ is

$$\hat{m}_{el}^2 = \frac{1}{2} \frac{|e_f|B}{2\pi} \sum_{n=0}^{\infty} \frac{1}{2} \alpha_n \times \int \frac{dq_z}{2\pi} 4\beta N_{\text{th}}(E_{q_z,n})(1 - N_{\text{th}}(E_{q_z,n})),\tag{5.49}$$

where $\alpha_n = 2 - \delta_{n,0}$. Examining in particular the contribution from the lowest Landau level (LLL), we get, per flavor,

$$\hat{m}_{el}^2 \approx \frac{1}{2} \frac{|e_f|B}{4\pi} \int \frac{dq_z}{2\pi} \frac{4\beta e^{\beta\sqrt{q_z^2+M^2}}}{(e^{\beta\sqrt{q_z^2+M^2}} + 1)^2}.\tag{5.50}$$

The result of an example calculation is shown as the red dashed line in Fig. 5.14. The dashed line corresponds to LLL, which is realized at low temperatures. At large temperatures, the electric mass slowly approaches $B = 0$ result.

5.5.2 Gap equations

A standard NJL model lacks a description of confinement. This is usually remedied by considering an additional coupling of quarks to the Polyakov loop. One known issue of PNJL-type models is that they overestimate the chiral transition temperature: typically

giving $T_{ch} \approx 220 \text{ MeV}$ instead of the LQCD result $T_{ch} \approx 158.0 \text{ MeV}$ [164]. A common way to deal with this problem is by an ad hoc rescaling of the T_d parameter entering the effective Polyakov loop potential: from the physical value of $T_d = 270 \text{ MeV}$, to a lower value at $T_d \approx 200 \text{ MeV}$ [212, 213, 237]. This is far from ideal, as it points to some missing interactions in the original model. Moreover, the problem appears again if one sends the quark mass to infinity, which results in incorrect temperature, unless one introduces yet another adjustment with the quark mass. Here, we propose the screening of the interaction by polarization as a natural resolution to the problem. For this purpose, we generalize the model (5.36) to include the coupling to ℓ by implementing a statistical confinement scheme, i.e., by replacing the thermal weight $N_{\text{th}}(E)$ in Eq. (5.42) with ($N_c = 3$) [238–240]

$$\begin{aligned} N_{\text{th}}(E, \ell) &\rightarrow \frac{1}{3} \sum_{j=1}^3 \frac{\hat{\ell}_F^{(j)}}{e^{\beta E} + \hat{\ell}_F^{(j)}} \\ &= \frac{1}{3} \frac{3\ell e^{-\beta E} + 6\ell e^{-2\beta E} + 3e^{-3\beta E}}{1 + 3\ell e^{-\beta E} + 3\ell e^{-2\beta E} + e^{-3\beta E}}, \end{aligned} \quad (5.51)$$

where $\hat{\ell}_F^{(j)}$ are entries of the Polyakov loop operator in the fundamental representation

$$\hat{\ell}_F = \text{diag} (e^{i\gamma_1}, 1, e^{-i\gamma_1}), \quad (5.52)$$

related to the Polyakov loop ℓ via

$$\ell = \frac{1}{3} \text{Tr} \hat{\ell}_F = \frac{1}{3} (1 + 2 \cos \gamma_1). \quad (5.53)$$

Furthermore, we couple the electric mass to the Polyakov loop by performing the following replacement,

$$N_{\text{th}}(1 - N_{\text{th}}) \rightarrow \frac{1}{3} \sum_{j=1}^3 \frac{\hat{\ell}_F^{(j)} e^{\beta E}}{e^{\beta E} + \hat{\ell}_F^{(j)}}. \quad (5.54)$$

Our final set of gap equations is

$$\begin{aligned} M &= m + C_F \tilde{V}_0 M \times I_0(T; M, \ell), \\ \tilde{V}_0(T; M, \ell) &= \frac{1}{V_0^{-1} + \hat{m}_{el}^2(T; M, \ell)}, \\ \frac{\partial}{\partial \ell} (U_G(\ell) + U_Q(M, \ell)) &= 0. \end{aligned} \quad (5.55)$$

The integral entering the first equation consists of the vacuum part, $T = 0$ magnetic field contribution and thermal part,

$$I_0 = I_0^{\text{vac}} + I_0^B + I_0^T, \quad (5.56)$$

where the first piece diverges and hence requires regularization. Here, we choose $4D$ regulator,

$$I_0^{\text{vac}}(M) = \int \frac{d^4 q_E}{(2\pi)^4} \frac{1}{q_E^2 + E^2} \mathcal{R}_{4D}(q_E), \quad (5.57)$$

where $q_E^2 = (q_4)^2 + (\vec{q})^2$ is the Euclidean 4-momentum,

$$\mathcal{R}_{4D}(q) = e^{-|q|^8/\Lambda^8} \quad (5.58)$$

and the set of model parameters is given by: $\Lambda = 1.076 \text{ GeV}$, $G_{\text{NJL}} \Lambda^2 = 4.232$, and a current quark mass $m = 5 \text{ MeV}$. In the vacuum, these parameters give: $f_\pi = 92.9 \text{ MeV}$, $m_\pi = 137.8 \text{ MeV}$, and $\langle \bar{\psi}\psi \rangle = -(250 \text{ MeV})^3$ (per flavor). The vacuum value of the constituent quark mass is $M_0 \approx 240 \text{ MeV}$. To match the current model with the NJL model, we use the prescription (5.43).

On the other hand, the magnetic field and thermal contributions do not require regularization. The former, per flavor reads [224],

$$I_{0,f}^B(M, q_f B) = \frac{M^2}{16\pi^2} \times \left[\frac{\ln \Gamma(x_f)}{x_f} - \frac{\ln(2\pi)}{2x_f} + 1 - \left(1 - \frac{1}{2x_f}\right) \ln x_f \right] \quad (5.59)$$

where x_f is defined in Eq. (5.28) and $\Gamma(x)$ is the gamma function. This contribution vanishes as $B \rightarrow 0$. At the vanishing magnetic field, the thermal contribution is

$$I_0^T(M, \ell, T) = - \int \frac{d^3 q}{(2\pi)^3} \frac{1}{2E} \times 2N_{\text{th}}(E, \ell). \quad (5.60)$$

For a finite B , this contribution is obtained using the prescription (5.5) and reads (per flavor)

$$I_0^T(M, \ell, T, q_f B) = - \frac{|q_f| B}{2\pi} \sum_{n=0}^{\infty} \frac{1}{2} \alpha_n \int \frac{dq_z}{2\pi} \frac{1}{2E_{q_z, n}} \times 2N_{\text{th}}(E_{q_z, n}, \ell). \quad (5.61)$$

The screening of V_0 in Eq. (5.55) introduces further field dependence in M and ℓ . In fact, \tilde{V}_0 may be considered as an effective in-medium coupling. We note that, depending on the model parameters and regularization scheme chosen, screening can induce a first order phase transition instead of a crossover [234, 241]. In the current model, this effect was observed for the $4D$ regulator [79] which we use in this section and, following this reference, we consider a further approximation of $\tilde{V}_0(T; M, \ell) \approx \tilde{V}_0(T; \langle M \rangle, \ell)$, and fix $\langle M \rangle = 0.136 \text{ GeV}$. In the last gap equation, which describes the gluon sector, we choose Eq. (5.1).

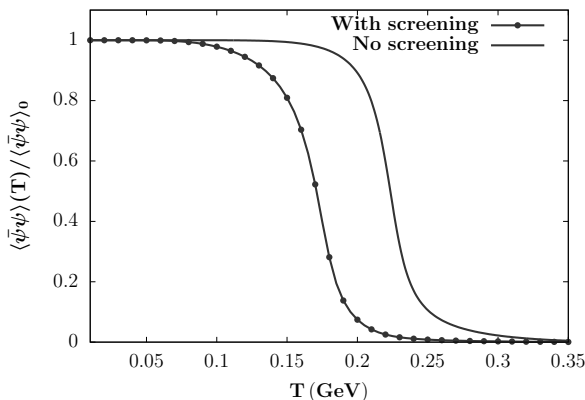


Figure 5.15: The chiral condensate (normalized to the vacuum value) at the vanishing magnetic field. The model with screening (the line with dots) shows a substantial reduction of critical temperature, compared to the PNJL model without screening (the line without dots).

5.5.3 Numerical results

We first consider the effect of screening without the magnetic field. Solving gap equations (5.55) consistently, we obtain the results in Fig. 5.15. The screening of the effective four-quark coupling by the electric mass leads to a substantial drop in the chiral transition temperature from $T_{ch} \approx 230$ MeV in the PNJL model (the plain line) to $T_{ch} \approx 175$ MeV (the line with dots).

To examine the effect of screening at finite magnetic field, we performed a numerical study of the chiral condensate and Polyakov loop. The first quantity is shown in the left panel of Fig. 5.16 (where the black solid line and dots correspond to $B = 0$, the red dashed line and triangles to $B = 0.6$ GeV² and the blue dash-dotted line and squares to $B = 1.0$ GeV²). Without the polarization screening in Eq. (5.44), our model is equivalent to PNJL type of model and hence it predicts an increasing chiral transition temperature with B (shown by lines without symbols), evident from the fact that the condensate remains large for a wider range of temperatures. When the interaction is dressed, the ring weakens the effective four-quark coupling at finite temperatures, and its effect is strong enough to reverse the trend observed in the PNJL-like models (shown by solid lines with symbols). We note that at $T = 0$, results are the same for the model with and without screening which can be understood from the fact, that the electric mass vanishes at $T = 0$.

The screening affects not only the chiral transition, but also the deconfinement, which can be seen from the behavior of Polyakov loop (the right panel of Fig. 5.16). Without screening, the overall magnetic field dependence of the Polyakov loop is weak. Its expectation value shifts slightly towards higher temperatures (see the solid, dashed and

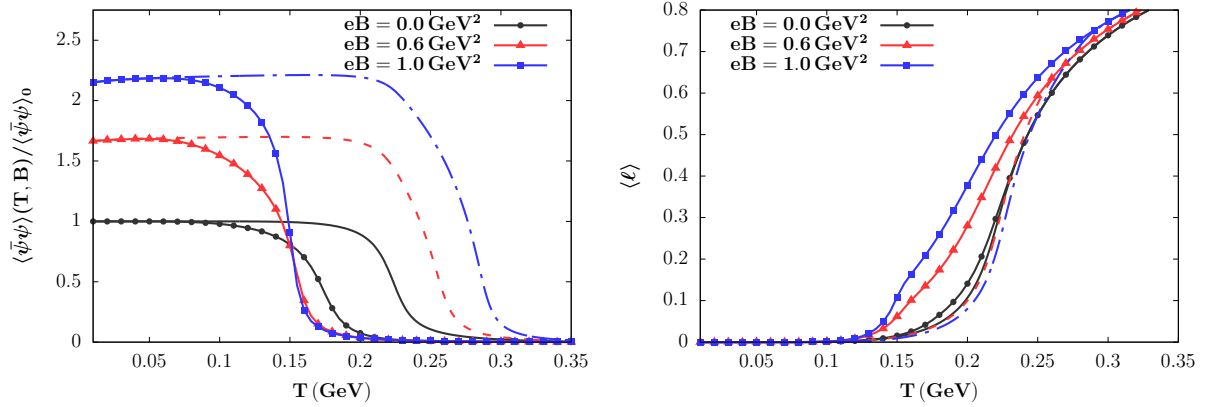


Figure 5.16: The chiral condensate (normalized to the vacuum value) (left), and the Polyakov loop (right), versus the temperature, at different magnetic fields $eB = 0$ (black solid line and dots), 0.6 GeV^2 (red dashed line and triangles) and 1.0 GeV^2 (blue dot-dashed line and squares). Lines with symbols (dots, triangles and squares) represent results obtained from a PNJL model with the dressed coupling, while the ones without symbols correspond to results of PNJL model without screening. The model with dressed coupling is capable of producing the inverse magnetic catalysis at finite temperatures.

dot-dashed lines) which indicates that the deconfinement temperature in the PNJL model increases with B . This feature of the PNJL-like models was already discussed in Sec. 5.4 for a different model setting. Although the parameters of the current model are different, the corresponding breaking field $h[M^{PNJL}(T, B), T, B]$ shows qualitatively the same behavior as seen in Fig. 5.11 (see Fig. 5.17 for the dressed quark mass and effective breaking field in the current model). When we consider the model with screening, we can find that ℓ is strongly affected by magnetic field, and it shifts towards lower temperatures, which clearly indicates that deconfinement temperature decreases with B . When we consider the effective breaking strength $h[M^{RING}(T, B), T, B]$ (see Fig. 5.18, where the left panel shows the dressed quark mass $M^{RING}(T, B)$ and the right panel contains the corresponding effective breaking field), we see that it strongly rises with magnetic field, showing the similar behavior to the one observed in Fig. 5.12. The important difference is that in the current model, the center symmetry breaking strength is enhanced by the in-medium dressing of the four-quark coupling (instead of the mass function (5.32) obtained by fitting the lattice data). This, in turn, weakens the confining effect and results in the enhancement of the polarization, which further reduces the four-quark coupling. The model considered here demonstrates such a positive feedback mechanism in a very transparent manner.

The effective NJL coupling $G(T, B)$ normalized to the vacuum value G_{NJL} , obtained in the current model, is shown in Fig. 5.19. The screening reduces the coupling even at the vanishing magnetic field. For finite B , the reduction of the coupling become substantial. The dressing of the interaction by the ring diagram may be seen as incorporation of the

5.6. Simultaneous effect of finite chemical potential and magnetic field on deconfinement

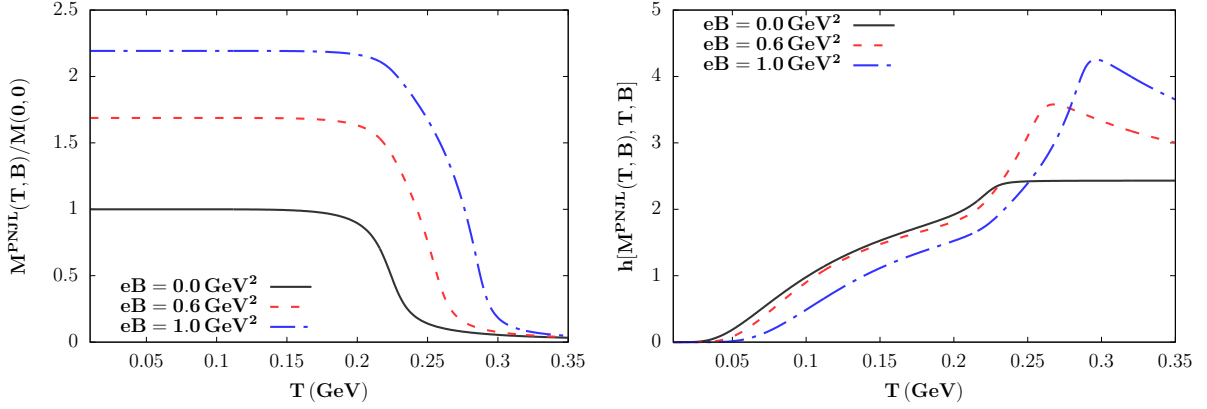


Figure 5.17: Temperature dependence of light quark masses normalized to the vacuum value (the left panel) and the corresponding effective breaking fields h (the right panel) obtained with the model (5.36) without dressed interaction.

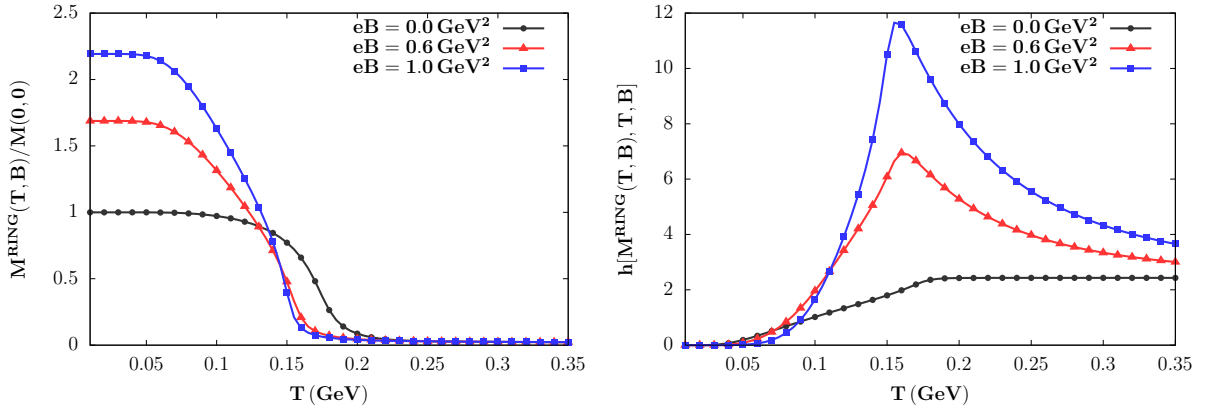


Figure 5.18: The same as in Fig. 5.17 but with interactions dressed with the ring diagram.

”sea quark” effect in this model. We also note that the need for a B -dependent coupling has been motivated in Refs. [237, 242] and Eq. (5.44) could be a theoretical justification to introducing such an effect.

5.6 Simultaneous effect of finite chemical potential and magnetic field on deconfinement

5.6.1 Sign problem and the Polyakov loop

Because of the sign problem, LQCD calculations at $\mu \neq 0$ are greatly limited and investigation of the QCD phase diagram at finite μ is one of the important applications of

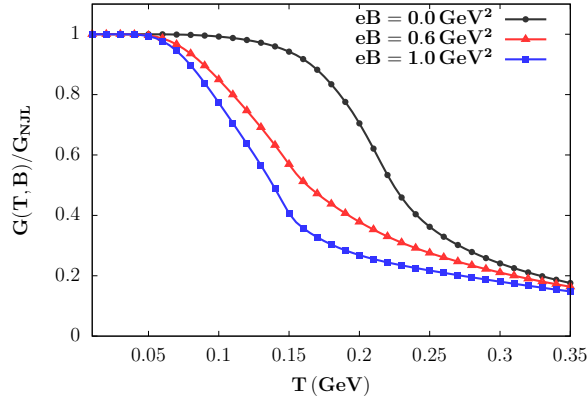


Figure 5.19: The effective coupling strength obtained in the model with screening, normalized to its vacuum value G_{NJL} .

effective models. In the final part of this chapter, we study how deconfinement is influenced by both magnetic field and quark chemical potential, working again in the heavy quark approximation [81].

In the presence of finite chemical potential, expectation values of Polyakov loop and its conjugate are real but, in general, different. This, at first confusing fact, may be understood by careful investigation of the QCD partition function [154, 158, 243]. We show this following Ref. [154]. The functional integration over fermion fields in the partition function (3.25) can be performed, which introduces the fermion determinant. At $\mu \neq 0$ it can be written as (for simplicity, we consider single quark flavor)

$$\mathcal{M}(A, \mu) = \det(i\mathcal{D} - i\gamma_4^E \mu - m), \quad (5.62)$$

where Euclidean Dirac matrices are chosen to be anti-Hermitian, $\gamma_4^E = i\gamma^0$, $\gamma_k^E = \gamma^k$ such that $\{\gamma_\mu^E, \gamma_\nu^E\} = -2\delta_{\mu\nu}$ [133]. In this convention, the covariant derivative part, $i\mathcal{D}$, is anti-Hermitian and hence it has purely imaginary eigenvalues, $\pm i\lambda$. On the other hand, $i\gamma_4^E \mu$ is Hermitian and hence eigenvalues of the mixed operator $i\mathcal{D} - i\gamma_4^E \mu$ will be complex. The fermion determinant can be split into real and imaginary parts,

$$\mathcal{M}(A, \mu) = \text{Re } \mathcal{M}(A, \mu) + i\text{Im } \mathcal{M}(A, \mu), \quad (5.63)$$

and one can prove that under the charge conjugation $A_\mu^C = -A_\mu$ these components transform as

$$\begin{aligned} \text{Re } \mathcal{M}(A^C, \mu) &= \text{Re } \mathcal{M}(A, \mu) \\ \text{Im } \mathcal{M}(A^C, \mu) &= -\text{Im } \mathcal{M}(A, \mu). \end{aligned} \quad (5.64)$$

In the functional integral, one sums over all configurations of the gluon fields. Therefore, for a given A_μ there will be the corresponding contribution from A_μ^C and hence the

imaginary part of the determinant does not contribute to the partition function,

$$Z_{QCD} = \int_{\text{periodic}} \mathcal{D}[A] \text{Re}\mathcal{M}(A, \mu) e^{-S_{YM}[A]}. \quad (5.65)$$

Following the same argument, one can show that expectation of value of a C -even observable, $O_+(A^C) = O_+(A)$, is

$$\langle O_+ \rangle = \frac{1}{Z_{QCD}} \int_{\text{periodic}} \mathcal{D}[A] O_+(A) \text{Re}\mathcal{M}(A, \mu) e^{-S_{YM}[A]}. \quad (5.66)$$

and the expectation value of a C -odd observable, $O_-(A^C) = -O_-(A)$, is

$$\langle O_- \rangle = \frac{1}{Z_{QCD}} \int_{\text{periodic}} \mathcal{D}[A] O_-(A) \text{Im}\mathcal{M}(A, \mu) e^{-S_{YM}[A]}. \quad (5.67)$$

Although in all cases integrands are manifestly real, they may be no longer strictly positive which justifies the name "sign problem".

Especially for the Polyakov loop, one finds that

$$\langle x \pm iy \rangle = \frac{1}{Z_{QCD}} \int_{\text{periodic}} \mathcal{D}[A] (x(A) \text{Re}\mathcal{M}(A, \mu) \mp y(A) \text{Im}\mathcal{M}(A, \mu)) e^{-S_{YM}[A]}, \quad (5.68)$$

which explains why expectation values of the ℓ and $\bar{\ell}$ are different for $\mu \neq 0$. Difference between these expectation values can also be understood physically. We remind that Polyakov loop is related to the free energy of a static quark,

$$\langle \ell \rangle = e^{-F_q/T}, \quad (5.69)$$

and the expectation value of its conjugate may be related to the free energy of a static anti-quark [59, 137],

$$\langle \bar{\ell} \rangle = e^{-F_{\bar{q}}/T}. \quad (5.70)$$

At finite baryon density, the energy required to put the quark into the medium will be different from the corresponding energy for the anti-quark and thus the Polyakov loop and its conjugate will be different too.

5.6.2 Modeling Polyakov loop fluctuations at finite chemical potential

To model deconfinement at finite B and μ , we consider the model of the form (5.1). Without the external magnetic field and chemical potential, the one-loop fermion contribution is given by Eq. (4.47). When the $\mu \neq 0$, this function becomes modified and for

a single quark flavor it reads

$$U_Q = -\frac{2}{T^3} \int \frac{d^3p}{(2\pi)^3} (\ln g^+ + \ln g^-) , \quad (5.71)$$

where coefficients g^\pm are now μ -dependent [158],

$$g^+ = 1 + 3\ell e^{-\beta(E-\mu)} + 3\bar{\ell} e^{-2\beta(E-\mu)} + e^{-3\beta(E-\mu)} , \quad (5.72)$$

$$g^- = 1 + 3\bar{\ell} e^{-\beta(E+\mu)} + 3\ell e^{-2\beta(E+\mu)} + e^{-3\beta(E+\mu)} , \quad (5.73)$$

with $E^2 = \vec{p}^2 + m^2$, where m is the quark mass. In fact, the sign problem is present even at the level of effective models [20, 154]. ℓ and $\bar{\ell}$ entering Eq. (5.73) are complex. When $\mu = 0$, g^+ and g^- are complex conjugates and the effective potential remains real. However, when the chemical potential is not zero, this property no longer holds and the effective potential is complex. At the mean-field level, one replaces ℓ and $\bar{\ell}$ with their expectation values, which are allowed to be different. Although in this case, the effective potential is real, it has a saddle point and solutions of the gap equations are not stable in the $\bar{\ell} - \ell$ direction, which can be seen as a remnant of the sign problem in model calculations [20, 154].

As previously, the coupling to the magnetic field is obtained following the prescription (5.5). Thus, the quark contribution at finite magnetic and chemical potential field reads

$$U_Q(\ell, \bar{\ell}, T, \mu, qB) = -\frac{|qB|}{2\pi T^3} \sum_{\sigma=\pm 1} \sum_{k=0}^{\infty} \int_{-\infty}^{\infty} \frac{dp_z}{2\pi} (\ln g_f^+ + \ln g_f^-) , \quad (5.74)$$

where coefficients g^\pm are given by Eq. (5.73) with the quark dispersion relation (5.4).

To calculate expectation values of the order parameters as well as their fluctuations, we perform the mean-field approximation. The Polyakov loop and its conjugate are obtained by solving the following gap equations,

$$\begin{aligned} \frac{\partial U}{\partial \ell} &= 0 \\ \frac{\partial U}{\partial \bar{\ell}} &= 0. \end{aligned} \quad (5.75)$$

The corresponding susceptibilities are obtained from the inverse of the curvature matrix,

$$T^3 \chi = \mathcal{C}^{-1} , \quad (5.76)$$

where

$$\mathcal{C} = \begin{pmatrix} \frac{\partial^2 U}{\partial \ell^2} & \frac{\partial^2 U}{\partial \ell \partial \bar{\ell}} \\ \frac{\partial^2 U}{\partial \ell \partial \bar{\ell}} & \frac{\partial^2 U}{\partial \bar{\ell}^2} \end{pmatrix} , \quad (5.77)$$

5.6. *Simultaneous effect of finite chemical potential and magnetic field on deconfinement*

which is evaluated at $(\ell_0, \bar{\ell}_0)$ obtained by solving the gap equations (5.75). Note that in this basis, the off-diagonal terms do not vanish. To calculate the longitudinal and transverse susceptibilities we use the following relations [158, 187],

$$\chi_L = \frac{1}{2}\chi_{\ell\bar{\ell}} + \frac{1}{4}(\chi_{\ell\ell} + \chi_{\bar{\ell}\bar{\ell}}), \quad (5.78)$$

$$\chi_T = \frac{1}{2}\chi_{\ell\bar{\ell}} - \frac{1}{4}(\chi_{\ell\ell} + \chi_{\bar{\ell}\bar{\ell}}). \quad (5.79)$$

where the susceptibilities $\chi_{\ell\ell}$, $\chi_{\ell\bar{\ell}}$ and $\chi_{\bar{\ell}\bar{\ell}}$ are obtained from Eq. (5.76). This allows to calculate the R_T ratio in the presence of the finite chemical potential.

Before studying the simultaneous effect of magnetic field and chemical potential on deconfinement, we discuss the effect of μ on Polyakov loop and its susceptibilities at the vanishing magnetic field. In the calculation we set the quark mass to be $1.4m_0 = 1.54$ GeV. Since the mass is above the critical value, the deconfinement for $\mu = 0$ is first-order, which could be already seen in Figs. 5.4-5.7. The upper left panel of Fig. 5.20 shows the expectation value of Polyakov loop (thick colored lines) and its conjugate (thin gray lines). For $\mu = 0.5$ GeV the deconfinement transition becomes continuous (dashed lines) and turns into a crossover for larger μ (the dash-dotted lines). Therefore, finite chemical potential, similarly to magnetic field, increases the strength of the explicit center symmetry breaking (this was already found in Ref. [187]). One can also see explicitly that Polyakov loop and its conjugate are not the same for $\mu \neq 0$.

The lower left panel shows the simultaneous effect of finite chemical potential and magnetic field. Here, we fix $\mu = 0.25$ GeV and vary the magnetic field, $qB = 0, 2.25$ and 5 GeV² (the solid, dashed and dash-dotted lines). In this case, the critical value of the magnetic field is lower than in the case of $\mu = 0$. This is because both quantities enhance the strength of $Z(3)$ symmetry breaking, and their effects add up to the total breaking strength.

The corresponding susceptibilities can be seen in Fig. 5.21, where the left column shows the longitudinal susceptibility and the right column to the transverse susceptibility, calculated from equations (5.78) and (5.79), respectively. The qualitative behavior of the longitudinal susceptibility is the same as in $\mu = 0$ case – it is discontinuous at the first-order transition, diverges at the deconfinement critical point and has a finite peak in the crossover region. (The discontinuities are difficult to see due to the choice of the figure scale.) The transverse susceptibility is discontinuous for the first-order transition as well, and does not diverge at the critical point. However, in contrast to $\mu = 0$ case, for the finite chemical potential, $T^3\chi_T$ develops a cusp. Hence, in this case, this observable becomes sensitive to the critical point.

The R_T ratio is shown in Figure 5.22, where the left panel corresponds to the fixed $qB = 0$ and varying chemical potential and the right panel shows the simultaneous contribution of finite chemical potential and magnetic field with fixed $\mu = 0.25$ GeV and varying

magnetic field. In both cases, the R_T ratio is sensitive to the deconfinement and further confirms that quark chemical potential increases the explicit center symmetry breaking strength.

Since at finite chemical potential free energies of static quark and antiquark are different, one can study not only the static quark entropy (5.16), but also the static anti-quark entropy,

$$S_{\bar{Q}} = \frac{\partial F_{\bar{Q}}}{\partial T} = \frac{\partial}{\partial T} T \ln \langle \bar{\ell} \rangle. \quad (5.80)$$

In the right column of Figure 5.20, we present the static quark (thick colored lines) and anti-quark entropies (thin gray lines) corresponding to the Polyakov loop expectation values shown in the left column. When the chemical potential vanishes, both entropies are equal because $\ell = \bar{\ell}$. Finite chemical potential leads to splitting between S_Q and $S_{\bar{Q}}$ which can be seen for both upper right and lower right panels. This follows from the fact that expectation values of the Polyakov loop and its conjugate are different for $\mu \neq 0$. In the first-order region and at the critical point, both entropies indicate the same phase transition temperature. In case of the crossover, the peaks are slightly shifted and the maximum of the static quark entropy is at a lower temperature than the maximum of the static anti-quark entropy.

5.6. Simultaneous effect of finite chemical potential and magnetic field on deconfinement

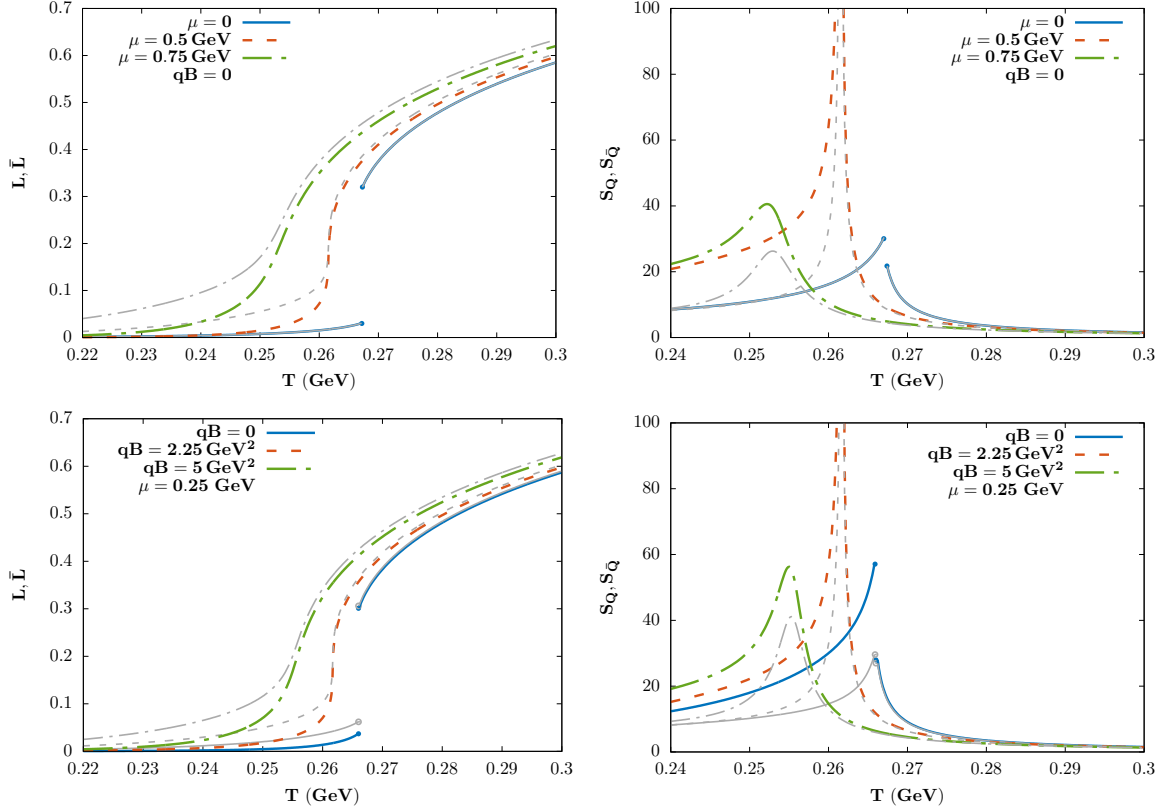


Figure 5.20: Left column: Polyakov loop expectation value (thick colored lines) and its conjugate (thin gray lines) calculated for various values of the magnetic field and chemical potential. Right column: The corresponding static quark (thick colored lines) and anti-quark (thin gray lines) entropies. For all figures, the quark mass is $1.4m_0 = 1.54$ GeV.

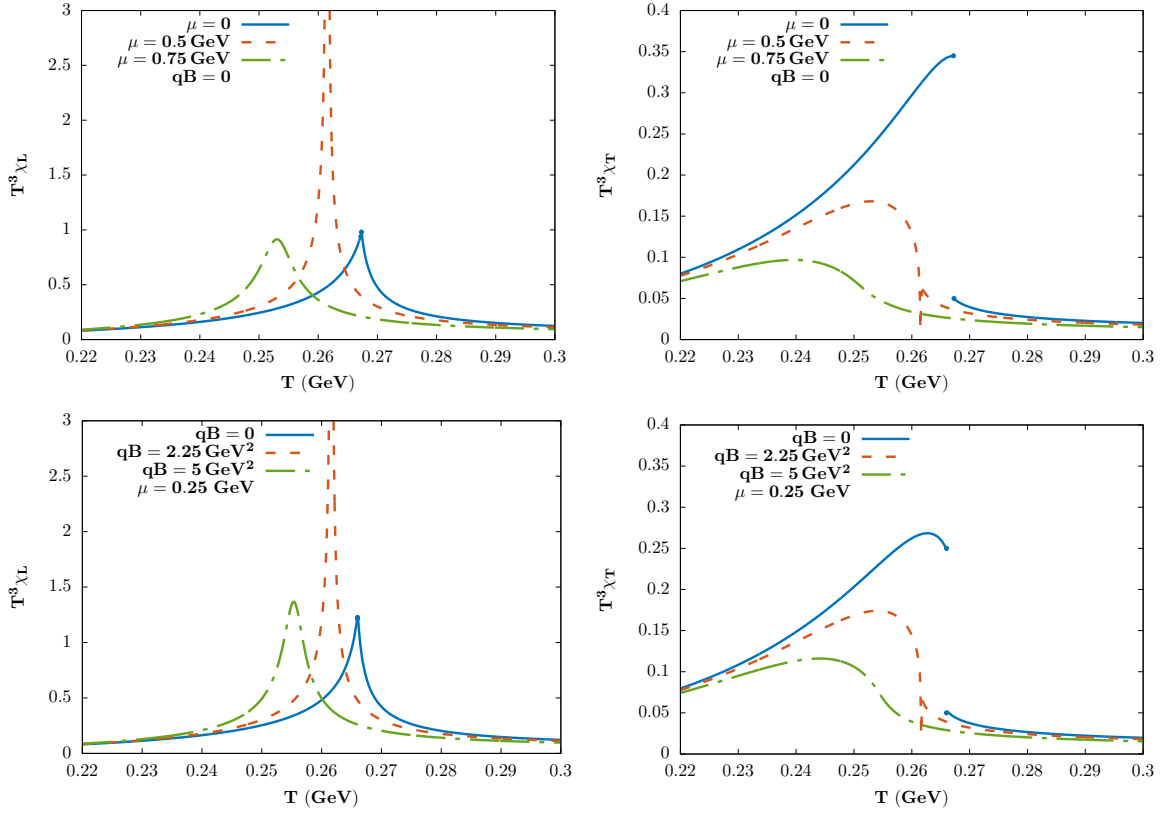


Figure 5.21: Left column: The longitudinal susceptibility of the Polyakov loop, calculated for various values of the magnetic field and chemical potential. Right column: The corresponding transverse susceptibilities. For all figures, the quark mass is $1.4m_0 = 1.54$ GeV.

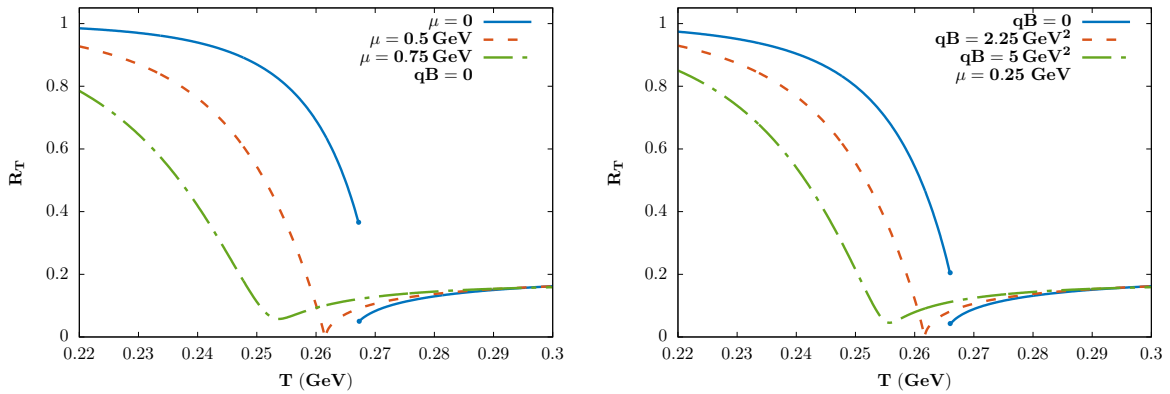


Figure 5.22: The R_T ratio calculated for different values of chemical potential and external magnetic field. For all figures, the quark mass is $1.4m_0 = 1.54$ GeV.

Chapter 6

Net-proton number fluctuations in the presence of the QCD critical point

In this chapter, we study the behavior of the net-proton number cumulants in the presence of the QCD critical point. We first give an overview on the fluctuations of conserved charges and their role in searches of the QCD critical point. Then, we discuss results on net-proton number cumulants obtained in Ref. [82] using a phenomenological model in which the fluctuations of the chiral critical mode were coupled to protons and anti-protons. Especially, we study the dependence of our results on the model parameters and the proximity of the chemical freeze-out to the critical point.

6.1 Fluctuations of conserved charges

Searching for the critical point in the QCD phase diagram is one of the important aspects of relativistic heavy-ion experiments. In contrast to measurements of, for example, magnetization in magnetic systems, the order parameter of chiral phase transition is not directly measurable in heavy-ion collisions and hence different quantities have to be considered to search for the QCD critical point [60]. An important class of observables which are expected to be sensitive to the critical point are fluctuations of conserved charges [60, 68].

For QCD, various conserved charges can be defined (see Chapter 2). In the context of searching for the critical point, natural candidates are the baryon number (B), electric charge (Q) and strangeness (S), and their fluctuations can be quantified in terms of generalized susceptibilities. They can be obtained by taking derivatives of the pressure

with respect to the corresponding chemical potentials [61],

$$\chi_{ijk}^{BQS} = \frac{\partial^{i+j+k}(P(T, \mu_B, \mu_Q, \mu_S)/T^4)}{\partial(\mu_B/T)^i \partial(\mu_Q/T)^j \partial(\mu_S/T)^k}. \quad (6.1)$$

Susceptibilities are related to the cumulants of conserved charges by

$$C_{ijk}^{BQS} = VT^3 \chi_{ijk}^{BQS}. \quad (6.2)$$

Especially, in this section we consider cumulants of the baryon number (therefore, we will omit superscript B in the following),

$$C_i = \frac{\partial^i(P(T, \mu_B)/T^4)}{\partial(\mu_B/T)^i}. \quad (6.3)$$

Cumulants provide information about the distribution function of the particle number and can be expressed in terms of its moments[68]. In particular, the first four cumulants of the baryon number N_B read [61]

$$\begin{aligned} C_1 &= VT^3 \chi_1 = \langle N_B \rangle, \\ C_2 &= VT^3 \chi_2 = \langle \Delta N_B \rangle, \quad \Delta N_B = N_B - \langle N_B \rangle, \\ C_3 &= VT^3 \chi_3 = \langle (\Delta N_B)^3 \rangle, \\ C_4 &= VT^3 \chi_4 = \langle (\Delta N_B)^4 \rangle_c \equiv \langle (\Delta N_B)^4 \rangle - 3\langle (\Delta N_B)^2 \rangle^2. \end{aligned} \quad (6.4)$$

Note that susceptibilities are intensive quantities, while cumulants are extensive. Therefore, it is useful to consider their ratios in which, ignoring volume fluctuations, the volume dependence cancels out. Consequently [68],

$$\frac{C_2}{C_1} = \frac{\sigma^2}{M}, \quad \frac{C_3}{C_2} = S\sigma, \quad \frac{C_4}{C_2} = \kappa\sigma^2, \quad (6.5)$$

where $M = C_1$ is the mean, $\sigma^2 = C_2$ the variance, $\kappa = C_4/(C_2)^2$ the kurtosis, and $S = C_3/(C_2)^{3/2}$ the skewness. Under the assumption that experimentally measured event-by-event multiplicity fluctuations originate from a thermal source with the given temperature and chemical potentials, one can compare theoretical results for the cumulant ratios with the experimental data to deduce features of the QCD phase diagram.

There are several reasons why the fluctuations of conserved charges are useful for investigating properties of QCD medium. First, they can be used to obtain the information about the effective degrees of freedom in the system in thermal equilibrium [16, 244]. As an example, we discuss the ratio χ_4/χ_2 of baryon number cumulants. At temperatures smaller or equal, approximately, 180 MeV, the QCD pressure is well-approximated by the hadron resonance gas (HRG) model [16] in which the pressure of the interacting hadron gas is approximated by the sum of the partial pressures of non-interacting hadrons and their resonances [245, 246]. In this model, one obtains $\chi_4/\chi_2 = 1$. On the other hand,

at large temperatures, the QCD medium is composed of approximately free quarks and gluons and in this case, one expects $\chi_4/\chi_2 \approx 1/9$ (the actual result is slightly smaller because of the quantum corrections). These predictions are supported by LQCD calculations which show that at $T \lesssim T_c$, χ_4/χ_2 is close to 1 (the value obtained from the HRG) and decreases rapidly above the transition temperature [247, 248], thus indicating the change in effective degrees of freedom in the QCD medium during crossover. Similar considerations can also be made for cumulants of electric charge and strangeness, as well as for mixed correlations, which allows to explore various characteristics of confined and deconfined matter [68, 244].

The another important feature of cumulants of conserved charges is sensitivity to the critical fluctuations. The chiral CP belongs to the $Z(2)$ static universality class of the 3-dimensional Ising model and the critical mode (σ) can be associated with the order parameter, the chiral condensate [49, 72, 73, 249]. At the critical point, fluctuations of the order parameter diverge. Although the condensate is not measurable, the critical behavior can also be observed for quantities which couple to σ and its fluctuations, including fluctuations of conserved charges [68, 244]. Moreover, the sensitivity to critical fluctuations increases with the order of cumulants [61, 68, 250]. The last feature is particularly useful for investigating the medium created during the heavy-ion collisions, in which the correlation length is limited by the finite size of the system and the phenomenon of critical slowing down [251, 252]. This makes higher-order cumulants of conserved charges important quantities for searches of the QCD critical point.

To compare theoretical predictions with the experimental data, the cumulants are calculated on the chemical freeze-out line. The anticipated effect of the critical point is the non-monotonic behavior of higher-order cumulants along the freeze-out line [60]. Experimentally, the fluctuations are measured on the event-by-event basis, i.e. for each event (collision) the particle multiplicities are measured and the event-by-event distribution function is obtained. The latter may be used to infer cumulants of conserved charges. Usually, detectors are not sensitive to neutral particles and thus the net-baryon and net-strangeness numbers are not directly measurable [68]. The net-proton number and net kaon-number are often used as proxies for net-baryon and net-strangeness, respectively [68].

Measurements of event-by-event fluctuations in the net-proton number [253–256], the net-electric charge [257] and the net-kaon number [258], have been performed in heavy-ion collisions at RHIC and LHC energies. The non-monotonic structures observed in the preliminary STAR Collaboration data on higher-order net-proton number fluctuations were indeed observed [254–256], however their unambiguous interpretation as the consequence of the presence of the CP has not been achieved yet [69, 70, 259, 260]. There are several factors which obscure the interpretation of the experimental data. The medium created in a heavy-ion collision is neither static nor infinite and due to its expansion dynamics, the non-equilibrium effects can play an important role and may, for example, lead to the retardation and damping of the critical signals [261–264]. Furthermore, even

in thermodynamic equilibrium, the global charge conservation [265–267], volume fluctuations [266, 268, 269], and further sources of non-critical fluctuations in the data [270], as well as, late hadronic stage processes [271–275], can modify signals of the critical fluctuations. These challenges make it clear that the theoretical description and interpretation of the data on fluctuation observables require special care and eventually a dynamical framework to match the conditions expected in heavy-ion collisions. Nevertheless, numerical simulations of the critical dynamics also require input from static, equilibrium models to provide an analytic benchmark [264, 269, 276, 277].

An additional complication arises from the fact that the relevant quark masses (m_u and m_d) are small but not 0. In the limit of vanishing m_q , the chiral transition is expected to be a second-order phase transition for small and even zero μ_B , belonging to the $O(4)$ static universality class. This line of second-order phase transitions terminates in a tricritical point at sufficiently large baryon chemical potential [278]. Recent lattice QCD studies [279, 280] and measurements of higher-order cumulants of net-particle multiplicity distributions [281] have revealed a significant impact of the hidden $O(4)$ criticality at larger \sqrt{s} even in case of the explicit chiral symmetry breaking. Moreover, in [278] it was shown that for reasonable light quark masses the physics near CP is strongly affected by the presence of the tricritical point. In fact, only very close to CP, for distances smaller than 1.5 MeV in μ_B , criticality in line with $Z(2)$ has been observed. Outside, in a wider region around CP, traces of the hidden tricritical point become visible as a difference in the scaling behavior of chiral and net-baryon number susceptibilities. From a phenomenological point of view it is, therefore, reasonable to attempt an implementation of the overlap of the two static universality classes relevant for the QCD phase transition, $O(4)$ and $Z(2)$.

The goal of this chapter is to investigate ratios of the net-proton number cumulants (as a proxy of net-baryon number cumulants) along the chemical freeze-out line obtained in the heavy-ion collisions (the results were originally published in Ref. [82]). We study implications of the tricritical point in an equilibrium model and identify systematics of the net-proton number cumulant ratios for different locations of the CP in the (T, μ_B) -plane, relative to the freeze-out line.

As a starting point, we choose the phenomenological model formulated in Ref. [275], which accounts for the critical fluctuations in heavy-ion collisions. In that work, the fluctuations of the critical mode were linked to protons, anti-protons and resonances by allowing the particle masses to fluctuate as a consequence of the (partial) mass generation through the coupling to σ . As was demonstrated there, the non-monotonicity observed in the higher-order fluctuation data of STAR Collaboration [254–256] can be qualitatively described within such formulation. However, in contrast to the experimental data, a pronounced peak structure was also found in the lowest-order cumulant ratios of the net-proton fluctuations even for small values of couplings [275]. We re-examined the assumptions of that model to improve the discrepancies between the model predictions and the STAR data on the variance of net-proton number fluctuations obtained in heavy-ion collisions.

The general idea was based on the universality of the critical scaling behavior of the net-quark (net-baryon) number susceptibility [278] near CP that is influenced by the tricritical point. The consistent implementation of critical scaling leads to a much weaker singularity than that seen for the net-proton number variance in Ref. [275]. In the mean field approximation of the chiral effective models, the singular part of the net-quark number susceptibility is proportional to the chiral susceptibility multiplied by the order parameter squared [282, 283]. This is correct both for O(4) and the tricritical point. In line with these findings, the model introduced in Ref. [275] was improved to further consistently identify the influence of criticality due to the existence of the CP on the net-proton number fluctuations in such a way that the impact of the O(4) criticality is taken into account. In the following, we will quantify different cumulant ratios of these fluctuations along the chemical freeze-out line obtained in heavy-ion collisions. We will also identify systematics of the net-proton number cumulant ratios for different locations of the CP in the (T, μ_B) -plane, relative to the freeze-out line.

6.2 Modeling critical fluctuations in heavy-ion collisions

In the following section, we describe the theoretical tools to be used to quantify the net-proton number fluctuations in the presence of the QCD critical point. We first define the baseline model, which does not contain contributions from fluctuations of the chiral critical mode. Then we explain, how the critical fluctuations can be coupled to particles near the CP. The approach is motivated by the observation that the critical contribution to the variance of the net-proton number should obey a certain scaling behavior [282, 283]. On the mean-field level, this idea can be extended to higher-order fluctuations. The critical mode fluctuations are obtained by using universality class arguments between QCD and the 3-dimensional Ising model.

6.2.1 Baseline model

As a baseline model for calculating the net-proton number cumulants, we employ the HRG model in which the particle density of each particle species is given by the ideal gas expression

$$n_i(T, \mu_i) = d_i \int \frac{d^3k}{(2\pi)^3} f_i^0(T, \mu_i), \quad (6.6)$$

where d_i is the degeneracy factor and

$$f_i^0 = \frac{1}{(-1)^{B_i+1} + e^{(E_i - \mu_i)/T}} \quad (6.7)$$

is the thermal equilibrium distribution function. In Eq. (6.7), $E_i = \sqrt{k^2 + m_i^2}$ is the energy and $\mu_i = B_i\mu_B + S_i\mu_S + Q_i\mu_Q$ the chemical potential of a particle with mass m_i , baryon number B_i , strangeness S_i and electric charge Q_i . μ_X 's are the chemical potentials conjugate to the conserved charge numbers N_X . For a grand canonical ensemble, the average particle number in a constant volume V is $\langle N_i \rangle = Vn_i$.

In the thermal medium, the particle number fluctuates around its mean on an event-by-event basis. These fluctuations can be quantified in terms of cumulants, where the n th order cumulant of i th particle specie is defined, similarly to Eq. (6.3), as

$$C_n^i = VT^3 \left. \frac{\partial^{n-1}(n_i/T^3)}{\partial(\mu_i/T)^{n-1}} \right|_T, \quad (6.8)$$

at constant temperature, T . In the following, we consider the first four cumulants of the net-proton number $N_{p-\bar{p}} = N_p - N_{\bar{p}}$, which are given by

$$C_1 = \langle N_{p-\bar{p}} \rangle = \langle N_p \rangle - \langle N_{\bar{p}} \rangle, \quad (6.9)$$

$$C_2 = \langle (\Delta N_{p-\bar{p}})^2 \rangle = C_2^p + C_2^{\bar{p}}, \quad (6.10)$$

$$C_3 = \langle (\Delta N_{p-\bar{p}})^3 \rangle = C_3^p - C_3^{\bar{p}}, \quad (6.11)$$

$$C_4 = \langle (\Delta N_{p-\bar{p}})^4 \rangle_c = C_4^p + C_4^{\bar{p}}, \quad (6.12)$$

where

$$\Delta N_{p-\bar{p}} = N_{p-\bar{p}} - \langle N_{p-\bar{p}} \rangle, \quad (6.13)$$

and

$$\langle (\Delta N_{p-\bar{p}})^4 \rangle_c = \langle (\Delta N_{p-\bar{p}})^4 \rangle - 3\langle (\Delta N_{p-\bar{p}})^2 \rangle^2. \quad (6.14)$$

The second equalities in Eqs. (6.10)-(6.12) hold only when correlations between different particle species vanish, which is the case in the HRG model. In the following, we ignore the contributions which arise from resonance decays and concentrate solely on the primary proton and anti-proton numbers as well as their fluctuations. Under the assumption that experimentally measured event-by-event multiplicity fluctuations originate from a thermal source with given T and μ_B , μ_Q and μ_S , one can compare the model results for the cumulant ratios with the experimental data to deduce features of the QCD phase diagram.

6.2.2 Coupling to critical mode fluctuations

Fluctuations of the chiral critical mode, σ , near the QCD critical point are expected to affect various experimentally measurable quantities, including the net-proton number cumulants [64, 65, 284]. Currently, there is no general prescription of how to model the effect of critical fluctuations on observables. In Ref. [275], inspired by the way in which the particle mass is generated near the chiral transition in the sigma models, the critical

mode fluctuations were incorporated into the HRG model by allowing the particle mass to fluctuate on an event-by-event basis around its mean value. Consequently, this leads to fluctuations in the distribution function, $f_i = f_i^0 + \delta f_i$. The change of the distribution function due to critical mode fluctuations reads

$$\delta f_i = \frac{\partial f_i}{\partial m_i} \delta m_i = -\frac{g_i v_i^2}{T \gamma_i} \delta \sigma, \quad (6.15)$$

where g_i is the coupling strength between σ and the particle of type i (which, in principle, can also depend on T and μ_X), $v_i^2 = f_i^0((-1)^{B_i} f_i^0 + 1)$ and $\gamma_i = E_i/m_i$.

Due to the above modification of the distribution function, proton and anti-proton number fluctuations are no longer independent. Considering only the most singular contributions to the fluctuations (see Ref. [285] for a discussion of the impact of less critical contributions), one obtains the following expressions for the net-proton number cumulants influenced by the conjectured critical point,

$$C_2 = C_2^p + C_2^{\bar{p}} + \langle (V\delta\sigma)^2 \rangle (I_p - I_{\bar{p}})^2, \quad (6.16)$$

$$C_3 = C_3^p - C_3^{\bar{p}} - \langle (V\delta\sigma)^3 \rangle (I_p - I_{\bar{p}})^3 \quad (6.17)$$

and

$$C_4 = C_4^p + C_4^{\bar{p}} + \langle (V\delta\sigma)^4 \rangle_c (I_p - I_{\bar{p}})^4, \quad (6.18)$$

where

$$I_i = \frac{g_i d_i}{T} \int \frac{d^3k}{(2\pi)^3} \frac{v_i^2}{\gamma_i} \quad (6.19)$$

and $\langle (V\delta\sigma)^n \rangle_c$ are the critical mode cumulants.

To calculate the cumulants of the critical mode, we apply universality class arguments. Assuming that the QCD critical point belongs to the same universality class as the 3-dimensional Ising model, we identify the order parameter in QCD, σ , with the magnetization M_I , i.e. the order parameter of the Ising spin model. The critical mode cumulants are defined as

$$\langle (V\delta\sigma)^n \rangle_c = \left(\frac{T}{VH_0} \right)^{n-1} \left. \frac{\partial^{n-1} M_I}{\partial h^{n-1}} \right|_r, \quad (6.20)$$

where $r = (T - T_c)/T_c$ and $h = H/H_0$ are the reduced temperature and magnetic field in the spin model, respectively, and the critical point is located at $r = h = 0$.

In our approach, the second cumulant C_2 of the net-proton number receives critical contributions through the coupling of (anti-)protons to the critical mode via the first derivative of the magnetization $\partial M_I / \partial h$. In the spin model, this quantity is the magnetic susceptibility, and, because of the universality, it can be related to the chiral susceptibility (χ) in QCD. For the $Z(2)$ universality class, the chiral susceptibility is known to diverge with a stronger amplitude but the same critical exponent as the net-baryon number susceptibility χ_B . This is, however, correct only extremely close to the CP [278]. Further

away, in a larger region around CP, traces of the hidden tricritical point lead to different critical exponents, making the magnetic susceptibility to diverge stronger than the baryon number one [278, 282, 283]. Therefore, the model in its form introduced in Ref. [275] requires some modifications. In Ref. [82] they were accomplished by using the following chiral relation between the net-baryon number and the chiral susceptibilities, which was found in the effective model calculations [282, 283] for the $O(4)$ universality class and the tricritical point,

$$\chi_B \simeq \chi_B^{\text{reg}} + \sigma^2 \chi. \quad (6.21)$$

Here χ_B^{reg} is the regular part of the net-baryon number susceptibility, whereas the second term in the above equation constitutes the singular part, χ_B^{sing} . Although this relation holds on the mean-field level, we will still use it in the present model to capture the correct dominant scaling behavior near, but not exactly at, the QCD critical end point.

Following Eq. (6.16), the singular part of the second-order cumulant is written as

$$C_2^{\text{sing}} = \langle (V\delta\sigma)^2 \rangle m_p^2 (J_p - J_{\bar{p}})^2, \quad (6.22)$$

where

$$J_i = \frac{g_i d_i}{T} \int \frac{d^3 k}{(2\pi)^3} \frac{v_i^2}{E_i}. \quad (6.23)$$

In the linear-sigma models, the proton mass is related to the chiral condensate. By replacing the factor m_p in Eq. (6.22) by $g_p \sigma$, the critical contribution to the second-order cumulant in Eq. (6.16) has the same form as the one in Eq. (6.21). We note that this replacement is only done at leading-order in the derivation, i.e. factors of E_i remain unaffected. This phenomenological approach results in the following modification,

$$\gamma_i \rightarrow E_i / (g_i \sigma), \quad (6.24)$$

which is applied also to the higher-order cumulants of the net-proton number. Consequently, we arrive at

$$C_2 = C_2^p + C_2^{\bar{p}} + g_p^2 \sigma^2 \langle (V\delta\sigma)^2 \rangle (J_p - J_{\bar{p}})^2, \quad (6.25)$$

$$C_3 = C_3^p - C_3^{\bar{p}} - g_p^3 \sigma^3 \langle (V\delta\sigma)^3 \rangle (J_p - J_{\bar{p}})^3 \quad (6.26)$$

and

$$C_4 = C_4^p + C_4^{\bar{p}} + g_p^4 \sigma^4 \langle (V\delta\sigma)^4 \rangle_c (J_p - J_{\bar{p}})^4. \quad (6.27)$$

By evaluating σ and its cumulants, we aim at capturing the crossover between the $O(4)$ and $Z(2)$ universality classes near the CP. As a result, C_2 now scales as $R^{\beta(3-\delta)}$ instead of $R^{\beta(1-\delta)}$ with the distance R from the CP in the region that is dominated by the influence of the tricritical point. It should only approach the scaling $\propto R^{\beta(1-\delta)}$ extremely close to the critical end point. Nonetheless, we note that we will never consider a situation in which we are substantially close enough to see the pure $Z(2)$ criticality. In QCD with finite quark masses, the proper order parameter of $Z(2)$ is a linear combination

of scalar density, quark number density and energy density. Along this direction, the grand potential exhibits zero curvature at the $Z(2)$ CP [286]. The soft mode emerges as a space-like collective excitation in the scalar spectral function [287]. A massive σ -mode appears in the time-like sector and decouples from the critical fluctuations near the CP. Thus, the σ in Eq. (6.21) must be interpreted as an effective soft mode for the overlap between the $O(4)$ and $Z(2)$ criticalities even in the presence of finite quark masses. In the following, we use g instead of g_p and apply Eqs. (6.9) and (6.25)-(6.27) together with Eq. (6.23) to calculate the net-proton number cumulant ratios.

6.2.3 Magnetic equation of state

To calculate σ and its cumulants, we use the parametric representation of the magnetic equation of state [288],

$$M_I = M_0 R^\beta \theta, \quad (6.28)$$

which is, strictly speaking, valid only in the scaling region close to the critical point. Here R and θ are auxiliary variables which depend on r and h , from which R measures the distance from the critical point. They are determined by solving the following equations,

$$r = R(1 - \theta^2), \quad (6.29)$$

$$h = R^{\beta\delta} w(\theta), \quad (6.30)$$

where β and δ are critical exponents and

$$w(\theta) = c\theta(1 + a\theta^2 + b\theta^4) \quad (6.31)$$

is an odd polynomial in θ . The parameters entering Eqs. (6.28)-(6.31) can be determined numerically by the Monte-Carlo simulations or by other theoretical tools such as the ϵ -expansion or functional renormalization group methods. In [288], renormalization group and field theoretical methods were used to determine the critical exponents and coefficients of $w(\theta)$, reading, $\beta = 0.325$ and $\delta = 4.8169$, and $a = -0.76145$, $b = 0.00773$ and $c = 1$. For the normalization constants H_0 and M_0 in Eqs. (6.20) and (6.28) we follow [275] and set exemplarily, $M_0 = 5.52 \times 10^{-2} \text{ GeV}$ and $H_0 = 3.44 \times 10^{-4} \text{ GeV}^3$. Differentiation of Eqs. (6.28)-(6.31) with respect to h as defined in Eq. (6.20) allows us to determine the cumulants of the critical mode. These expressions are summarized in Ref. [275], and will not be repeated here.

6.2.4 Mapping between spin model and QCD

To utilize the universality class arguments, a mapping between the spin model variables (reduced temperature r and magnetic field h) and the QCD temperature T and baryon-chemical potential μ_B is necessary. Such a mapping is non-universal. Moreover,

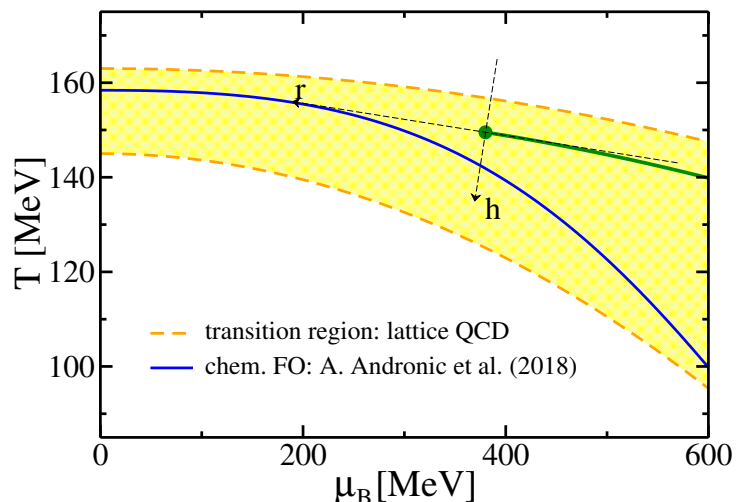


Figure 6.1: The model setup for the location of the critical point. The filled band between the two dashed curves shows lattice QCD results for the location of the chiral crossover transition obtained by solving Eq. (6.34) at leading-order for $\kappa_c = 0.007$ (upper curve, $T_{c,0} = 0.163$ GeV) and $\kappa_c = 0.02$ (lower curve, $T_{c,0} = 0.145$ GeV). The green dot shows the critical point with the attached spin model coordinate system (see the main text for details of the mapping) and the first-order phase transition line for larger μ_B . The solid blue line shows the chemical freeze-out curve from [245].

it is sensitive to the model assumptions. One of the frequently used models is a linear mapping between the spin model and QCD phase diagrams [263, 289]. There, the main assumptions are:

1. The conjectured QCD critical point at (μ_{cp}, T_{cp}) is located at $r = h = 0$ in the Ising model coordinate system,
2. the r axis is tangential at the critical point to the first-order phase transition line in QCD, where the positive r direction points towards the QCD crossover region.

The orientation of the h axis, on the other hand, is not well constrained. In this work, we assume that this axis is perpendicular to the r axis and its positive direction points towards the hadronic phase of QCD. The pictorial representation of our choice can be seen in Fig. 6.1.

To obtain (r, h) corresponding to a given (μ_B, T) pair it is convenient to introduce an auxiliary coordinate system (\tilde{r}, \tilde{h}) , originating at the QCD critical point and oriented such that the \tilde{r} axis is parallel to the μ_B axis. Then the mapping is defined as

$$\tilde{r} = \frac{\mu_B - \mu_{cp}}{\Delta\mu_{cp}}, \quad (6.32)$$

and

$$\tilde{h} = \frac{T - T_{cp}}{\Delta T_{cp}}, \quad (6.33)$$

where ΔT_{cp} and $\Delta\mu_{cp}$ are parameters which are connected to the size of the critical region. Following Ref. [275], we set $\Delta T_{cp} = 0.02$ GeV and $\Delta\mu_{cp} = 0.42$ GeV. The corresponding point in the spin model coordinate system is obtained by rotation of the auxiliary coordinate system, where the angle is determined by the slope of the first-order phase transition line of QCD at the critical point.

The exact location of the QCD critical point and the slope of the first-order phase transition line are not known. Input provided by lattice QCD calculations may be used to constrain these parameters. The crossover line can be parametrized as

$$T_c(\mu_B) = T_{c,0} \left[1 - \kappa_c \left(\frac{\mu_B}{T_c(\mu_B)} \right)^2 + \dots \right], \quad (6.34)$$

where $T_{c,0} = (0.145 \dots 0.163)$ GeV is the critical temperature at vanishing chemical potential [41, 42] and $\kappa_c \simeq 0.007 \dots 0.059$ is the chiral crossover curvature [43–46]. Then, for the given μ_{cp} , $T_{c,0}$ and κ_c , the temperature T_{cp} and the slope of the first-order phase transition line at (μ_{cp}, T_{cp}) can be obtained from Eq. (6.34).

Finally, to make contact between our model calculations and the experimental data on net-proton fluctuations, we calculate the net-proton number cumulants at chemical freeze-out. In this work, we use the chemical freeze-out conditions which were determined by analyzing the measured hadron yields [290–295]. The solid blue line in Fig. 6.1 indicates the recent parametrization from Ref. [245].

6.3 Numerical results on the net-proton number fluctuations

In this section, we discuss the numerical results on different fluctuations of the net-proton number obtained in the above phenomenological approach that correctly embeds the expected scaling behavior of the net-proton variance [282, 283]. To link our results to the STAR data, we first discuss how the experimentally applied kinematic acceptance cuts can be included into the framework. Then, the impact of the phenomenological modification introduced in Eq. (6.24) on fluctuation observables is studied. We also discuss the effects of modifying the coupling strength g and the proximity of the thermal conditions at which the cumulant ratios are evaluated near the QCD critical point.

6.3.1 Kinematic cuts

In the fluctuation measurements, the investigated phase-space coverage is limited by the detector design and specific demands from the experimental analysis, like e.g. to optimize efficiency. Since the observables depend on the implemented kinematic acceptance (see e.g. refs. [253] and [254–256, 296]), it is important to incorporate the experimental cuts into our theoretical framework. Following [297], we include restrictions in kinematic rapidity y , transverse momentum k_T and azimuthal angle ϕ by replacing

$$\int d^3k \longrightarrow \int k_T \sqrt{k_T^2 + m_i^2} \cosh y dk_T dy d\phi, \quad (6.35)$$

and $E_i \rightarrow \sqrt{k_T^2 + m_i^2} \cosh y$ in the momentum-integrals. In line with [256], we consider the following phase-space integrations: $-0.5 \leq y \leq 0.5$, $0 \leq \phi \leq 2\pi$ and $0.4 \text{ GeV}/c \leq k_T \leq 2 \text{ GeV}/c$. We note that this procedure cannot account for scattering of particles in and out of the acceptance window during the late-stage evolution of a medium created in heavy-ion collisions.

6.3.2 Net-proton number cumulant ratios

The contributions of critical fluctuations to the net-proton number cumulants are sensitive to the value of the coupling g between (anti-)protons and the critical mode. This value may, in principle, depend on T and μ_X , i.e. on the position in the QCD phase diagram where the cumulant ratios are evaluated. In fact, in the quark-meson [298] and NJL [299] models, the meson-nucleon couplings are found to decrease both with increasing T and/or μ_B . In the following, we consider fixed values for g along the chemical freeze-out curve depicted in Fig. 6.1, i.e. independent of the beam energy \sqrt{s} . Typical values for g may be inferred from various effective model calculations. In the linear sigma model this parameter can be related in the ground state to the pion decay constant, $g \simeq m_p/f_\pi \simeq 10$ [250, 284]. Similar values can be found in non-linear chiral models [300] describing QCD matter in neutron stars. On the other hand, based on different quark-meson models the value of $g \simeq 3 - 7$ for the nucleon-meson couplings is well conceivable [301]. To highlight the features of our model results, we will use g in the range between 3 and 5.

In Ref. [275], the critical point was exemplarily located at $\mu_{cp} = 0.39 \text{ GeV}$ and $T_{cp} = 0.149 \text{ GeV}$ (see Fig. 6.1). There, even for rather small values of $g \simeq 3$, the cumulant ratio C_2/C_1 exhibited a clear peak structure compared to the non-critical baseline and in contrast to the STAR data [253–256]. This is illustrated in Fig. 6.2.

The effect of the modified scaling, discussed in Sec. 6.2.2, is the substantial reduction of the critical contribution to C_2 in Eq. (6.25) implying the disappearance of the maximum in C_2/C_1 even for large values of $g \simeq 5$, as seen in Fig. 6.2. Within error bars, the model

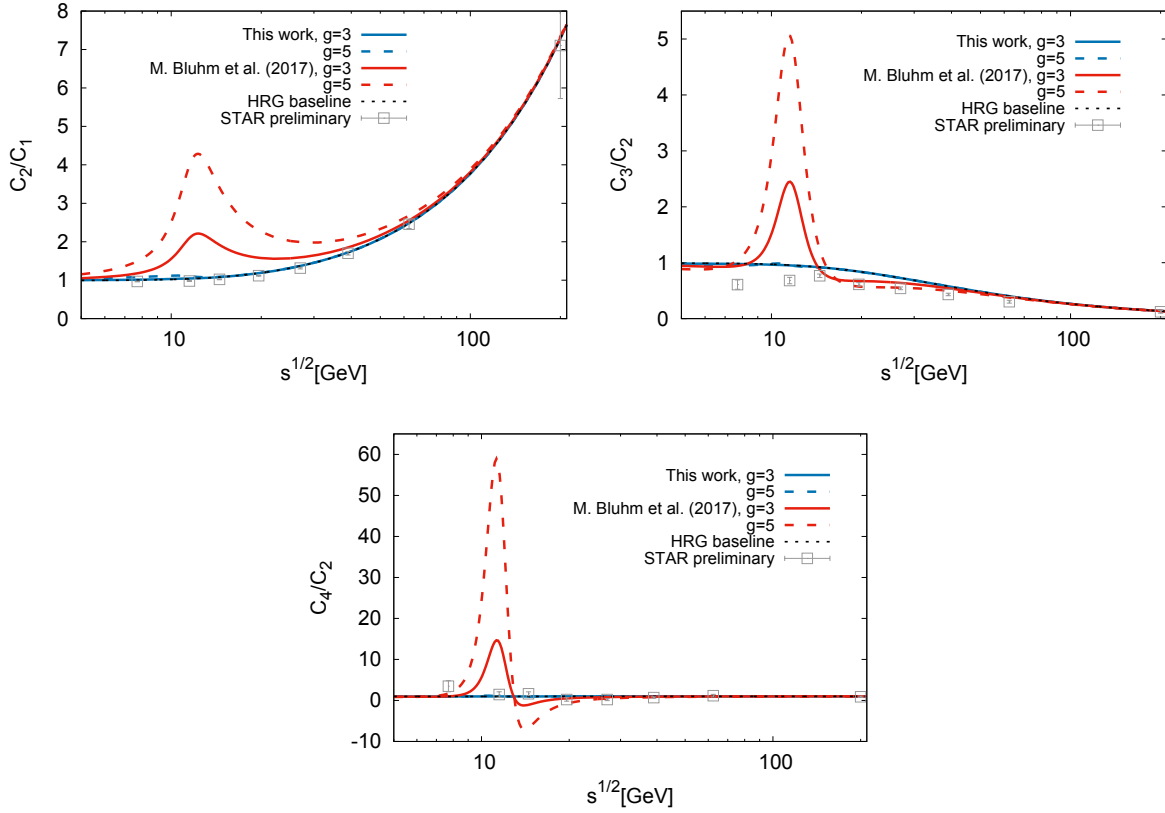


Figure 6.2: Net-proton number cumulant ratios from Eq. (6.5) calculated following Ref. [275] for $g = 3$ and 5 (red solid and dashed lines, respectively) in comparison with present model results (blue solid and dashed lines, respectively). We note that we modified the set-up compared to Ref. [275], i.e. we changed the orientation of the h -axis, neglected resonance decays, considered different freeze-out conditions and applied a different parametrization of the magnetic equation of state. For comparison, we also show the preliminary STAR data on the net-proton number fluctuations [256] (squares, where the error bars contain both statistical and systematic errors). Also shown are results for the non-critical baseline (black dotted lines).

results are in agreement with data of the STAR Collaboration [256] on the C_2/C_1 ratio. We note that to see a similar maximum in C_2/C_1 in this model calculations, as found in [275] for a given location of the critical point, a significantly larger value of g , outside the expected range discussed above, would be necessary. Furthermore, the differences between the C_2/C_1 ratios shown in Fig. 6.2 are independent of the particular choice for the phenomenological freeze-out conditions. Indeed, in these studies, we have adopted the freeze-out line from Ref. [245], whereas in [275] the C_2/C_1 ratio was calculated along the freeze-out line from Refs. [302, 303].

The higher-order cumulant ratios of the net-proton number fluctuations are also shown

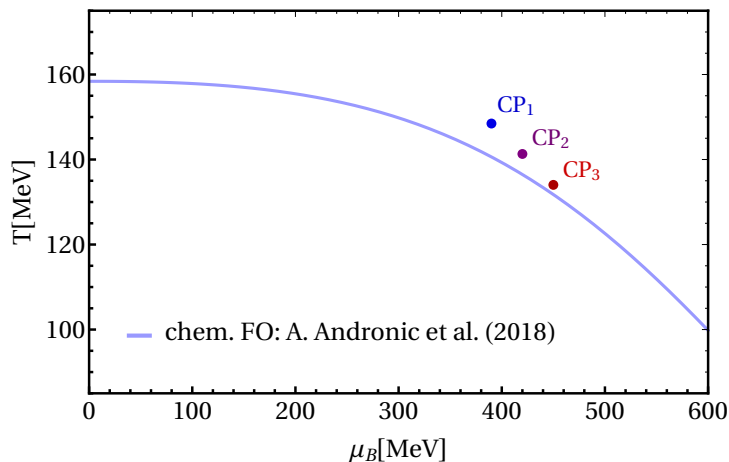


Figure 6.3: Locations of the QCD critical points from Tab. 6.1 plotted together with the chemical freeze-out line [245] used in this work.

in Fig. 6.2. The model introduced in [275] exhibits clearly pronounced non-monotonic structures of higher-order cumulant ratios for $g = 3$ and 5. We note, that while in the model [275] the ratios C_2/C_1 and C_4/C_2 are independent of the choice made for the orientation of the h -axis, the behavior of C_3/C_2 is sensitive to this choice. In [275], the positive direction of the h -axis was defined to point upward towards larger values of T . In our work, we choose the opposite direction as discussed in Sec. 6.2.4 such that $g\sigma$ is positive along the chemical freeze-out curve.

As seen in Fig. 6.2, in the present model calculations, the non-monotonic structures of the higher-order cumulant ratios become strongly suppressed even for $g = 5$. In fact, for the considered setup, the model results show rather small deviations from the non-critical baseline. Moreover, in contrast to [275], the behavior of C_3/C_2 in the present model (blue lines in Fig. 6.2) does not depend on the orientation of h . This is because the combined θ -dependence in C_3 of the critical mode fluctuations $\langle (V\delta\sigma)^3 \rangle$ and the factor σ^3 is even, see Eq. (6.26). Thus, although h is an odd function in θ as seen from Eqs. (6.30) and (6.31), a re-orientation of the h -axis would have no effect.

The substantial reduction of the critical signal in the net-proton number cumulant ratios seen in results obtained in the current model is a consequence of the reduced scaling of the critical contributions to $C_{n=2,3,4}$ in Eqs. (6.25)-(6.27) and the magnitude of the factors $(g\sigma)^n$. As a result of the phenomenological implementation in Eq. (6.24), the scaling of C_n at the CP is weakened by an additional $n\beta$ factor in the critical exponents. Moreover, the factor $g\sigma$ differs from the vacuum proton mass m_p in Eq. (6.22) as employed in [275]. In the present calculations, $g\sigma$ is of the order of 0.2–0.3 GeV for most \sqrt{s} . Its actual values depend on the parameters in the magnetic equation of state, most notably on the value of M_0 (see Sec. 6.2.3), and the mapping between spin model and QCD (see Sec. 6.2.4). These values receive support from recent works on the origin of the baryon masses in both

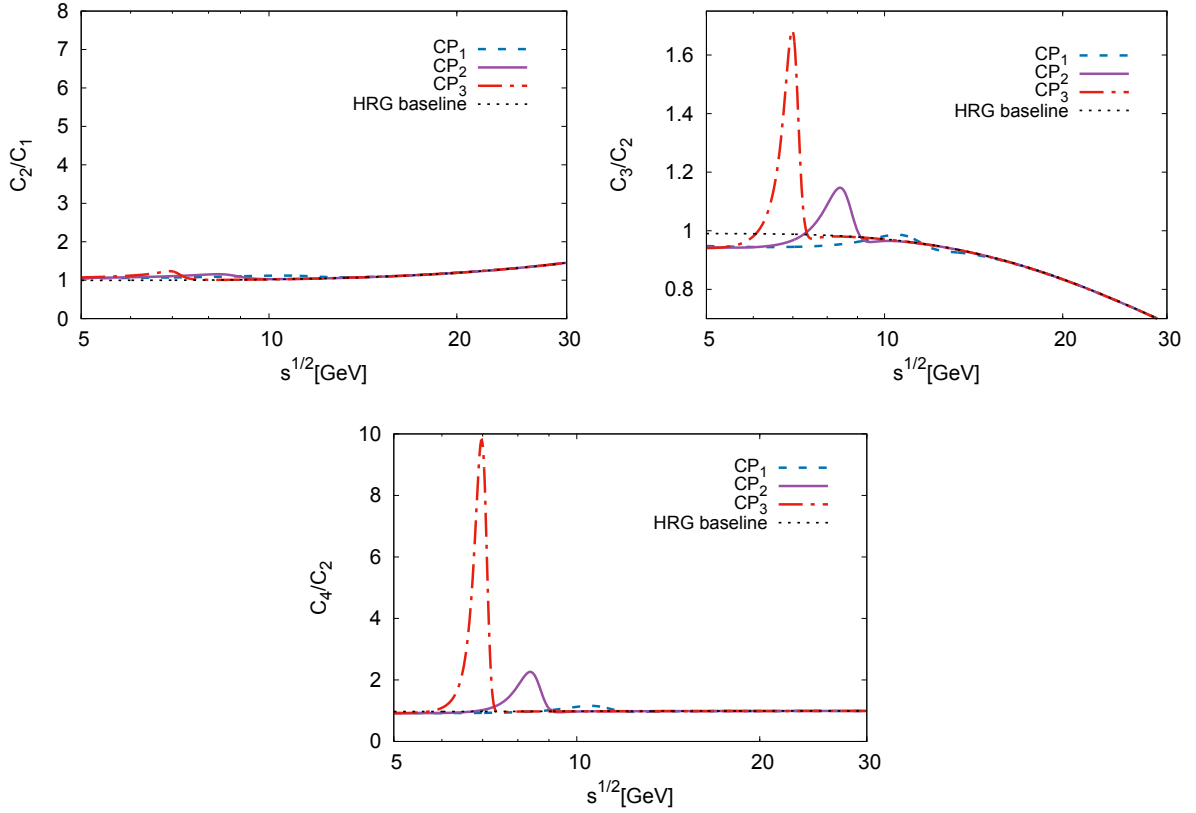


Figure 6.4: Ratios of the net-proton number cumulants from Eq. (6.5) calculated in the present model for fixed $g = 5$ and for different locations of the QCD critical point as listed in Tab. 6.1.

lattice QCD [304, 305] and effective models based on parity doubling [306, 307]. There, the ground state baryon masses are found to be given to a large extent by σ -independent contributions.

The properties of different cumulant ratios shown in Fig. 6.2 can lead to the conclusion that the monotonic beam energy dependence seen experimentally in C_2/C_1 together with the non-monotonicity in the higher-order cumulant ratios cannot be explained simultaneously by a model that includes critical mode fluctuations through the coupling of σ with the particles and obeys the connection between the chiral and net-baryon number susceptibilities observed in effective models [282, 283]. However, one notes that the model results depend not only on the values of the coupling g but also on the non-universal details of the mapping between QCD and the spin model discussed in Sec. 6.2.4. One of them is the unknown distance of the QCD critical point from the chemical freeze-out conditions at which the fluctuations are determined. To study this effect, we keep the chemical freeze-out conditions fixed but vary the location of the critical point in the QCD phase diagram, as summarized in Tab. 6.1 and depicted in Fig. 6.3.

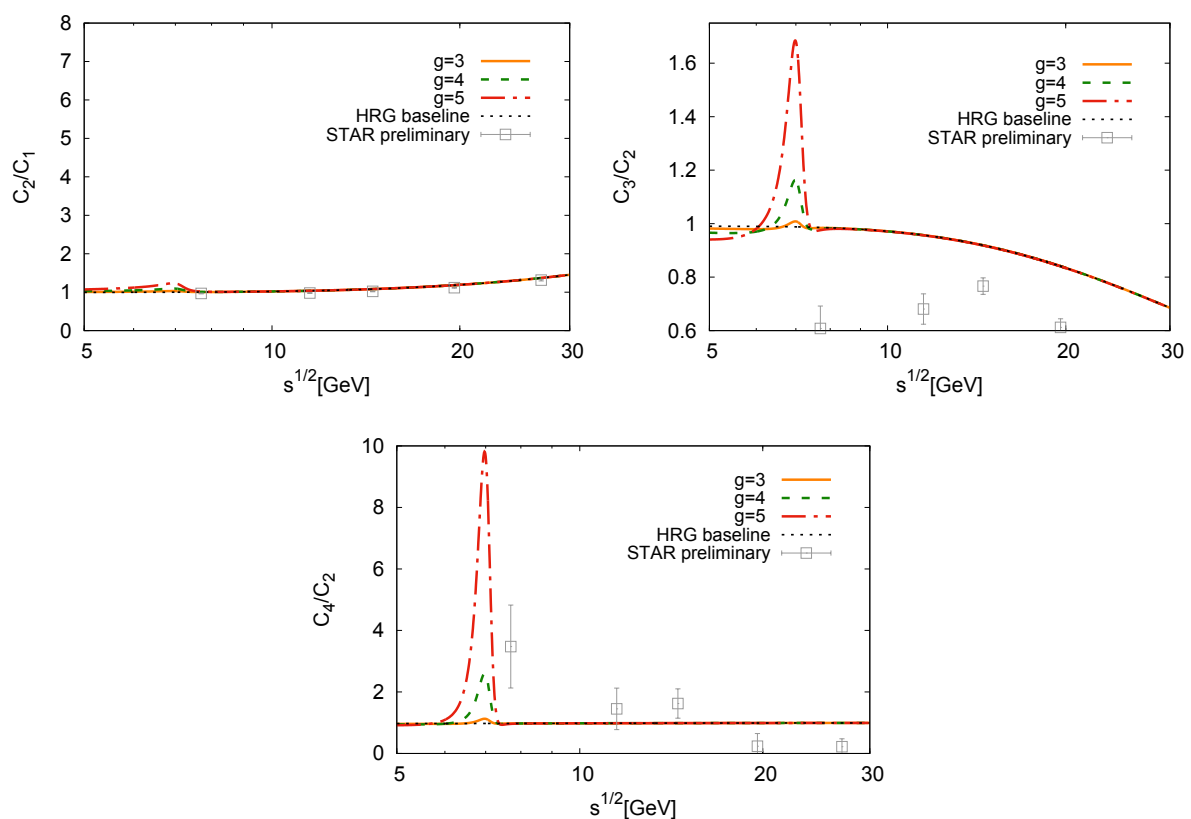


Figure 6.5: Net-proton number cumulant ratios from Eq. (6.5) calculated with the CP₃-setup for the location of the CP (see Tab. 6.1) and for different values of the coupling $g = 3, 4$ and 5 (orange solid, green long-dashed and red dash-dotted lines, respectively). The preliminary STAR data for the net-proton number fluctuations [256] (squares, where the error bars contain both statistical and systematic errors) are shown for comparison. The non-critical baseline model results are shown by black dotted lines.

In Fig. 6.4 we show the net-proton number fluctuations along the phenomenological freeze-out line at fixed value of the coupling $g = 5$ and assuming different locations of the CP. As evident from this figure, moving the critical point closer to the chemical freeze-out curve leads to an increase of non-monotonic structures in the net-proton number cumulant ratios. While deviations from the non-critical baseline (black dotted lines) remain moderately weak in C_2/C_1 , they become more pronounced with increasing order of the fluctuations in C_n/C_2 ratios. We note that even for CP₃ we always remain at a distance of about or larger than 3 MeV in μ_B along the chemical freeze-out line.

In Fig. 6.5 we show the influence of the critical point located at the closest distance CP₃ on the energy dependence of the net-proton number fluctuations for different values of the coupling g . As can be seen, all cumulant ratios depend strongly on the actual value of g . This behavior is expected from Eqs. (6.25)-(6.27) and Eq. (6.23) since cumulants

C_n scale as g^{2n} . This differs from the model introduced in [275] where, as seen from Eqs. (6.16)-(6.19), they scale only as g^n . When compared to the STAR data, the results for C_2/C_1 and C_4/C_2 shown in Fig. 6.5 are in qualitative agreement with the data, given the uncertainties in the model assumptions. However, the C_3/C_2 ratio also increases beyond the non-critical baseline towards the lower beam energies, in contrast to the STAR data.

From the results shown in Figs. 6.2, 6.4 and 6.5 it is clear that for small couplings $g \simeq 3$ deviations from the non-critical baseline are negligible in all cumulant ratios irrespective of the studied location of the critical point. By increasing g , non-monotonic structures in the \sqrt{s} -dependence of the net-proton cumulant ratios develop and are sensitive to the relative distance between the critical point and the chemical freeze-out curve. This behavior is also stronger in the higher-order cumulant ratios.

It is therefore conceivable that, by an appropriate choice of the location of the CP and the model parameters, it is possible to describe the energy dependence of some ratios of the net-proton number fluctuations as seen in the preliminary STAR data. Consequently, the rather strong increase of the C_4/C_2 ratio beyond the HRG baseline and the smooth dependence of C_2/C_1 observed in heavy-ion collisions at energies $\sqrt{s} < 20$ GeV could be due to the contribution from the CP located near the chemical freeze-out line. However, in this case the C_3/C_2 ratio should also exceed the non-critical baseline, which is not seen experimentally.

Thus, based on the presented equilibrium model results one concludes, that the energy dependence of the C_4/C_2 , C_3/C_2 and C_2/C_1 ratios observed in heavy ion collisions at $\sqrt{s} < 20$ GeV by the STAR Collaboration does not follow the systematics expected from the contribution of the CP to the net-proton number fluctuations alone. This conclusion is consistent with the previous analysis of different fluctuation observables based on lattice QCD and PNJL model results [69, 70]. We note, however, that the above statement requires further theoretical and empirical justifications due to current uncertainties in the model assumptions and the experimental data.

Table 6.1: Considered locations of the QCD critical point in the (μ_B, T) -plane. The parameters $T_{c,0}$ and κ_c of the crossover (pseudo-critical) line Eq. (6.34) needed to determine T_{cp} and the slope of the first-order phase transition line at the critical point for a given μ_{cp} are also listed. The locations of these critical points in the QCD phase diagram are shown in Fig. 6.3.

CP_i	μ_{cp} [GeV]	T_{cp} [GeV]	$T_{c,0}$ [GeV]	κ_c
1	0.390	0.149	0.156	0.007
2	0.420	0.141	0.155	0.010
3	0.450	0.134	0.155	0.012

Chapter 7

Conclusions and outlook

In this thesis, we explored various aspects of deconfinement and chiral transition using effective models. We showed the utility of Polyakov loop fluctuations for investigating deconfinement and explored the impact of finite magnetic field and chemical potential on this phenomenon. We also studied the role of in-medium effects in generating the inverse magnetic catalysis and formulated a phenomenological model which captures the effect of the hidden tricritical point and investigated its effect on net-proton number fluctuations. In the following, we summarize the most important results of our work.

In Chapter 4 we argued that Polyakov loop suffers from the renormalization scheme dependence when calculated on lattice, and thus it is essential to study also other observables sensitive to deconfinement. We focused on Polyakov loop susceptibilities and their ratios. Using an effective model, we demonstrated how features of deconfinement emerge from these observables. For the R_A ratio, we found a characteristic volume dependence along with temperature and the explicit $Z(3)$ symmetry breaking strength h . In a Gaussian approximation scheme, these features follow from a single scaling equation and, after a particular mapping procedure, can be seen also in the full model. The R_T ratio shows very weak volume dependence, which makes it a robust probe of the strength of the explicit center symmetry breaking. The effective model discussed in Chapter 4 is capable of describing many features of the LQCD results on a qualitative level. Especially, these include the low and high temperature limits of the ratios, as well as connection between R_A and R_T . As our results indicate, the latter may be possibly via the explicit center symmetry breaking strength, h . Additionally, the lattice data on ratio observables may provide additional constraints on effective models. As an example, we argued that one of the commonly used chiral models, the PNJL model, leads to significantly smaller $Z(3)$ breaking strength than suggested by the lattice. This indicates that the naive coupling between quarks and gluons is not sufficient, and more sophisticated treatment may be necessary.

In Chapter 5 we investigated an impact of strong magnetic field and chemical potential on

Polyakov loop and its fluctuations, by generalizing the model introduced in the previous chapter. We started from the heavy quark approximation, in which effects due to the chiral dynamics may be neglected. We showed that the external magnetic field tends to increase the strength of the explicit center symmetry breaking, both for the full one-loop fermion potential and its linear approximation. The asymptotic behavior of the latter at small and large magnetic fields was investigated. We also demonstrated that taking into account the higher-order terms of the one-loop fermionic potential does not lead to substantial changes in the center symmetry breaking strength, at least at the mean-field level. With the schematic mean-field calculation, it was shown that the deconfinement transition is sensitive to magnetic field, which was inferred from the behavior of the Polyakov loop and its fluctuations. The longitudinal susceptibility is diverging at the critical point, while the transverse one remains finite. Therefore, χ_L may be used to probe the deconfinement critical point. We found that the critical temperature decreases with B for a fixed quark mass and the critical quark mass (i.e. the mass for which deconfinement becomes second-order transition) increases with magnetic field. Magnetic field also shrinks the region of first-order transition in the (m_l, m_s) plane.

When the light quarks are considered, the chiral dynamics has to be taken into account to obtain an accurate description of the QCD medium. Magnetic field shows a non-trivial interplay with the chiral dynamics, which results in magnetic catalysis and inverse magnetic catalysis. Moreover, the deconfinement temperature decreases with B . This provides additional test for effective models. While most chiral models are capable of describing MC, they predict the opposite trends for the behavior of the condensate near the transition region and the critical temperature. To show a delicate interplay between the chiral dynamics and deconfinement, we investigated the effective breaking strength $h[M_Q(T, B), T, B]$ in the PNJL model and using the lattice-improved quark mass function. We found that for the latter, the trend in deconfinement temperature agrees with LQCD observations. Our analysis may be useful for constraining missing interactions in effective chiral models.

To demonstrate the importance of in-medium effects for a proper description of chiral dynamics, we investigated effects of screening of four-quark interaction by the ring diagram. Our starting point was a field-theoretical model inspired by QCD in the Coulomb gauge. Dressing of interactions results in an effective medium-dependent coupling, which decreases with T and B . This allows to resolve the problem of an overestimated chiral transition temperature in common PNJL-type models. At finite temperature and magnetic field, the screening is capable of generating an inverse magnetic catalysis. The screening affects also deconfinement which is transparent from the significant response of the Polyakov loop to a magnetic field, in comparison to the model with the bare coupling.

We also investigated the simultaneous effect of magnetic field and quark chemical potential on deconfinement of heavy quarks. The behavior of the Polyakov loop, its susceptibilities as well as the R_T ratio indicates that magnetic field tend to increase the strength of the explicit center symmetry breaking, similarly to finite B . The crucial difference is

that the finite chemical potential makes effective action complex which, in turn, leads to splitting between $\langle \ell \rangle$ and $\langle \bar{\ell} \rangle$. On the other hand, the magnetic field does not induce such a splitting. We found that the transverse susceptibility, χ_T , becomes sensitive to the critical point at finite density. We also investigated the static quark and anti-quark entropies. When the chemical potential is non-zero, S_Q and $S_{\bar{Q}}$ are no longer identical, and we found that their maxima in the crossover region are located at slightly different temperatures.

In Chapter 6 we studied the influence of the QCD critical end point on the properties of the first four cumulants (C_n) of the net-proton number and their ratios. The results were addressed in the context of the recent data from the STAR Collaboration on the energy dependence of the net-proton number fluctuations obtained within the Beam Energy Scan program at the RHIC. The net-proton number cumulants were calculated using a phenomenological model [275] where non-critical fluctuations are obtained from the hadron resonance gas model. For simplicity, the baryonic sector of the HRG was approximated by contributions from primary protons and anti-protons. The criticality was embedded by linking their masses to the σ mode, as suggested by various chiral models. In consequence, the (anti-)proton mass and its momentum distribution function fluctuate on an event-by-event basis around their mean or equilibrium value, respectively. The critical mode fluctuations were determined by applying the universality class arguments between QCD and the 3-dimensional Ising spin model. We have extended this model by accounting for the critical scaling behavior of the net-baryon variance χ_B suggested by effective chiral models. There, χ_B is linked to the product of the chiral susceptibility and the chiral order parameter squared. This allowed to embed into the model, in a phenomenological way, the overlap between a hidden $O(4)$ and the $Z(2)$ criticality which is theoretically expected near CP up to a tiny region in μ_B [278].

We have found a substantial reduction of the critical mode contributions to the net-proton number fluctuations compared to the results in Ref. [275]. This is a consequence of the reduced critical scaling imposed by respecting the proper scaling relation between net-baryon number and chiral susceptibilities and the size of the proton mass modification due to the coupling to the σ mode. This brings our results for different cumulants (C_n) of the net-proton number, calculated along the phenomenological chemical freeze-out line, closer to the experimental observations made by the STAR Collaboration for the energy dependence of the cumulant ratios in heavy-ion collisions at RHIC. In particular, with an appropriate choice of the model parameters and the location of the CP relative to the chemical freeze-out line, the model can reproduce the smooth energy dependence of C_2/C_1 and the increase and non-monotonic variation of C_4/C_2 towards lower beam energies, as is observed by the STAR Collaboration. However, the decrease of the C_3/C_2 ratio towards lower beam energies seen in the STAR data is inconsistent with the systematics expected in the present model from the contribution of the CP, which would predict access of this ratio beyond the non-critical baseline. Thus, our conclusion is that it is rather unlikely that the properties observed in the low-energy behavior of different ratios of the net-

proton number cumulants in heavy-ion collisions are due to the existence of the critical point near the phenomenological chemical freeze-out line alone. However, because of various uncertainties, this interesting result requires further investigation.

In the final remarks of this work, we list various open questions and new research possibilities which we encountered during our investigation of QCD phase transitions. The LQCD results on ratio observables, to which we compared our model results in Chapter 4 and which were used to estimate the center symmetry breaking strength on the lattice, still suffer from a renormalization scheme dependence. This issue should be resolved to achieve a meaningful comparison of effective approaches with LQCD. Additionally, a more detailed studies of fluctuation observables within LQCD could be helpful in distinguishing various beyond mean-field effects, for example the spatial dependence of the Polyakov loops and their correlators. Another suggestion is to study the magnetic field dependence of Polyakov loop susceptibilities and ratio observables. Note, that from the color group integration approach χ_A and, in consequence, R_A are expected to be explicitly volume-dependent. To extract useful information from these quantities, they need to be studied either at a finite volume, or as a function of the scaling variable ξ . Investigation of the spatial dependence of correlation functions [218] and establishing the relation between correlation functions and the susceptibilities could guide the study of the spatial- or momentum-dependence of the Polyakov loop fields, which are constant in the mean-field approach.

We also demonstrated that in-medium screening may generate IMC in the class of models. These promising results motivate us to further explore this type of model to investigate the QCD phase structure. We studied order parameters, however, the effect of screening on susceptibilities and ratio observables remains to be seen. It would also be interesting to investigate the screening effects at finite baryon chemical potential, which may lead to new insights into the finite density region of the QCD phase diagram, including the conjectured QCD critical point. It is also important to incorporate other physical effects, which are absent in that model. This includes, for example, an explicit treatment of dynamical gluons (and ghosts) in the confinement model which gives a natural extension to introduce non-local interactions among quarks. This would allow to explore the role played by the gluons in a chiral phase transition.

Finally, there are also several uncertainties regarding the results presented in Chapter 6. It remains to be seen, for example, whether non-equilibrium effects can push the C_3/C_2 ratio below the non-critical HRG model baseline. Moreover, the fireball evolution or late hadronic stage processes such as resonance decays or isospin randomization, which have not been included in our study, may influence the theoretical results.

Appendices

Appendix A

Effective gluon potential

In this appendix we provide the details of the effective gluon potential [141] used in calculations presented in the thesis. The potential reads

$$U_G = -\frac{1}{2}A\ell\bar{\ell} + B \ln M_H(\ell, \bar{\ell}) + \frac{1}{2}C(\ell^3 + \bar{\ell}^3) + D(\ell\bar{\ell})^2, \quad (\text{A.1})$$

where ℓ and $\bar{\ell}$ are the Polyakov loop and its conjugate and M_H is the $SU(3)$ Haar measure,

$$M_H(\ell, \bar{\ell}) = 1 - 6\ell\bar{\ell} + 4(\ell^3 + \bar{\ell}^3) - 3(\ell\bar{\ell})^2. \quad (\text{A.2})$$

The Haar measure allows to take into account the structure of the gauge group of QCD. The logarithmic term is well-defined only for Polyakov loop and its conjugate for which $M_H(\ell, \bar{\ell}) > 0$

Temperature-dependent coefficients A , B , C and D were determined such that the potential captures lattice results [139] for the pure gauge pressure, Polyakov loop expectation value and its longitudinal as well as transverse susceptibilities. Therefore, not only the position of the minimum is adjusted to LQCD data but also the curvature of the potential which makes it particularly suited to study Polyakov loop fluctuations. Parameters A , B and C are of the following form,

$$X = \frac{x_1 + x_2/t + x_3/t^2}{1 + x_4/t + x_5/t^2} \quad (\text{A.3})$$

and the coefficient B is given by

$$B = b_1 \left(1 - e^{b_2/t^{b_3}}\right) t^{-b_4}. \quad (\text{A.4})$$

In both equations $t = T/T_c$, where $T_c \approx 270$ MeV is the deconfinement temperature of the pure gauge $SU(3)$ theory. Numerical constants are listed in tab. A.1.

Appendix A. Effective gluon potential

a_1	a_2	a_3	a_4	a_5
-44.14	151.4	-90.0677	2.77173	3.56403
b_1	b_2	b_3	b_4	
-0.32665	-82.9823	3.0	5.85559	
c_1	c_2	c_3	c_4	c_5
-50.7961	114.038	-89.4596	3.08718	6.72812
d_1	d_2	d_3	d_4	d_5
27.0885	-56.0859	71.2225	2.9715	6.61433

Table A.1: Numerical parameters for coefficients A , B , C and D in the Polyakov loop potential (A.1), obtained from Ref. [141].

Alternatively, the potential can be expressed in terms of the real and imaginary parts of the Polyakov loop,

$$\begin{aligned}\ell &= x + iy, \\ \bar{\ell} &= x - iy,\end{aligned}\tag{A.5}$$

which is an equivalent basis to ℓ , $\bar{\ell}$ when the quark chemical potential vanishes (when $\mu \neq 0$, the mixing between the real and imaginary parts results in $\ell \neq \bar{\ell}$ [154]). The effective potential expressed in terms of x and y is

$$U_G = -\frac{1}{2}A(x^2 + y^2) + B \ln M_H + C(x^3 - 3xy^2) + D(x^2 + y^2)^2\tag{A.6}$$

and the Haar measure (A.2) is

$$M_H = 1 - 6(x^2 + y^2) + 8(x^3 - 3xy^2) - 3(x^2 + y^2)^2.\tag{A.7}$$

On the mean-field level the expectation values are obtained by solving the gap equations

$$\begin{aligned}\frac{\partial U_G}{\partial x} &= 0 \\ \frac{\partial U_G}{\partial y} &= 0\end{aligned}\tag{A.8}$$

For the first equation one finds

$$\frac{1}{T^4} \frac{\partial U}{\partial x} = -Ax + \frac{B}{M_H(x, y)} \frac{\partial M_H(x, y)}{\partial x} + 3C(x^2 - y^2) + 4D(x^3 + xy^2),\tag{A.9}$$

where

$$\frac{\partial M_H(x, y)}{\partial x} = -12x + 24(x^2 - y^2) - 12(x^3 + y^2x).\tag{A.10}$$

For the second equation one finds

$$\frac{1}{T^4} \frac{\partial U}{\partial y} = -Ay + \frac{B}{M_H} \frac{\partial M_H}{\partial y} - 6Cxy + 4D(y^3 + x^2y), \quad (\text{A.11})$$

where

$$\frac{\partial M_H}{\partial y} = -12y - 48xy - 12(y^3 + x^2y). \quad (\text{A.12})$$

In the deconfined phase the center symmetry is spontaneously broken and the gluon potential (A.6) has three minima. Here we focus on the real sector ($x \rightarrow x_0, y \rightarrow 0$). In this case Eq. (A.11) vanishes and the minimum can be determined from a single equation

$$\left. \frac{1}{T^4} \frac{\partial U}{\partial x} \right|_{x=x_0} = -Ax_0 - 12B \frac{x_0 - 2x_0^2 + x_0^3}{1 - 6x_0^2 + 8x_0^3 - 3x_0^4} + 3Cx_0^2 + 4Dx_0^3. \quad (\text{A.13})$$

The susceptibilities can be obtained by inverting the curvature matrix:

$$T^3 \hat{\chi} = (\hat{C})^{-1}, \quad (\text{A.14})$$

where

$$\hat{C} = \begin{pmatrix} \frac{\partial^2 U}{\partial x^2} & \frac{\partial^2 U}{\partial x \partial y} \\ \frac{\partial^2 U}{\partial y \partial x} & \frac{\partial^2 U}{\partial y^2} \end{pmatrix}. \quad (\text{A.15})$$

The longitudinal component of the curvature matrix reads

$$\begin{aligned} \hat{C}_{xx} = \frac{\partial^2 U}{\partial x^2} &= -A + \frac{B}{M_H} \frac{\partial^2 M_H}{\partial x^2} - \frac{B}{M_H^2} \left(\frac{\partial M_H}{\partial x} \right)^2 \\ &+ 6Cx + 4D(3x^2 + y^2), \end{aligned} \quad (\text{A.16})$$

where

$$\frac{\partial^2 M_H}{\partial x^2} = -12 + 48x - 12(3x^2 + y^2). \quad (\text{A.17})$$

The mixed component reads

$$\begin{aligned} \hat{C}_{xy} = \frac{1}{T^4} \frac{\partial^2 U}{\partial x \partial y} &= \frac{B}{M_H} \frac{\partial^2 M_H}{\partial y \partial x} - \frac{B}{M_H^2} \frac{\partial M_H}{\partial x} \frac{\partial M_H}{\partial y} \\ &- 6Cy + 8Dyx, \end{aligned} \quad (\text{A.18})$$

where

$$\frac{\partial^2 M_H}{\partial x \partial y} = -48y - 24xy. \quad (\text{A.19})$$

The transverse component is

$$\hat{C}_{yy} = \frac{1}{T^4} \frac{\partial^2 U}{\partial y^2} = -A + \frac{B}{M_H} \frac{\partial^2 M_H}{\partial y^2} - \frac{B}{M_H^2} \left(\frac{\partial M_H}{\partial y} \right)^2 - 6Cx + 4D(3y^2 + x^2), \quad (\text{A.20})$$

where

$$\frac{\partial^2 M_H}{\partial y^2} = -12 - 48x - 12(3y^2 + x^2). \quad (\text{A.21})$$

In the real sector these expression are considerably simplified. First, we note that the off-diagonal terms vanish. The longitudinal term becomes

$$\hat{C}_{xx} = -A - B \left[\frac{9}{(3x_0 + 1)^2} + \frac{3}{(x_0 - 1)^2} \right] + 6Cx_0 + 12Dx_0^2. \quad (\text{A.22})$$

and the the transverse component is

$$\hat{C}_{yy} = -A + 12B \frac{x_0^2 + 4x_0 + 1}{(3x_0 + 1)(x_0 - 1)^3} - 6Cx_0 + 4Dx_0^2. \quad (\text{A.23})$$

Corresponding susceptibilities are given by inverse of \hat{C}_{xx} and \hat{C}_{yy} .

Bibliography

- [1] H. Fritzsche, Murray Gell-Mann, and H. Leutwyler. Advantages of the Color Octet Gluon Picture. *Phys. Lett. B*, 47:365–368, 1973. doi: 10.1016/0370-2693(73)90625-4.
- [2] Steven Weinberg. Nonabelian Gauge Theories of the Strong Interactions. *Phys. Rev. Lett.*, 31:494–497, 1973. doi: 10.1103/PhysRevLett.31.494.
- [3] Frank Wilczek. Quantum Chromodynamics (QCD): The Modern Theory of the Strong Interaction. *Ann. Rev. Nucl. Part. Sci.*, 32:177–209, 1982. doi: 10.1146/annurev.ns.32.120182.001141.
- [4] P. A. Zyla et al. Review of Particle Physics. *PTEP*, 2020(8):083C01, 2020. doi: 10.1093/ptep/ptaa104.
- [5] David J. Gross and Frank Wilczek. Ultraviolet Behavior of Nonabelian Gauge Theories. *Phys. Rev. Lett.*, 30:1343–1346, 1973. doi: 10.1103/PhysRevLett.30.1343.
- [6] D. J. Gross and Frank Wilczek. Asymptotically Free Gauge Theories - I. *Phys. Rev. D*, 8:3633–3652, 1973. doi: 10.1103/PhysRevD.8.3633.
- [7] H. David Politzer. Reliable Perturbative Results for Strong Interactions? *Phys. Rev. Lett.*, 30:1346–1349, 1973. doi: 10.1103/PhysRevLett.30.1346.
- [8] T. P. Cheng and L. F. Li. *Gauge theory of elementary particle physics*. Oxford University Press, Oxford, UK, 1984. ISBN 978-0-19-851961-4, 978-0-19-851961-4.
- [9] Michael E. Peskin and Daniel V. Schroeder. *An Introduction to quantum field theory*. Addison-Wesley, Reading, USA, 1995. ISBN 978-0-201-50397-5.
- [10] Vladimir A. Miransky. *Dynamical Symmetry Breaking in Quantum Field Theories*. WORLD SCIENTIFIC, 1994. ISBN 978-981-02-1558-3.
- [11] John C. Collins and M. J. Perry. Superdense Matter: Neutrons Or Asymptotically Free Quarks? *Phys. Rev. Lett.*, 34:1353, 1975. doi: 10.1103/PhysRevLett.34.1353.
- [12] N. Cabibbo and G. Parisi. Exponential Hadronic Spectrum and Quark Liberation. *Phys. Lett. B*, 59:67–69, 1975. doi: 10.1016/0370-2693(75)90158-6.

- [13] Edward V. Shuryak. Theory of Hadronic Plasma. *Sov. Phys. JETP*, 47:212–219, 1978.
- [14] Edward V. Shuryak. Quark-Gluon Plasma and Hadronic Production of Leptons, Photons and Psions. *Phys. Lett. B*, 78:150, 1978. doi: 10.1016/0370-2693(78)90370-2.
- [15] Ulrich W. Heinz and Maurice Jacob. Evidence for a new state of matter: An Assessment of the results from the CERN lead beam program. 1 2000.
- [16] Peter Braun-Munzinger, Volker Koch, Thomas Schäfer, and Johanna Stachel. Properties of hot and dense matter from relativistic heavy ion collisions. *Phys. Rept.*, 621:76–126, 2016. doi: 10.1016/j.physrep.2015.12.003.
- [17] Claudia Ratti. Lattice QCD and heavy ion collisions: a review of recent progress. *Rept. Prog. Phys.*, 81(8):084301, 2018. doi: 10.1088/1361-6633/aabb97.
- [18] Michael Buballa. NJL model analysis of quark matter at large density. *Phys. Rept.*, 407:205–376, 2005. doi: 10.1016/j.physrep.2004.11.004.
- [19] Kenji Fukushima and Tetsuo Hatsuda. The phase diagram of dense QCD. *Rept. Prog. Phys.*, 74:014001, 2011. doi: 10.1088/0034-4885/74/1/014001.
- [20] Kenji Fukushima. QCD matter in extreme environments. *J. Phys. G*, 39:013101, 2012. doi: 10.1088/0954-3899/39/1/013101.
- [21] Kenji Fukushima and Chihiro Sasaki. The phase diagram of nuclear and quark matter at high baryon density. *Prog. Part. Nucl. Phys.*, 72:99–154, 2013. doi: 10.1016/j.ppnp.2013.05.003.
- [22] Dmitri E. Kharzeev, Karl Landsteiner, Andreas Schmitt, and Ho-Ung Yee. ‘Strongly interacting matter in magnetic fields’: an overview. *Lect. Notes Phys.*, 871:1–11, 2013. doi: 10.1007/978-3-642-37305-3_1.
- [23] Igor A. Shovkovy. Magnetic Catalysis: A Review. *Lect. Notes Phys.*, 871:13–49, 2013. doi: 10.1007/978-3-642-37305-3_2.
- [24] Jens O. Andersen, William R. Naylor, and Anders Tranberg. Phase diagram of QCD in a magnetic field: A review. *Rev. Mod. Phys.*, 88:025001, 2016. doi: 10.1103/RevModPhys.88.025001.
- [25] Vladimir A. Miransky and Igor A. Shovkovy. Quantum field theory in a magnetic field: From quantum chromodynamics to graphene and Dirac semimetals. *Phys. Rept.*, 576:1–209, 2015. doi: 10.1016/j.physrep.2015.02.003.
- [26] Kenji Fukushima. Extreme matter in electromagnetic fields and rotation. *Prog. Part. Nucl. Phys.*, 107:167–199, 2019. doi: 10.1016/j.ppnp.2019.04.001.

-
- [27] Dmitri E. Kharzeev, Larry D. McLerran, and Harmen J. Warringa. The Effects of topological charge change in heavy ion collisions: 'Event by event P and CP violation'. *Nucl. Phys. A*, 803:227–253, 2008. doi: 10.1016/j.nuclphysa.2008.02.298.
- [28] V. Skokov, A. Yu. Illarionov, and V. Toneev. Estimate of the magnetic field strength in heavy-ion collisions. *Int. J. Mod. Phys. A*, 24:5925–5932, 2009. doi: 10.1142/S0217751X09047570.
- [29] V. Voronyuk, V. D. Toneev, W. Cassing, E. L. Bratkovskaya, V. P. Konchakovski, and S. A. Voloshin. (Electro-)Magnetic field evolution in relativistic heavy-ion collisions. *Phys. Rev. C*, 83:054911, 2011. doi: 10.1103/PhysRevC.83.054911.
- [30] Adam Bzdak and Vladimir Skokov. Event-by-event fluctuations of magnetic and electric fields in heavy ion collisions. *Phys. Lett. B*, 710:171–174, 2012. doi: 10.1016/j.physletb.2012.02.065.
- [31] Wei-Tian Deng and Xu-Guang Huang. Event-by-event generation of electromagnetic fields in heavy-ion collisions. *Phys. Rev. C*, 85:044907, 2012. doi: 10.1103/PhysRevC.85.044907.
- [32] Kirill Tuchin. Particle production in strong electromagnetic fields in relativistic heavy-ion collisions. *Adv. High Energy Phys.*, 2013:490495, 2013. doi: 10.1155/2013/490495.
- [33] Robert C. Duncan and Christopher Thompson. Formation of very strongly magnetized neutron stars - implications for gamma-ray bursts. *Astrophys. J. Lett.*, 392:L9, 1992. doi: 10.1086/186413.
- [34] Efrain J. Ferrer and Vivian de la Incera. Magnetism in Dense Quark Matter. *Lect. Notes Phys.*, 871:399–432, 2013. doi: 10.1007/978-3-642-37305-3_16.
- [35] Dario Grasso and Hector R. Rubinstein. Magnetic fields in the early universe. *Phys. Rept.*, 348:163–266, 2001. doi: 10.1016/S0370-1573(00)00110-1.
- [36] Kenneth G. Wilson. Confinement of Quarks. *Phys. Rev. D*, 10:2445–2459, 1974. doi: 10.1103/PhysRevD.10.2445.
- [37] M. Creutz. Monte Carlo Study of Quantized SU(2) Gauge Theory. *Phys. Rev. D*, 21:2308–2315, 1980. doi: 10.1103/PhysRevD.21.2308.
- [38] Michael Creutz. *Quarks, gluons and lattices*. Cambridge Monographs on Mathematical Physics. Cambridge Univ. Press, Cambridge, UK, 6 1985. ISBN 978-0-521-31535-7.
- [39] F. Karsch. Lattice QCD at high temperature and density. *Lect. Notes Phys.*, 583:209–249, 2002. doi: 10.1007/3-540-45792-5_6.
- [40] Y. Aoki, G. Endrodi, Z. Fodor, S. D. Katz, and K. K. Szabo. The Order of the

- quantum chromodynamics transition predicted by the standard model of particle physics. *Nature*, 443:675–678, 2006. doi: 10.1038/nature05120.
- [41] Szabolcs Borsanyi, Zoltan Fodor, Christian Hoelbling, Sandor D Katz, Stefan Krieg, Claudia Ratti, and Kalman K. Szabo. Is there still any T_c mystery in lattice QCD? Results with physical masses in the continuum limit III. *JHEP*, 09:073, 2010. doi: 10.1007/JHEP09(2010)073.
- [42] A. Bazavov et al. The chiral and deconfinement aspects of the QCD transition. *Phys. Rev. D*, 85:054503, 2012. doi: 10.1103/PhysRevD.85.054503.
- [43] O. Kaczmarek, F. Karsch, E. Laermann, C. Miao, S. Mukherjee, P. Petreczky, C. Schmidt, W. Soeldner, and W. Unger. Phase boundary for the chiral transition in (2+1) -flavor QCD at small values of the chemical potential. *Phys. Rev. D*, 83:014504, 2011. doi: 10.1103/PhysRevD.83.014504.
- [44] G. Endrodi, Z. Fodor, S. D. Katz, and K. K. Szabo. The QCD phase diagram at nonzero quark density. *JHEP*, 04:001, 2011. doi: 10.1007/JHEP04(2011)001.
- [45] Claudio Bonati, Massimo D’Elia, Marco Mariti, Michele Mesiti, Francesco Negro, and Francesco Sanfilippo. Curvature of the chiral pseudocritical line in QCD: Continuum extrapolated results. *Phys. Rev. D*, 92(5):054503, 2015. doi: 10.1103/PhysRevD.92.054503.
- [46] Paolo Cea, Leonardo Cosmai, and Alessandro Papa. Critical line of 2+1 flavor QCD: Toward the continuum limit. *Phys. Rev. D*, 93(1):014507, 2016. doi: 10.1103/PhysRevD.93.014507.
- [47] Shin Muroya, Atsushi Nakamura, Chiho Nonaka, and Tetsuya Takaishi. Lattice QCD at finite density: An Introductory review. *Prog. Theor. Phys.*, 110:615–668, 2003. doi: 10.1143/PTP.110.615.
- [48] Massimo D’Elia. Lattice QCD Simulations in External Background Fields. *Lect. Notes Phys.*, 871:181–208, 2013. doi: 10.1007/978-3-642-37305-3_7.
- [49] Heng-Tong Ding, Frithjof Karsch, and Swagato Mukherjee. Thermodynamics of strong-interaction matter from Lattice QCD. *Int. J. Mod. Phys. E*, 24(10):1530007, 2015. doi: 10.1142/S0218301315300076.
- [50] S. P. Klevansky. The Nambu-Jona-Lasinio model of quantum chromodynamics. *Rev. Mod. Phys.*, 64:649–708, 1992. doi: 10.1103/RevModPhys.64.649.
- [51] M. Asakawa and K. Yazaki. Chiral Restoration at Finite Density and Temperature. *Nucl. Phys. A*, 504:668–684, 1989. doi: 10.1016/0375-9474(89)90002-X.
- [52] Mikhail A. Stephanov. QCD phase diagram and the critical point. *Prog. Theor. Phys. Suppl.*, 153:139–156, 2004. doi: 10.1142/S0217751X05027965.

-
- [53] M. A. Stephanov. QCD phase diagram: An Overview. *PoS*, LAT2006:024, 2006. doi: 10.22323/1.032.0024.
- [54] Maciej A. Nowak. Lectures on chiral disorder in QCD. In *Cargese Summer School on QCD Perspectives on Hot and Dense Matter*, pages 433–460, 12 2001.
- [55] Stefan Scherer. Introduction to chiral perturbation theory. *Adv. Nucl. Phys.*, 27: 277, 2003.
- [56] Gerard 't Hooft. On the Phase Transition Towards Permanent Quark Confinement. *Nucl. Phys. B*, 138:1–25, 1978. doi: 10.1016/0550-3213(78)90153-0.
- [57] Alexander M. Polyakov. Thermal Properties of Gauge Fields and Quark Liberation. *Phys. Lett. B*, 72:477–480, 1978. doi: 10.1016/0370-2693(78)90737-2.
- [58] Leonard Susskind. Lattice Models of Quark Confinement at High Temperature. *Phys. Rev. D*, 20:2610–2618, 1979. doi: 10.1103/PhysRevD.20.2610.
- [59] Benjamin Svetitsky and Laurence G. Yaffe. Critical Behavior at Finite Temperature Confinement Transitions. *Nucl. Phys. B*, 210:423–447, 1982. doi: 10.1016/0550-3213(82)90172-9.
- [60] Adam Bzdak, Shinichi Esumi, Volker Koch, Jinfeng Liao, Mikhail Stephanov, and Nu Xu. Mapping the Phases of Quantum Chromodynamics with Beam Energy Scan. *Phys. Rept.*, 853:1–87, 2020. doi: 10.1016/j.physrep.2020.01.005.
- [61] Xiaofeng Luo and Nu Xu. Search for the QCD Critical Point with Fluctuations of Conserved Quantities in Relativistic Heavy-Ion Collisions at RHIC : An Overview. *Nucl. Sci. Tech.*, 28(8):112, 2017. doi: 10.1007/s41365-017-0257-0.
- [62] J. J. Binney, N. J. Dowrick, A. J. Fisher, and M. E. J. Newman. *The Theory of critical phenomena: An Introduction to the renormalization group*. 1992.
- [63] Peter Kopietz, Lorenz Bartosch, and Florian Schütz. *Introduction to the functional renormalization group*, volume 798. 2010. doi: 10.1007/978-3-642-05094-7.
- [64] Misha A. Stephanov, K. Rajagopal, and Edward V. Shuryak. Signatures of the tricritical point in QCD. *Phys. Rev. Lett.*, 81:4816–4819, 1998. doi: 10.1103/PhysRevLett.81.4816.
- [65] Misha A. Stephanov, K. Rajagopal, and Edward V. Shuryak. Event-by-event fluctuations in heavy ion collisions and the QCD critical point. *Phys. Rev. D*, 60: 114028, 1999. doi: 10.1103/PhysRevD.60.114028.
- [66] S. Ejiri, F. Karsch, and K. Redlich. Hadronic fluctuations at the QCD phase transition. *Phys. Lett. B*, 633:275–282, 2006. doi: 10.1016/j.physletb.2005.11.083.
- [67] B. Friman, F. Karsch, K. Redlich, and V. Skokov. Fluctuations as probe of the

- QCD phase transition and freeze-out in heavy ion collisions at LHC and RHIC. *Eur. Phys. J. C*, 71:1694, 2011. doi: 10.1140/epjc/s10052-011-1694-2.
- [68] Masayuki Asakawa and Masakiyo Kitazawa. Fluctuations of conserved charges in relativistic heavy ion collisions: An introduction. *Prog. Part. Nucl. Phys.*, 90: 299–342, 2016. doi: 10.1016/j.pnpnp.2016.04.002.
- [69] Gabor Andras Almasi, Bengt Friman, and Krzysztof Redlich. Baryon number fluctuations in chiral effective models and their phenomenological implications. *Phys. Rev. D*, 96(1):014027, 2017. doi: 10.1103/PhysRevD.96.014027.
- [70] Frithjof Karsch. Lattice QCD results on cumulant ratios at freeze-out. *J. Phys. Conf. Ser.*, 779(1):012015, 2017. doi: 10.1088/1742-6596/779/1/012015.
- [71] A. Barducci, R. Casalbuoni, S. De Curtis, Raoul Gatto, and Giulio Pettini. Chiral Symmetry Breaking in QCD at Finite Temperature and Density. *Phys. Lett. B*, 231:463–470, 1989. doi: 10.1016/0370-2693(89)90695-3.
- [72] Frank Wilczek. Application of the renormalization group to a second order QCD phase transition. *Int. J. Mod. Phys. A*, 7:3911–3925, 1992. doi: 10.1142/S0217751X92001757. [Erratum: *Int.J.Mod.Phys.A* 7, 6951 (1992)].
- [73] Adam Miklos Halasz, A. D. Jackson, R. E. Shrock, Misha A. Stephanov, and J. J. M. Verbaarschot. On the phase diagram of QCD. *Phys. Rev. D*, 58:096007, 1998. doi: 10.1103/PhysRevD.58.096007.
- [74] C. Sasaki, B. Friman, and K. Redlich. Density fluctuations in the presence of spinodal instabilities. *Phys. Rev. Lett.*, 99:232301, 2007. doi: 10.1103/PhysRevLett.99.232301.
- [75] Jan Steinheimer and Jorgen Randrup. Spinodal amplification of density fluctuations in fluid-dynamical simulations of relativistic nuclear collisions. *Phys. Rev. Lett.*, 109:212301, 2012. doi: 10.1103/PhysRevLett.109.212301.
- [76] Christoph Herold, Marlene Nahrgang, Igor Mishustin, and Marcus Bleicher. Formation of droplets with high baryon density at the QCD phase transition in expanding matter. *Nucl. Phys. A*, 925:14–24, 2014. doi: 10.1016/j.nuclphysa.2014.01.010.
- [77] Pok Man Lo, Michał Szymański, Krzysztof Redlich, and Chihiro Sasaki. Polyakov loop fluctuations in the presence of external fields. *Phys. Rev. D*, 97(11):114006, 2018. doi: 10.1103/PhysRevD.97.114006.
- [78] Pok Man Lo, Michał Szymański, Chihiro Sasaki, and Krzysztof Redlich. Deconfinement in the presence of a strong magnetic field. *Phys. Rev. D*, 102(3):034024, 2020. doi: 10.1103/PhysRevD.102.034024.
- [79] Pok Man Lo, Michał Szymański, Krzysztof Redlich, and Chihiro Sasaki. Polarization effects at finite temperature and magnetic field. 7 2021.

-
- [80] Pok Man Lo, Michał Szymański, Krzysztof Redlich, and Chihiro Sasaki. Driving chiral phase transition with ring diagram. 9 2021.
- [81] Michał Szymański. Deconfinement of heavy quarks at finite density and strong magnetic field. *Eur. Phys. J. ST*, 229(22-23):3387–3394, 2020. doi: 10.1140/epjst/e2020-000115-3.
- [82] Michał Szymański, Marcus Bluhm, Krzysztof Redlich, and Chihiro Sasaki. Net-proton number fluctuations in the presence of the QCD critical point. *J. Phys. G*, 47(4):045102, 2020. doi: 10.1088/1361-6471/ab614c.
- [83] Chen-Ning Yang and Robert L. Mills. Conservation of Isotopic Spin and Isotopic Gauge Invariance. *Phys. Rev.*, 96:191–195, 1954. doi: 10.1103/PhysRev.96.191.
- [84] Alexandre Deur, Stanley J. Brodsky, and Guy F. de Teramond. The QCD Running Coupling. *Nucl. Phys.*, 90:1, 2016. doi: 10.1016/j.ppnp.2016.04.003.
- [85] Emmy Noether. Invariant Variation Problems. *Gott. Nachr.*, 1918:235–257, 1918. doi: 10.1080/00411457108231446.
- [86] Krzysztof A. Meissner. *Klasyczna Teoria Pola*. Wydawnictwo naukowe PWN, Warszawa, 2002. ISBN 83-01-13717-7.
- [87] Sidney Coleman. The invariance of the vacuum is the invariance of the world. *Journal of Mathematical Physics*, 7(5):787–787, 1966. doi: 10.1063/1.1931207. URL <https://doi.org/10.1063/1.1931207>.
- [88] Yoichiro Nambu. Axial vector current conservation in weak interactions. *Phys. Rev. Lett.*, 4:380–382, 1960. doi: 10.1103/PhysRevLett.4.380.
- [89] Yoichiro Nambu and G. Jona-Lasinio. Dynamical Model of Elementary Particles Based on an Analogy with Superconductivity. 1. *Phys. Rev.*, 122:345–358, 1961. doi: 10.1103/PhysRev.122.345.
- [90] Yoichiro Nambu and G. Jona-Lasinio. DYNAMICAL MODEL OF ELEMENTARY PARTICLES BASED ON AN ANALOGY WITH SUPERCONDUCTIVITY. II. *Phys. Rev.*, 124:246–254, 1961. doi: 10.1103/PhysRev.124.246.
- [91] J. Goldstone. Field Theories with Superconductor Solutions. *Nuovo Cim.*, 19: 154–164, 1961. doi: 10.1007/BF02812722.
- [92] Jeffrey Goldstone, Abdus Salam, and Steven Weinberg. Broken Symmetries. *Phys. Rev.*, 127:965–970, 1962. doi: 10.1103/PhysRev.127.965.
- [93] Murray Gell-Mann and M Levy. The axial vector current in beta decay. *Nuovo Cim.*, 16:705, 1960. doi: 10.1007/BF02859738.
- [94] Volker Koch. Aspects of chiral symmetry. *Int. J. Mod. Phys. E*, 6:203–250, 1997. doi: 10.1142/S0218301397000147.

- [95] Andrei V. Smilga. *Lectures on quantum chromodynamics*. WSP, Singapore, 2001. doi: 10.1142/4443.
- [96] Thomas Mannel. Theory and phenomenology of CP violation. *Nucl. Phys. B Proc. Suppl.*, 167:115–119, 2007. doi: 10.1016/j.nuclphysbps.2006.12.083.
- [97] Stephen L. Adler. Axial vector vertex in spinor electrodynamics. *Phys. Rev.*, 177:2426–2438, 1969. doi: 10.1103/PhysRev.177.2426.
- [98] J. S. Bell and R. Jackiw. A PCAC puzzle: $\pi^0 \rightarrow \gamma\gamma$ in the σ model. *Nuovo Cim. A*, 60:47–61, 1969. doi: 10.1007/BF02823296.
- [99] C. Vafa and Edward Witten. Restrictions on Symmetry Breaking in Vector-Like Gauge Theories. *Nucl. Phys. B*, 234:173–188, 1984. doi: 10.1016/0550-3213(84)90230-X.
- [100] Murray Gell-Mann. Symmetries of baryons and mesons. *Phys. Rev.*, 125:1067–1084, 1962. doi: 10.1103/PhysRev.125.1067.
- [101] Yuval Ne’eman. Derivation of strong interactions from a gauge invariance. *Nucl. Phys.*, 26:222–229, 1961. doi: 10.1016/0029-5582(61)90134-1.
- [102] Murray Gell-Mann. A Schematic Model of Baryons and Mesons. *Phys. Lett.*, 8:214–215, 1964. doi: 10.1016/S0031-9163(64)92001-3.
- [103] Aneesh Manohar and Howard Georgi. Chiral Quarks and the Nonrelativistic Quark Model. *Nucl. Phys. B*, 234:189–212, 1984. doi: 10.1016/0550-3213(84)90231-1.
- [104] H. Sazdjian. Introduction to chiral symmetry in QCD. *EPJ Web Conf.*, 137:02001, 2017. doi: 10.1051/epjconf/201713702001.
- [105] J. Greensite. The Confinement problem in lattice gauge theory. *Prog. Part. Nucl. Phys.*, 51:1, 2003. doi: 10.1016/S0146-6410(03)90012-3.
- [106] Jeff Greensite. *An introduction to the confinement problem*, volume 821. 2011. doi: 10.1007/978-3-642-14382-3.
- [107] G. F. Chew and Steven C. Frautschi. Regge Trajectories and the Principle of Maximum Strength for Strong Interactions. *Phys. Rev. Lett.*, 8:41–44, 1962. doi: 10.1103/PhysRevLett.8.41.
- [108] Bernhard Ketzer, Boris Grube, and Dmitry Ryabchikov. Light-Meson Spectroscopy with COMPASS. 9 2019. doi: 10.1016/j.pnpnp.2020.103755.
- [109] Yoichiro Nambu. QCD and the String Model. *Phys. Lett. B*, 80:372–376, 1979. doi: 10.1016/0370-2693(79)91193-6.
- [110] Stephen Gasiorowicz and Jonathan L. Rosner. Hadron Spectra and Quarks. *Am. J. Phys.*, 49:954, 1981. doi: 10.1119/1.12597.

-
- [111] E. Seiler. Upper Bound on the Color Confining Potential. *Phys. Rev. D*, 18:482–483, 1978. doi: 10.1103/PhysRevD.18.482.
- [112] Myron Bander. Theories of Quark Confinement. *Phys. Rept.*, 75:205, 1981. doi: 10.1016/0370-1573(81)90026-0.
- [113] G. S. Bali and K. Schilling. Static quark - anti-quark potential: Scaling behavior and finite size effects in SU(3) lattice gauge theory. *Phys. Rev. D*, 46:2636–2646, 1992. doi: 10.1103/PhysRevD.46.2636.
- [114] S. P. Booth, D. S. Henty, A. Hulsebos, A. C. Irving, Christopher Michael, and P. W. Stephenson. The Running coupling from SU(3) lattice gauge theory. *Phys. Lett. B*, 294:385–390, 1992. doi: 10.1016/0370-2693(92)91538-K.
- [115] Gunnar S. Bali. QCD forces and heavy quark bound states. *Phys. Rept.*, 343: 1–136, 2001. doi: 10.1016/S0370-1573(00)00079-X.
- [116] G. S. Bali, K. Schilling, and C. Schlichter. Observing long color flux tubes in SU(2) lattice gauge theory. *Phys. Rev. D*, 51:5165–5198, 1995. doi: 10.1103/PhysRevD.51.5165.
- [117] F. Bissey, F-G. Cao, A. R. Kitson, A. I. Signal, D. B. Leinweber, B. G. Lasscock, and A. G. Williams. Gluon flux-tube distribution and linear confinement in baryons. *Phys. Rev. D*, 76:114512, 2007. doi: 10.1103/PhysRevD.76.114512.
- [118] Gunnar S. Bali, Hartmut Neff, Thomas Duessel, Thomas Lippert, and Klaus Schilling. Observation of string breaking in QCD. *Phys. Rev. D*, 71:114513, 2005. doi: 10.1103/PhysRevD.71.114513.
- [119] Owe Philipsen and Hartmut Wittig. String breaking in nonAbelian gauge theories with fundamental matter fields. *Phys. Rev. Lett.*, 81:4056–4059, 1998. doi: 10.1103/PhysRevLett.81.4056. [Erratum: *Phys.Rev.Lett.* 83, 2684 (1999)].
- [120] John Bulava, Ben Hörz, Francesco Knechtli, Vanessa Koch, Graham Moir, Colin Morningstar, and Mike Peardon. String breaking by light and strange quarks in QCD. *Phys. Lett. B*, 793:493–498, 2019. doi: 10.1016/j.physletb.2019.05.018.
- [121] I. T. Drummond. Strong coupling model for string breaking on the lattice. *Phys. Lett. B*, 434:92–98, 1998. doi: 10.1016/S0370-2693(98)00747-3.
- [122] Francesco Knechtli and Rainer Sommer. String breaking as a mixing phenomenon in the SU(2) Higgs model. *Nucl. Phys. B*, 590:309–328, 2000. doi: 10.1016/S0550-3213(00)00470-3.
- [123] Eric S. Swanson. Aspects of confinement: A Brief review. *AIP Conf. Proc.*, 717 (1):636–645, 2004. doi: 10.1063/1.1799773.
- [124] Shang-Keng Ma. *Statistical Mechanics*. WORLD SCIENTIFIC, 1985. doi: 10.1142/0073. URL <https://www.worldscientific.com/doi/abs/10.1142/0073>.

- [125] Leo P. Kadanoff. More is the Same: Phase Transitions and Mean Field Theories. *J. Statist. Phys.*, 137:777, 2009. doi: 10.1007/s10955-009-9814-1.
- [126] Kerson Huang. *Statistical Mechanics*. John Wiley & Sons, 2 edition, 1987.
- [127] L. D. Landau. On the theory of phase transitions. *Zh. Eksp. Teor. Fiz.*, 7:19–32, 1937.
- [128] A.L. Fetter and J.D. Walecka. *Quantum Theory of Many-particle Systems*. Dover Books on Physics. Dover Publications, 2003. ISBN 9780486428277. URL <https://books.google.pl/books?id=0wekf1s83b0C>.
- [129] J. I. Kapusta and Charles Gale. *Finite-temperature field theory: Principles and applications*. Cambridge Monographs on Mathematical Physics. Cambridge University Press, 2011. ISBN 978-0-521-17322-3, 978-0-521-82082-0, 978-0-511-22280-1. doi: 10.1017/CBO9780511535130.
- [130] B. Widom. Surface tension and molecular correlations near the critical point. *The Journal of Chemical Physics*, 43(11):3892–3897, 1965. doi: 10.1063/1.1696617. URL <https://doi.org/10.1063/1.1696617>.
- [131] L. P. Kadanoff. Scaling laws for Ising models near $T(c)$. *Physics Physique Fizika*, 2:263–272, 1966. doi: 10.1103/PhysicsPhysiqueFizika.2.263.
- [132] K Binder. Theory of first-order phase transitions. *Reports on Progress in Physics*, 50(7):783–859, jul 1987. doi: 10.1088/0034-4885/50/7/001. URL <https://doi.org/10.1088/0034-4885/50/7/001>.
- [133] Michel Le Bellac. *Thermal Field Theory*. Cambridge Monographs on Mathematical Physics. Cambridge University Press, 3 2011. ISBN 978-0-511-88506-8, 978-0-521-65477-7. doi: 10.1017/CBO9780511721700.
- [134] Mikko Laine and Aleksi Vuorinen. *Basics of Thermal Field Theory*, volume 925. Springer, 2016. doi: 10.1007/978-3-319-31933-9.
- [135] Kieran Holland and Uwe-Jens Wiese. The Center symmetry and its spontaneous breakdown at high temperatures. pages 1909–1944, 11 2000. doi: 10.1142/9789812810458_0040.
- [136] Gerard 't Hooft. A Property of Electric and Magnetic Flux in Nonabelian Gauge Theories. *Nucl. Phys. B*, 153:141–160, 1979. doi: 10.1016/0550-3213(79)90595-9.
- [137] Larry D. McLerran and Benjamin Svetitsky. Quark Liberation at High Temperature: A Monte Carlo Study of $SU(2)$ Gauge Theory. *Phys. Rev. D*, 24:450, 1981. doi: 10.1103/PhysRevD.24.450.
- [138] Sudhir Nadkarni. Nonabelian Debye Screening. 1. The Color Averaged Potential. *Phys. Rev. D*, 33:3738, 1986. doi: 10.1103/PhysRevD.33.3738.

-
- [139] Pok Man Lo, Bengt Friman, Olaf Kaczmarek, Krzysztof Redlich, and Chihiro Sasaki. Probing Deconfinement with Polyakov Loop Susceptibilities. *Phys. Rev. D*, 88(1):014506, 2013. doi: 10.1103/PhysRevD.88.014506.
- [140] A. Bazavov, N. Brambilla, H. T. Ding, P. Petreczky, H. P. Schadler, A. Vairo, and J. H. Weber. Polyakov loop in 2+1 flavor QCD from low to high temperatures. *Phys. Rev. D*, 93(11):114502, 2016. doi: 10.1103/PhysRevD.93.114502.
- [141] Pok Man Lo, Bengt Friman, Olaf Kaczmarek, Krzysztof Redlich, and Chihiro Sasaki. Polyakov loop fluctuations in SU(3) lattice gauge theory and an effective gluon potential. *Phys. Rev. D*, 88:074502, 2013. doi: 10.1103/PhysRevD.88.074502.
- [142] Frank R. Brown, Frank P. Butler, Hong Chen, Norman H. Christ, Zhi-hua Dong, Wendy Schaffer, Leo I. Unger, and Alessandro Vaccarino. On the existence of a phase transition for QCD with three light quarks. *Phys. Rev. Lett.*, 65:2491–2494, 1990. doi: 10.1103/PhysRevLett.65.2491.
- [143] Andrei V. Smilga. Physics of thermal QCD. *Phys. Rept.*, 291:1–106, 1997. doi: 10.1016/S0370-1573(97)00014-8.
- [144] Robert D. Pisarski. Notes on the deconfining phase transition. In *Cargese Summer School on QCD Perspectives on Hot and Dense Matter*, pages 353–384, 3 2002.
- [145] R. B. Potts. Some generalized order - disorder transformations. *Proc. Cambridge Phil. Soc.*, 48:106–109, 1952. doi: 10.1017/S0305004100027419.
- [146] F. Y. Wu. The Potts model. *Rev. Mod. Phys.*, 54:235–268, 1982. doi: 10.1103/RevModPhys.54.235. [Erratum: *Rev. Mod. Phys.* 55, 315–315 (1983)].
- [147] Larry D. McLerran and Benjamin Svetitsky. A Monte Carlo Study of SU(2) Yang-Mills Theory at Finite Temperature. *Phys. Lett. B*, 98:195, 1981. doi: 10.1016/0370-2693(81)90986-2.
- [148] J. Engels, J. Fingberg, and M. Weber. Finite Size Scaling Analysis of SU(2) Lattice Gauge Theory in (3+1)-dimensions. *Nucl. Phys. B*, 332:737–759, 1990. doi: 10.1016/0550-3213(90)90010-B.
- [149] T. Celik, J. Engels, and H. Satz. The Order of the Deconfinement Transition in SU(3) Yang-Mills Theory. *Phys. Lett. B*, 125:411–414, 1983. doi: 10.1016/0370-2693(83)91314-X.
- [150] John B. Kogut, M. Stone, H. W. Wyld, W. R. Gibbs, J. Shigemitsu, Stephen H. Shenker, and D. K. Sinclair. Deconfinement and Chiral Symmetry Restoration at Finite Temperatures in SU(2) and SU(3) Gauge Theories. *Phys. Rev. Lett.*, 50:393, 1983. doi: 10.1103/PhysRevLett.50.393.
- [151] G. Boyd, J. Engels, F. Karsch, E. Laermann, C. Legeland, M. Lutgemeier, and

- B. Petersson. Equation of state for the SU(3) gauge theory. *Phys. Rev. Lett.*, 75: 4169–4172, 1995. doi: 10.1103/PhysRevLett.75.4169.
- [152] Pok Man Lo. Probing Deconfinement with Polyakov Loop Susceptibilities. *Acta Phys. Polon. Suppl.*, 7(1):99–105, 2014. doi: 10.5506/APhysPolBSupp.7.99.
- [153] Philippe de Forcrand and Massimo D’Elia. Continuum limit and universality of the Columbia plot. *PoS, LATTICE2016:081*, 2017. doi: 10.22323/1.256.0081.
- [154] Kenji Fukushima and Vladimir Skokov. Polyakov loop modeling for hot QCD. *Prog. Part. Nucl. Phys.*, 96:154–199, 2017. doi: 10.1016/j.pnpnp.2017.05.002.
- [155] Claudia Ratti, Michael A. Thaler, and Wolfram Weise. Phases of QCD: Lattice thermodynamics and a field theoretical model. *Phys. Rev. D*, 73:014019, 2006. doi: 10.1103/PhysRevD.73.014019.
- [156] Simon Roessner, Claudia Ratti, and W. Weise. Polyakov loop, diquarks and the two-flavour phase diagram. *Phys. Rev. D*, 75:034007, 2007. doi: 10.1103/PhysRevD.75.034007.
- [157] Kenji Fukushima. Chiral effective model with the Polyakov loop. *Phys. Lett. B*, 591:277–284, 2004. doi: 10.1016/j.physletb.2004.04.027.
- [158] C. Sasaki, B. Friman, and K. Redlich. Susceptibilities and the Phase Structure of a Chiral Model with Polyakov Loops. *Phys. Rev. D*, 75:074013, 2007. doi: 10.1103/PhysRevD.75.074013.
- [159] Robert D. Pisarski and Frank Wilczek. Remarks on the Chiral Phase Transition in Chromodynamics. *Phys. Rev. D*, 29:338–341, 1984. doi: 10.1103/PhysRevD.29.338.
- [160] M. Kobayashi and T. Maskawa. Chiral symmetry and eta-x mixing. *Prog. Theor. Phys.*, 44:1422–1424, 1970. doi: 10.1143/PTP.44.1422.
- [161] M. Kobayashi, H. Kondo, and T. Maskawa. Symmetry breaking of the chiral $u(3) \times u(3)$ and the quark model. *Prog. Theor. Phys.*, 45:1955–1959, 1971. doi: 10.1143/PTP.45.1955.
- [162] Gerard ’t Hooft. Symmetry Breaking Through Bell-Jackiw Anomalies. *Phys. Rev. Lett.*, 37:8–11, 1976. doi: 10.1103/PhysRevLett.37.8.
- [163] Gerard ’t Hooft. Computation of the Quantum Effects Due to a Four-Dimensional Pseudoparticle. *Phys. Rev. D*, 14:3432–3450, 1976. doi: 10.1103/PhysRevD.14.3432. [Erratum: *Phys.Rev.D* 18, 2199 (1978)].
- [164] Szabolcs Borsanyi, Zoltan Fodor, Jana N. Guenther, Ruben Kara, Sandor D. Katz, Paolo Parotto, Attila Pasztor, Claudia Ratti, and Kalman K. Szabo. QCD Crossover at Finite Chemical Potential from Lattice Simulations. *Phys. Rev. Lett.*, 125(5):052001, 2020. doi: 10.1103/PhysRevLett.125.052001.

-
- [165] C. R. Allton, S. Ejiri, S. J. Hands, O. Kaczmarek, F. Karsch, E. Laermann, C. Schmidt, and L. Scorzato. The QCD thermal phase transition in the presence of a small chemical potential. *Phys. Rev. D*, 66:074507, 2002. doi: 10.1103/PhysRevD.66.074507.
- [166] Maria-Paola Lombardo. Finite density (might well be easier) at finite temperature. *Nucl. Phys. B Proc. Suppl.*, 83:375–377, 2000. doi: 10.1016/S0920-5632(00)91678-5.
- [167] Philippe de Forcrand and Owe Philipsen. The QCD phase diagram for small densities from imaginary chemical potential. *Nucl. Phys. B*, 642:290–306, 2002. doi: 10.1016/S0550-3213(02)00626-0.
- [168] G. Sauer, H. Chandra, and U. Mosel. Thermal properties of nuclei. *Nucl. Phys. A*, 264:221–243, 1976. doi: 10.1016/0375-9474(76)90429-2.
- [169] J. Pochodzalla et al. Probing the nuclear liquid - gas phase transition. *Phys. Rev. Lett.*, 75:1040–1043, 1995. doi: 10.1103/PhysRevLett.75.1040.
- [170] J. B. Elliott, P. T. Lake, L. G. Moretto, and L. Phair. Determination of the coexistence curve, critical temperature, density, and pressure of bulk nuclear matter from fragment emission data. *Phys. Rev. C*, 87(5):054622, 2013. doi: 10.1103/PhysRevC.87.054622.
- [171] Leon N. Cooper. Bound electron pairs in a degenerate Fermi gas. *Phys. Rev.*, 104:1189–1190, 1956. doi: 10.1103/PhysRev.104.1189.
- [172] John Bardeen, L. N. Cooper, and J. R. Schrieffer. Microscopic theory of superconductivity. *Phys. Rev.*, 106:162, 1957. doi: 10.1103/PhysRev.106.162.
- [173] John Bardeen, L. N. Cooper, and J. R. Schrieffer. Theory of superconductivity. *Phys. Rev.*, 108:1175–1204, 1957. doi: 10.1103/PhysRev.108.1175.
- [174] Mark G. Alford, Krishna Rajagopal, and Frank Wilczek. Color flavor locking and chiral symmetry breaking in high density QCD. *Nucl. Phys. B*, 537:443–458, 1999. doi: 10.1016/S0550-3213(98)00668-3.
- [175] Thomas Schäfer and Frank Wilczek. Continuity of quark and hadron matter. *Phys. Rev. Lett.*, 82:3956–3959, 1999. doi: 10.1103/PhysRevLett.82.3956.
- [176] Krishna Rajagopal and Frank Wilczek. *The Condensed matter physics of QCD*, pages 2061–2151. 11 2000. doi: 10.1142/9789812810458_0043.
- [177] Mark G. Alford, Andreas Schmitt, Krishna Rajagopal, and Thomas Schäfer. Color superconductivity in dense quark matter. *Rev. Mod. Phys.*, 80:1455–1515, 2008. doi: 10.1103/RevModPhys.80.1455.
- [178] O. Kaczmarek, F. Karsch, P. Petreczky, and F. Zantow. Heavy quark anti-quark free energy and the renormalized Polyakov loop. *Phys. Lett. B*, 543:41–47, 2002. doi: 10.1016/S0370-2693(02)02415-2.

- [179] Johannes Heinrich Weber. Lattice calculation of the Polyakov loop and Polyakov loop correlators. *EPJ Web Conf.*, 137:07028, 2017. doi: 10.1051/epjconf/201713707028.
- [180] Y. Aoki, Szabolcs Borsanyi, Stephan Durr, Zoltan Fodor, Sandor D. Katz, Stefan Krieg, and Kalman K. Szabo. The QCD transition temperature: results with physical masses in the continuum limit II. *JHEP*, 06:088, 2009. doi: 10.1088/1126-6708/2009/06/088.
- [181] Y. Aoki, S. Borsanyi, S. Durr, Z. Fodor, S. D. Katz, S. Krieg, and K. K. Szabo. QCD transition temperature: Approaching the continuum on the lattice. *Nucl. Phys. A*, 830:805C–808C, 2009. doi: 10.1016/j.nuclphysa.2009.10.141.
- [182] K. Kajantie, M. Laine, K. Rummukainen, and Mikhail E. Shaposhnikov. 3-D SU(N) + adjoint Higgs theory and finite temperature QCD. *Nucl. Phys. B*, 503:357–384, 1997. doi: 10.1016/S0550-3213(97)00425-2.
- [183] Peter Brockway Arnold and Laurence G. Yaffe. The NonAbelian Debye screening length beyond leading order. *Phys. Rev. D*, 52:7208–7219, 1995. doi: 10.1103/PhysRevD.52.7208.
- [184] Adrian Dumitru and Robert D. Pisarski. Two point functions for SU(3) Polyakov loops near T(c). *Phys. Rev. D*, 66:096003, 2002. doi: 10.1103/PhysRevD.66.096003.
- [185] David E. Miller and Krzysztof Redlich. Thermodynamical Properties of a Class of Models With Nonabelian Internal Symmetries at Finite Temperature and Baryon Number. *Phys. Rev. D*, 37:3716, 1988. doi: 10.1103/PhysRevD.37.3716.
- [186] E. Megias, E. Ruiz Arriola, and L. L. Salcedo. Polyakov loop in chiral quark models at finite temperature. *Phys. Rev. D*, 74:065005, 2006. doi: 10.1103/PhysRevD.74.065005.
- [187] Pok Man Lo, Bengt Friman, and Krzysztof Redlich. Polyakov loop fluctuations and deconfinement in the limit of heavy quarks. *Phys. Rev. D*, 90(7):074035, 2014. doi: 10.1103/PhysRevD.90.074035.
- [188] Peter Kovács, Zsolt Szép, and György Wolf. Existence of the critical endpoint in the vector meson extended linear sigma model. *Phys. Rev. D*, 93(11):114014, 2016. doi: 10.1103/PhysRevD.93.114014.
- [189] Kouji Kashiwa, Robert D. Pisarski, and Vladimir V. Skokov. Critical endpoint for deconfinement in matrix and other effective models. *Phys. Rev. D*, 85:114029, 2012. doi: 10.1103/PhysRevD.85.114029.
- [190] Constantia Alexandrou, Artan Borici, Alessandra Feo, Philippe de Forcrand, Andrea Galli, Fred Jegerlehner, and Tetsuya Takaishi. The Deconfinement phase transition in one flavor QCD. *Phys. Rev. D*, 60:034504, 1999. doi: 10.1103/PhysRevD.60.034504.

-
- [191] Michael Fromm, Jens Langelage, Stefano Lottini, Mathias Neuman, and Owe Philipsen. Onset Transition to Cold Nuclear Matter from Lattice QCD with Heavy Quarks. *Phys. Rev. Lett.*, 110(12):122001, 2013. doi: 10.1103/PhysRevLett.110.122001.
- [192] Christian S. Fischer, Jan Luecker, and Jan M. Pawłowski. Phase structure of QCD for heavy quarks. *Phys. Rev. D*, 91(1):014024, 2015. doi: 10.1103/PhysRevD.91.014024.
- [193] Owe Philipsen. Towards a theoretical description of dense QCD. *EPJ Web Conf.*, 137:03016, 2017. doi: 10.1051/epjconf/201713703016.
- [194] P. Rehberg, S. P. Klevansky, and J. Hufner. Hadronization in the SU(3) Nambu-Jona-Lasinio model. *Phys. Rev. C*, 53:410–429, 1996. doi: 10.1103/PhysRevC.53.410.
- [195] Tetsuo Hatsuda and Teiji Kunihiro. QCD phenomenology based on a chiral effective Lagrangian. *Phys. Rept.*, 247:221–367, 1994. doi: 10.1016/0370-1573(94)90022-1.
- [196] Robert D. Pisarski and Vladimir V. Skokov. Chiral matrix model of the semi-QGP in QCD. *Phys. Rev. D*, 94(3):034015, 2016. doi: 10.1103/PhysRevD.94.034015.
- [197] Massimo D’Elia and Francesco Negro. Chiral Properties of Strong Interactions in a Magnetic Background. *Phys. Rev. D*, 83:114028, 2011. doi: 10.1103/PhysRevD.83.114028.
- [198] G. S. Bali, F. Bruckmann, G. Endrodi, Z. Fodor, S. D. Katz, and A. Schafer. QCD quark condensate in external magnetic fields. *Phys. Rev. D*, 86:071502, 2012. doi: 10.1103/PhysRevD.86.071502.
- [199] Falk Bruckmann, Gergely Endrodi, and Tamas G. Kovacs. Inverse magnetic catalysis and the Polyakov loop. *JHEP*, 04:112, 2013. doi: 10.1007/JHEP04(2013)112.
- [200] V. G. Bornyakov, P. V. Buividovich, N. Cundy, O. A. Kochetkov, and A. Schäfer. Deconfinement transition in two-flavor lattice QCD with dynamical overlap fermions in an external magnetic field. *Phys. Rev. D*, 90(3):034501, 2014. doi: 10.1103/PhysRevD.90.034501.
- [201] G. S. Bali, F. Bruckmann, G. Endrodi, Z. Fodor, S. D. Katz, S. Krieg, A. Schafer, and K. K. Szabo. The QCD phase diagram for external magnetic fields. *JHEP*, 02:044, 2012. doi: 10.1007/JHEP02(2012)044.
- [202] Gergely Endrodi. Critical point in the QCD phase diagram for extremely strong background magnetic fields. *JHEP*, 07:173, 2015. doi: 10.1007/JHEP07(2015)173.
- [203] Massimo D’Elia, Floriano Manigrasso, Francesco Negro, and Francesco Sanfilippo. QCD phase diagram in a magnetic background for different values of the pion mass. *Phys. Rev. D*, 98(5):054509, 2018. doi: 10.1103/PhysRevD.98.054509.

- [204] Gergely Endrodi, Matteo Giordano, Sandor D. Katz, T. G. Kovács, and Ferenc Pittler. Magnetic catalysis and inverse catalysis for heavy pions. *JHEP*, 07:007, 2019. doi: 10.1007/JHEP07(2019)007.
- [205] Eduardo S. Fraga. Thermal chiral and deconfining transitions in the presence of a magnetic background. *Lect. Notes Phys.*, 871:121–141, 2013. doi: 10.1007/978-3-642-37305-3_5.
- [206] E. S. Fraga, B. W. Mintz, and J. Schaffner-Bielich. A search for inverse magnetic catalysis in thermal quark-meson models. *Phys. Lett. B*, 731:154–158, 2014. doi: 10.1016/j.physletb.2014.02.028.
- [207] R. L. S. Farias, K. P. Gomes, G. I. Krein, and M. B. Pinto. Importance of asymptotic freedom for the pseudocritical temperature in magnetized quark matter. *Phys. Rev. C*, 90(2):025203, 2014. doi: 10.1103/PhysRevC.90.025203.
- [208] E. J. Ferrer, V. de la Incera, and X. J. Wen. Quark Antiscreening at Strong Magnetic Field and Inverse Magnetic Catalysis. *Phys. Rev. D*, 91(5):054006, 2015. doi: 10.1103/PhysRevD.91.054006.
- [209] V. P. Pagura, D. Gomez Dumm, S. Noguera, and N. N. Scoccola. Magnetic catalysis and inverse magnetic catalysis in nonlocal chiral quark models. *Phys. Rev. D*, 95(3):034013, 2017. doi: 10.1103/PhysRevD.95.034013.
- [210] D. Gómez Dumm, M. F. Izzo Villafañe, S. Noguera, V. Pagura, and N. N. Scoccola. Effects of strong magnetic fields on quark matter and π^0 properties within nonlocal chiral quark models. In *14th International Workshop on Hadron Physics*, 5 2018.
- [211] D. Gómez Dumm, M. F. Izzo Villafañe, and N. N. Scoccola. Neutral meson properties under an external magnetic field in nonlocal chiral quark models. *Phys. Rev. D*, 97(3):034025, 2018. doi: 10.1103/PhysRevD.97.034025.
- [212] Jens Braun, Holger Gies, and Jan M. Pawłowski. Quark Confinement from Color Confinement. *Phys. Lett. B*, 684:262–267, 2010. doi: 10.1016/j.physletb.2010.01.009.
- [213] Bernd-Jochen Schaefer, Jan M. Pawłowski, and Jochen Wambach. The Phase Structure of the Polyakov–Quark–Meson Model. *Phys. Rev. D*, 76:074023, 2007. doi: 10.1103/PhysRevD.76.074023.
- [214] U. Reinosa, J. Serreau, M. Tissier, and N. Wschebor. Deconfinement transition in $SU(N)$ theories from perturbation theory. *Phys. Lett. B*, 742:61–68, 2015. doi: 10.1016/j.physletb.2015.01.006.
- [215] Urko Reinosa, Julien Serreau, and Matthieu Tissier. Perturbative study of the QCD phase diagram for heavy quarks at nonzero chemical potential. *Phys. Rev. D*, 92:025021, 2015. doi: 10.1103/PhysRevD.92.025021.

-
- [216] Kenji Fukushima and Kouji Kashiwa. Polyakov loop and QCD thermodynamics from the gluon and ghost propagators. *Phys. Lett. B*, 723:360–364, 2013. doi: 10.1016/j.physletb.2013.05.037.
- [217] Claudio Bonati, Massimo D’Elia, and Andrea Rucci. Heavy quarkonia in strong magnetic fields. *Phys. Rev. D*, 92(5):054014, 2015. doi: 10.1103/PhysRevD.92.054014.
- [218] Claudio Bonati, Massimo D’Elia, Marco Mariti, Michele Mesiti, Francesco Negro, Andrea Rucci, and Francesco Sanfilippo. Screening masses in strong external magnetic fields. *Phys. Rev. D*, 95(7):074515, 2017. doi: 10.1103/PhysRevD.95.074515.
- [219] Olaf Kaczmarek and Felix Zantow. Static quark anti-quark interactions at zero and finite temperature QCD. II. Quark anti-quark internal energy and entropy. 6 2005.
- [220] Kouji Kashiwa and Robert D. Pisarski. Roberge-Weiss transition and ’t Hooft loops. *Phys. Rev. D*, 87(9):096009, 2013. doi: 10.1103/PhysRevD.87.096009.
- [221] H. Saito, S. Ejiri, S. Aoki, T. Hatsuda, K. Kanaya, Y. Maezawa, H. Ohno, and T. Umeda. Phase structure of finite temperature QCD in the heavy quark region. *Phys. Rev. D*, 84:054502, 2011. doi: 10.1103/PhysRevD.85.079902. [Erratum: Phys.Rev.D 85, 079902 (2012)].
- [222] Michael Fromm, Jens Langelage, Stefano Lottini, and Owe Philipsen. The QCD deconfinement transition for heavy quarks and all baryon chemical potentials. *JHEP*, 01:042, 2012. doi: 10.1007/JHEP01(2012)042.
- [223] Shinji Ejiri, Shota Itagaki, Ryo Iwami, Kazuyuki Kanaya, Masakiyo Kitazawa, Atsushi Kiyohara, Mizuki Shirogane, and Takashi Umeda. End point of the first-order phase transition of QCD in the heavy quark region by reweighting from quenched QCD. *Phys. Rev. D*, 101(5):054505, 2020. doi: 10.1103/PhysRevD.101.054505.
- [224] Jorn K. Boomsma and Daniel Boer. The Influence of strong magnetic fields and instantons on the phase structure of the two-flavor NJL model. *Phys. Rev. D*, 81:074005, 2010. doi: 10.1103/PhysRevD.81.074005.
- [225] Murray Gell-Mann and Keith A. Brueckner. Correlation Energy of an Electron Gas at High Density. *Phys. Rev.*, 106:364–368, 1957. doi: 10.1103/PhysRev.106.364.
- [226] David Bohm and David Pines. A Collective Description of Electron Interactions: 3. Coulomb Interactions in a Degenerate Electron Gas. *Phys. Rev.*, 92:609–625, 1953. doi: 10.1103/PhysRev.92.609.
- [227] J. Govaerts, J. E. Mandula, and J. Weyers. A Model for Chiral Symmetry Breaking in QCD. *Nucl. Phys. B*, 237:59–76, 1984. doi: 10.1016/0550-3213(84)90015-4.

- [228] Aleksandar Kocic. Chiral Symmetry Restoration at Finite Densities in Coulomb Gauge QCD. *Phys. Rev. D*, 33:1785, 1986. doi: 10.1103/PhysRevD.33.1785.
- [229] M. Hirata. Composite Meson Quark Interactions Under the Condition of Dynamical Breaking of Chiral Symmetry. *Phys. Rev. D*, 39:1425–1431, 1989. doi: 10.1103/PhysRevD.39.1425.
- [230] Reinhard Alkofer, P. A. Amundsen, and K. Langfeld. Chiral Symmetry Breaking and Pion Properties at Finite Temperatures. *Z. Phys. C*, 42:199–208, 1989. doi: 10.1007/BF01555857.
- [231] S. M. Schmidt, D. Blaschke, and Yu. L. Kalinovsky. Low-energy theorems in a nonlocal chiral quark model at finite temperature. *Z. Phys. C*, 66:485–490, 1995. doi: 10.1007/BF01556375.
- [232] H. Reinhardt, G. Burgio, D. Campagnari, E. Ebadati, J. Heffner, M. Quandt, P. Vastag, and H. Vogt. Hamiltonian approach to QCD in Coulomb gauge - a survey of recent results. *Adv. High Energy Phys.*, 2018:2312498, 2018. doi: 10.1155/2018/2312498.
- [233] Markus Quandt, Ehsan Ebadati, Hugo Reinhardt, and Peter Vastag. Chiral symmetry restoration at finite temperature within the Hamiltonian approach to QCD in Coulomb gauge. *Phys. Rev. D*, 98(3):034012, 2018. doi: 10.1103/PhysRevD.98.034012.
- [234] Pok Man Lo and Eric S. Swanson. Confinement Models at Finite Temperature and Density. *Phys. Rev. D*, 81:034030, 2010. doi: 10.1103/PhysRevD.81.034030.
- [235] R. D. Mattuck. *A Guide to Feynman Diagrams in the Many Body Problem (Second Edition)*. 1976.
- [236] Gianluca Stefanucci and Robert van Leeuwen. *Nonequilibrium Many-Body Theory of Quantum Systems: A Modern Introduction*. Cambridge University Press, 2013. doi: 10.1017/CBO9781139023979.
- [237] Gergely Endrődi and Gergely Markó. Magnetized baryons and the QCD phase diagram: NJL model meets the lattice. *JHEP*, 08:036, 2019. doi: 10.1007/JHEP08(2019)036.
- [238] V. Skokov, B. Stokic, B. Friman, and K. Redlich. Meson fluctuations and thermodynamics of the Polyakov loop extended quark-meson model. *Phys. Rev. C*, 82:015206, 2010. doi: 10.1103/PhysRevC.82.015206.
- [239] V. Skokov, B. Friman, and K. Redlich. Quark number fluctuations in the Polyakov loop-extended quark-meson model at finite baryon density. *Phys. Rev. C*, 83:054904, 2011. doi: 10.1103/PhysRevC.83.054904.
- [240] Pok Man Lo, Krzysztof Redlich, and Chihiro Sasaki. Fluctuations of the order

- parameter in an $SU(N_c)$ effective model. *Phys. Rev. D*, 103(7):074026, 2021. doi: 10.1103/PhysRevD.103.074026.
- [241] P. M. Lo and E. S. Swanson. QED3 at Finite Temperature and Density. *Phys. Rev. D*, 89(2):025015, 2014. doi: 10.1103/PhysRevD.89.025015.
- [242] Sidney S. Avancini, Ricardo L. S. Farias, Marcus Benghi Pinto, William R. Tavares, and Varese S. Timóteo. π_0 pole mass calculation in a strong magnetic field and lattice constraints. *Phys. Lett. B*, 767:247–252, 2017. doi: 10.1016/j.physletb.2017.02.002.
- [243] Adrian Dumitru, Robert D. Pisarski, and Detlef Zschiesche. Dense quarks, and the fermion sign problem, in a $SU(N)$ matrix model. *Phys. Rev. D*, 72:065008, 2005. doi: 10.1103/PhysRevD.72.065008.
- [244] Volker Koch. *Hadronic Fluctuations and Correlations*, pages 626–652. 2010. doi: 10.1007/978-3-642-01539-7_20.
- [245] Anton Andronic, Peter Braun-Munzinger, Krzysztof Redlich, and Johanna Stachel. Decoding the phase structure of QCD via particle production at high energy. *Nature*, 561(7723):321–330, 2018. doi: 10.1038/s41586-018-0491-6.
- [246] R. Venugopalan and M. Prakash. Thermal properties of interacting hadrons. *Nucl. Phys. A*, 546:718–760, 1992. doi: 10.1016/0375-9474(92)90005-5.
- [247] S. Borsanyi, Z. Fodor, S. D. Katz, S. Krieg, C. Ratti, and K. K. Szabo. Freeze-out parameters: lattice meets experiment. *Phys. Rev. Lett.*, 111:062005, 2013. doi: 10.1103/PhysRevLett.111.062005.
- [248] Szabolcs Borsanyi, Zoltan Fodor, Jana N. Guenther, Sandor K. Katz, Kalman K. Szabo, Attila Pasztor, Israel Portillo, and Claudia Ratti. Higher order fluctuations and correlations of conserved charges from lattice QCD. *JHEP*, 10:205, 2018. doi: 10.1007/JHEP10(2018)205.
- [249] Juergen Berges and Krishna Rajagopal. Color superconductivity and chiral symmetry restoration at nonzero baryon density and temperature. *Nucl. Phys. B*, 538: 215–232, 1999. doi: 10.1016/S0550-3213(98)00620-8.
- [250] M. A. Stephanov. Non-Gaussian fluctuations near the QCD critical point. *Phys. Rev. Lett.*, 102:032301, 2009. doi: 10.1103/PhysRevLett.102.032301.
- [251] Boris Berdnikov and Krishna Rajagopal. Slowing out-of-equilibrium near the QCD critical point. *Phys. Rev. D*, 61:105017, 2000. doi: 10.1103/PhysRevD.61.105017.
- [252] D. T. Son and M. A. Stephanov. Dynamic universality class of the QCD critical point. *Phys. Rev. D*, 70:056001, 2004. doi: 10.1103/PhysRevD.70.056001.
- [253] L. Adamczyk et al. Energy Dependence of Moments of Net-proton Multiplicity Dis-

- tributions at RHIC. *Phys. Rev. Lett.*, 112:032302, 2014. doi: 10.1103/PhysRevLett.112.032302.
- [254] Xiaofeng Luo. Energy Dependence of Moments of Net-Proton and Net-Charge Multiplicity Distributions at STAR. *PoS*, CPOD2014:019, 2015. doi: 10.22323/1.217.0019.
- [255] Xiaofeng Luo. Exploring the QCD Phase Structure with Beam Energy Scan in Heavy-ion Collisions. *Nucl. Phys. A*, 956:75–82, 2016. doi: 10.1016/j.nuclphysa.2016.03.025.
- [256] Jochen Thäder. Higher Moments of Net-Particle Multiplicity Distributions. *Nucl. Phys. A*, 956:320–323, 2016. doi: 10.1016/j.nuclphysa.2016.02.047.
- [257] L. Adamczyk et al. Beam energy dependence of moments of the net-charge multiplicity distributions in Au+Au collisions at RHIC. *Phys. Rev. Lett.*, 113:092301, 2014. doi: 10.1103/PhysRevLett.113.092301.
- [258] L. Adamczyk et al. Collision Energy Dependence of Moments of Net-Kaon Multiplicity Distributions at RHIC. *Phys. Lett. B*, 785:551–560, 2018. doi: 10.1016/j.physletb.2018.07.066.
- [259] Adam Bzdak and Volker Koch. Net-baryon multiplicity distribution consistent with lattice QCD. *Phys. Rev. C*, 99(2):024913, 2019. doi: 10.1103/PhysRevC.99.024913.
- [260] Volker Koch and Adam Bzdak. Fluctuations and the QCD Phase Diagram. *Acta Phys. Polon. B*, 47:1867, 2016. doi: 10.5506/APhysPolB.47.1867.
- [261] Marlene Nahrgang, Stefan Leupold, Christoph Herold, and Marcus Bleicher. Nonequilibrium chiral fluid dynamics including dissipation and noise. *Phys. Rev. C*, 84:024912, 2011. doi: 10.1103/PhysRevC.84.024912.
- [262] Christoph Herold, Marlene Nahrgang, Igor Mishustin, and Marcus Bleicher. Chiral fluid dynamics with explicit propagation of the Polyakov loop. *Phys. Rev. C*, 87(1):014907, 2013. doi: 10.1103/PhysRevC.87.014907.
- [263] Swagato Mukherjee, Raju Venugopalan, and Yi Yin. Real time evolution of non-Gaussian cumulants in the QCD critical regime. *Phys. Rev. C*, 92(3):034912, 2015. doi: 10.1103/PhysRevC.92.034912.
- [264] Christoph Herold, Marlene Nahrgang, Yupeng Yan, and Chinorat Kobdaj. Dynamical net-proton fluctuations near a QCD critical point. *Phys. Rev. C*, 93(2):021902, 2016. doi: 10.1103/PhysRevC.93.021902.
- [265] S. Jeon, V. Koch, K. Redlich, and X. N. Wang. Fluctuations of rare particles as a measure of chemical equilibration. *Nucl. Phys. A*, 697:546–562, 2002. doi: 10.1016/S0375-9474(01)01228-3.

-
- [266] Adam Bzdak, Volker Koch, and Vladimir Skokov. Baryon number conservation and the cumulants of the net proton distribution. *Phys. Rev. C*, 87(1):014901, 2013. doi: 10.1103/PhysRevC.87.014901.
- [267] P. Braun-Munzinger, A. Rustamov, and J. Stachel. Bridging the gap between event-by-event fluctuation measurements and theory predictions in relativistic nuclear collisions. *Nucl. Phys. A*, 960:114–130, 2017. doi: 10.1016/j.nuclphysa.2017.01.011.
- [268] Marlene Nahrgang, Tim Schuster, Michael Mitrovski, Reinhard Stock, and Marcus Bleicher. Net-baryon-, net-proton-, and net-charge kurtosis in heavy-ion collisions within a relativistic transport approach. *Eur. Phys. J. C*, 72:2143, 2012. doi: 10.1140/epjc/s10052-012-2143-6.
- [269] Marlene Nahrgang, Marcus Bluhm, Thomas Schaefer, and Steffen A. Bass. Diffusive dynamics of critical fluctuations near the QCD critical point. *Phys. Rev. D*, 99(11):116015, 2019. doi: 10.1103/PhysRevD.99.116015.
- [270] Marlene Nahrgang. The QCD Critical Point and Related Observables. *Nucl. Phys. A*, 956:83–90, 2016. doi: 10.1016/j.nuclphysa.2016.02.074.
- [271] Lijia Jiang, Pengfei Li, and Huichao Song. Correlated fluctuations near the QCD critical point. *Phys. Rev. C*, 94(2):024918, 2016. doi: 10.1103/PhysRevC.94.024918.
- [272] Masakiyo Kitazawa and Masayuki Asakawa. Revealing baryon number fluctuations from proton number fluctuations in relativistic heavy ion collisions. *Phys. Rev. C*, 85:021901, 2012. doi: 10.1103/PhysRevC.85.021901.
- [273] Masakiyo Kitazawa and Masayuki Asakawa. Relation between baryon number fluctuations and experimentally observed proton number fluctuations in relativistic heavy ion collisions. *Phys. Rev. C*, 86:024904, 2012. doi: 10.1103/PhysRevC.86.024904. [Erratum: Phys.Rev.C 86, 069902 (2012)].
- [274] Marlene Nahrgang, Marcus Bluhm, Paolo Alba, Rene Bellwied, and Claudia Ratti. Impact of resonance regeneration and decay on the net-proton fluctuations in a hadron resonance gas. *Eur. Phys. J. C*, 75(12):573, 2015. doi: 10.1140/epjc/s10052-015-3775-0.
- [275] Marcus Bluhm, Marlene Nahrgang, Steffen A. Bass, and Thomas Schaefer. Impact of resonance decays on critical point signals in net-proton fluctuations. *Eur. Phys. J. C*, 77(4):210, 2017. doi: 10.1140/epjc/s10052-017-4771-3.
- [276] Christoph Herold, Marcus Bleicher, Marlene Nahrgang, Jan Steinheimer, Ayut Limphirat, Chinorat Kobdaj, and Yupeng Yan. Broadening of the chiral critical region in a hydrodynamically expanding medium. *Eur. Phys. J. A*, 54(2):19, 2018. doi: 10.1140/epja/i2018-12438-1.
- [277] M. Bluhm, Y. Jiang, M. Nahrgang, J. M. Pawłowski, F. Rennecke, and N. Wink. Time-evolution of fluctuations as signal of the phase transition dynamics in a QCD-

- assisted transport approach. *Nucl. Phys. A*, 982:871–874, 2019. doi: 10.1016/j.nuclphysa.2018.09.058.
- [278] Yoshitaka Hatta and Takashi Ikeda. Universality, the QCD critical / tricritical point and the quark number susceptibility. *Phys. Rev. D*, 67:014028, 2003. doi: 10.1103/PhysRevD.67.014028.
- [279] H. T. Ding et al. Chiral Phase Transition Temperature in (2+1)-Flavor QCD. *Phys. Rev. Lett.*, 123(6):062002, 2019. doi: 10.1103/PhysRevLett.123.062002.
- [280] Frithjof Karsch. Critical behavior and net-charge fluctuations from lattice QCD. *PoS*, CORFU2018:163, 2019. doi: 10.22323/1.347.0163.
- [281] Toshihiro Nonaka. Recent Results and Methods on Higher Order and Off-diagonal Cumulants of Identified Net-particle Multiplicity Distributions in Au+Au Collisions at STAR. *Nucl. Phys. A*, 982:863–866, 2019. doi: 10.1016/j.nuclphysa.2018.10.092.
- [282] C. Sasaki, B. Friman, and K. Redlich. Quark Number Fluctuations in a Chiral Model at Finite Baryon Chemical Potential. *Phys. Rev. D*, 75:054026, 2007. doi: 10.1103/PhysRevD.75.054026.
- [283] C. Sasaki, B. Friman, and K. Redlich. Chiral phase transition in the presence of spinodal decomposition. *Phys. Rev. D*, 77:034024, 2008. doi: 10.1103/PhysRevD.77.034024.
- [284] Y. Hatta and M. A. Stephanov. Proton number fluctuation as a signal of the QCD critical endpoint. *Phys. Rev. Lett.*, 91:102003, 2003. doi: 10.1103/PhysRevLett.91.102003. [Erratum: *Phys.Rev.Lett.* 91, 129901 (2003)].
- [285] Adam Bzdak, Volker Koch, and Nils Strodthoff. Cumulants and correlation functions versus the QCD phase diagram. *Phys. Rev. C*, 95(5):054906, 2017. doi: 10.1103/PhysRevC.95.054906.
- [286] H. Fujii. Scalar density fluctuation at critical end point in NJL model. *Phys. Rev. D*, 67:094018, 2003. doi: 10.1103/PhysRevD.67.094018.
- [287] H. Fujii and M. Ohtani. Sigma and hydrodynamic modes along the critical line. *Phys. Rev. D*, 70:014016, 2004. doi: 10.1103/PhysRevD.70.014016.
- [288] Riccardo Guida and Jean Zinn-Justin. 3-D Ising model: The Scaling equation of state. *Nucl. Phys. B*, 489:626–652, 1997. doi: 10.1016/S0550-3213(96)00704-3.
- [289] Chiho Nonaka and Masayuki Asakawa. Hydrodynamical evolution near the QCD critical end point. *Phys. Rev. C*, 71:044904, 2005. doi: 10.1103/PhysRevC.71.044904.
- [290] Betty Abelev et al. Centrality dependence of π , K, p production in Pb-Pb collisions at $\sqrt{s_{NN}} = 2.76$ TeV. *Phys. Rev. C*, 88:044910, 2013. doi: 10.1103/PhysRevC.88.044910.

-
- [291] Betty Bezverkhny Abelev et al. K_S^0 and Λ production in Pb-Pb collisions at $\sqrt{s_{NN}} = 2.76$ TeV. *Phys. Rev. Lett.*, 111:222301, 2013. doi: 10.1103/PhysRevLett.111.222301.
- [292] Betty Bezverkhny Abelev et al. Multi-strange baryon production at mid-rapidity in Pb-Pb collisions at $\sqrt{s_{NN}} = 2.76$ TeV. *Phys. Lett. B*, 728:216–227, 2014. doi: 10.1016/j.physletb.2014.05.052. [Erratum: *Phys.Lett.B* 734, 409–410 (2014)].
- [293] Betty Bezverkhny Abelev et al. $K^*(892)^0$ and $\phi(1020)$ production in Pb-Pb collisions at $\sqrt{s_{NN}} = 2.76$ TeV. *Phys. Rev. C*, 91:024609, 2015. doi: 10.1103/PhysRevC.91.024609.
- [294] Jaroslav Adam et al. ${}^3_{\Lambda}\text{H}$ and ${}^3_{\Lambda}\bar{\text{H}}$ production in Pb-Pb collisions at $\sqrt{s_{NN}} = 2.76$ TeV. *Phys. Lett. B*, 754:360–372, 2016. doi: 10.1016/j.physletb.2016.01.040.
- [295] Jaroslav Adam et al. Production of light nuclei and anti-nuclei in pp and Pb-Pb collisions at energies available at the CERN Large Hadron Collider. *Phys. Rev. C*, 93(2):024917, 2016. doi: 10.1103/PhysRevC.93.024917.
- [296] Frithjof Karsch, Kenji Morita, and Krzysztof Redlich. Effects of kinematic cuts on net-electric charge fluctuations. *Phys. Rev. C*, 93(3):034907, 2016. doi: 10.1103/PhysRevC.93.034907.
- [297] P. Garg, D. K. Mishra, P. K. Netrakanti, B. Mohanty, A. K. Mohanty, B. K. Singh, and N. Xu. Conserved number fluctuations in a hadron resonance gas model. *Phys. Lett. B*, 726:691–696, 2013. doi: 10.1016/j.physletb.2013.09.019.
- [298] M. Abu-Shady and A. Abu-Nab. The effect of finite temperature and chemical potential on nucleon properties in the logarithmic quark sigma model. *Eur. Phys. J. Plus*, 130(12):248, 2015. doi: 10.1140/epjp/i2015-15248-4.
- [299] T. Hatsuda and T. Kunihiro. Character Changes of Pion and Sigma Meson at Finite Temperature. *Phys. Lett. B*, 185:304, 1987. doi: 10.1016/0370-2693(87)91004-5.
- [300] V. Dexheimer and S. Schramm. Proto-Neutron and Neutron Stars in a Chiral SU(3) Model. *Astrophys. J.*, 683:943–948, 2008. doi: 10.1086/589735.
- [301] C. Downum, T. Barnes, J. R. Stone, and E. S. Swanson. Nucleon-meson coupling constants and form-factors in the quark model. *Phys. Lett. B*, 638:455–460, 2006. doi: 10.1016/j.physletb.2006.05.084.
- [302] Paolo Alba, Wanda Alberico, Rene Bellwied, Marcus Bluhm, Valentina Mantovani Sarti, Marlene Nahrgang, and Claudia Ratti. Freeze-out conditions from net-proton and net-charge fluctuations at RHIC. *Phys. Lett. B*, 738:305–310, 2014. doi: 10.1016/j.physletb.2014.09.052.
- [303] M. Bluhm, P. Alba, W. Alberico, R. Bellwied, V. Mantovani Sarti, M. Nahrgang, and C. Ratti. Parametrization for chemical freeze-out conditions from net-charge

- fluctuations measured at RHIC. *J. Phys. Conf. Ser.*, 612(1):012041, 2015. doi: 10.1088/1742-6596/612/1/012041.
- [304] Gert Aarts, Chris Allton, Simon Hands, Benjamin Jäger, Chrisanthi Praki, and Jon-Ivar Skullerud. Nucleons and parity doubling across the deconfinement transition. *Phys. Rev. D*, 92(1):014503, 2015. doi: 10.1103/PhysRevD.92.014503.
- [305] Gert Aarts, Chris Allton, Davide De Boni, Simon Hands, Benjamin Jäger, Chrisanthi Praki, and Jon-Ivar Skullerud. Light baryons below and above the deconfinement transition: medium effects and parity doubling. *JHEP*, 06:034, 2017. doi: 10.1007/JHEP06(2017)034.
- [306] Chihiro Sasaki. Parity doubling of baryons in a chiral approach with three flavors. *Nucl. Phys. A*, 970:388–397, 2018. doi: 10.1016/j.nuclphysa.2018.01.004.
- [307] Michał Marzecenko and Chihiro Sasaki. Net-baryon number fluctuations in the Hybrid Quark-Meson-Nucleon model at finite density. *Phys. Rev. D*, 97(3):036011, 2018. doi: 10.1103/PhysRevD.97.036011.

.....
(imiona i nazwisko)

..... (aktualny adres do korespondencji) (numer PESEL)

.....
(adres e-mail)

.....
(wydział)

.....
(nazwa studiów doktoranckich)

..... (forma studiów) (numer albumu)

OŚWIADCZENIE O PRAWACH AUTORSKICH I DANYCH OSOBOWYCH

Ja niżej podpisany/a doktorant/ka
Stacjonarnych/Niestacjonarnych Studiów Doktoranckichna
Wydziale oświadczam, że przedkładana
rozprawa doktorska na temat:

.....
.....
.....

- jest mojego autorstwa i nie narusza autorskich praw w rozumieniu ustawy z dnia 4 lutego 1994 r. o prawie autorskim i prawach pokrewnych (tekst jednolity: Dz. U. z 2006 r. Nr 90, poz. 631, z późn. zm.) oraz dóbr osobistych chronionych prawem;
- nie zawiera danych i informacji uzyskanych w sposób niedozwolony;
- nie była wcześniej przedmiotem innej urzędowej procedury związanej z nadaniem dyplomu doktora uczelni wyższej;
- treść rozprawy doktorskiej przedstawionej do obrony, zawarta na przekazanym nośniku elektronicznym, jest identyczna z jej wersją drukowaną.

Oświadczam, iż zostałem/am poinformowany/a o prawie dostępu do treści moich danych osobowych oraz ich poprawiania.
Udostępnienie przez mnie danych osobowych ma charakter dobrowolny.

Wyrażam zgodę, na:

- przetwarzanie moich danych osobowych w myśl ustawy z dnia 29 sierpnia 1997 r. o ochronie danych osobowych (tekst jednolity: Dz. U. z 2014, poz. 1182, z późn. zm.);
- umieszczenie mojej rozprawy doktorskiej w bazie danych Uczelni i jej przechowywanie przez okres stosowny do potrzeb Uczelni;
- wykorzystanie mojej rozprawy doktorskiej jako elementu komparatywnej bazy danych Uczelni;
- udostępnienie mojej rozprawy doktorskiej innym podmiotom celem prowadzenia kontroli antyplagiatowej rozpraw doktorskich i innych tekstów, które zostaną opracowane w przyszłości;
- porównywanie tekstu mojej rozprawy doktorskiej z tekstami innych prac znajdujących się w bazie porównawczej systemu antyplagiatowego i zasobach Internetu.

Wrocław,

(rrrr – mm - dd)

.....

(czytelny podpis autora pracy)